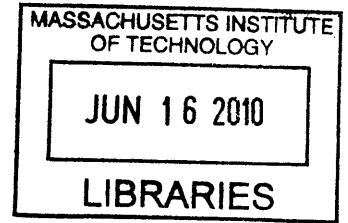


A phase-field study of ternary multiphase  
microstructures

by

Daniel A. Cogswell



S.M. Materials Science and Engineering, MIT, 2006

B.S. Materials Science and Engineering, Northwestern University, 2004

B.S. Computer Science, Northwestern University, 2004

Submitted to the Department of Materials Science and Engineering  
in partial fulfillment of the requirements for the degree of

Doctor of Philosophy in Materials Science and Engineering

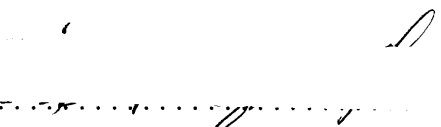

at the

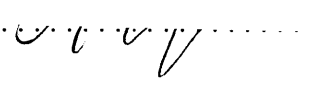
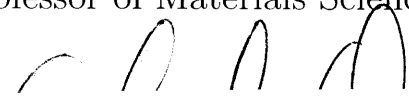
**ARCHIVES**

MASSACHUSETTS INSTITUTE OF TECHNOLOGY

February 2010

© Massachusetts Institute of Technology 2010. All rights reserved.

Author  .....  
Department of Materials Science and Engineering  
 December 16, 2009

Certified by  .....  
W. Craig Carter  
MacVicar Fellow Professor of Materials Science and Engineering  
 Thesis Supervisor

Accepted by ....  
 .....  
Christine Ortiz  
Associate Professor of Materials Science and Engineering  
Chair, Departmental Committee on Graduate Students



# A phase-field study of ternary multiphase microstructures

by

Daniel A. Cogswell

Submitted to the Department of Materials Science and Engineering  
on December 16, 2009, in partial fulfillment of the  
requirements for the degree of  
Doctor of Philosophy in Materials Science and Engineering

## Abstract

A diffuse-interface model for microstructures with an arbitrary number of components and phases was developed from basic thermodynamic and kinetic principles and applied to the study of ternary eutectic phase transformations. Gradients in composition and phase were included in the free energy functional, and a generalized diffusion potential equal to the chemical potential at equilibrium was defined as the driving force for diffusion. Problematic pair-wise treatment of phases at interfaces and triple junctions was avoided, and a cutoff barrier was introduced to constrain phase fractions to physically meaningful values. Parameters in the model were connected to experimentally measurable quantities. Numerical methods for solving the phase-field equations were investigated. Explicit finite difference suffered from stability problems while a semi-implicit spectral method was orders of magnitude more stable but potentially inaccurate. The source of error was found to be the rich temporal dynamics of spinodal decomposition combined with large timesteps and a first-order time integrator. The error was addressed with a second-order semi-implicit Runge-Kutta time integrator and adaptive timestepping, resulting in two orders of magnitude improvement in efficiency. A diffusion-limited growth instability in multiphase thin-film systems was discovered, highlighting how ternary systems differ from binary systems, and intricate asymmetries in the processes of solidification and melting were simulated. A nucleation barrier for solidification was observed and prompted development of a Monte-Carlo-like procedure to trigger nucleation. However when solid was heated from below the melting point, premelting was observed first at phase triple junctions and then at phase boundaries with stable liquid films forming under certain conditions. Premelting was attributed to the shape and position of the metastable liquid curve, which was found to affect microstructure by creating low energy pathways through composition space. Slow diffusivity in solid relative to liquid was shown to produce solutal melting of solid below the melting point. Finally, the multiphase method was used to produce the first reported simulation of the entire transient liquid phase bonding process. The model shows promise for optimizing the bonding process and for simulating non-planar solidification interfaces.

Thesis Supervisor: W. Craig Carter

Title: MacVicar Fellow Professor of Materials Science and Engineering



## Acknowledgments

Graduate school has taught me a lot, particularly about myself. I've come to realize that I have a difficult time declaring something finished without first understanding every little detail. This characteristic drove me to write the thorough, detailed descriptions that appear in this thesis and lead to subtle but important discoveries that have previously been overlooked. On the other hand, being overly concerned with details while working on an open-ended modeling project eventually became mentally exhausting and left me focusing on the negatives of what my model couldn't do rather than its potential. This negative attitude only encouraged more obsession with detail, especially as my work began to appear simple and obvious to me after having thought about it for so long. This resulted in a downward spiral of negativity, common among grad students, that hit bottom at some point during 2009. At one point I imagined this thesis as no more than a collection of several thesis proposals. In retrospect, the absolute bottom seems to have been the beginning of the graduation process.

The only other person whose life was directly impacted by my graduate school struggles was my wonderful wife Courtney. It was unfortunate that our first year of marriage correlated with my last year of graduate school. Courtney, I wish it could have worked out differently, but I do admire the strength you showed throughout the whole process. I am proud to have you by my side, and know we have a lot to look forward to.

Were it not for the prayers and loving support of my family, I would have quit sometime after I got my masters. So Courtney, Mom, Dad, Heather, and Brenna, my success is your success. Likewise for the Elders (Fred, Eileen, Elyce, and Nathan) and many friends from Park Street Church who helped keep me spiritually grounded.

Over the last 5 years I spent countless hours around my office mates. Colin Ashe was a good friend who offered valuable advice and with whom I had many deep discussions on all walks of life. Vyom Sharma and I both started and ended grad school in the same semesters, and shared many common experiences. I will remember

Ming Tang for his amazing intuition and ability to ask challenging questions. Karlene Maskaly, Rick Rajter, Shadow Huang, Celine Hin, Bryan Ho, Billy Woodford, and Victor Brunini, thank you for helping make my time at MIT interesting and exciting.

I am thankful for several other colleagues who offered encouragement or gentle criticism, even though they were not always directly involved in my research. Sound advice or a kind word, I learned, can be very powerful. These people include: Katusyo Thornton, Peter Voorhees, Sam Allen, Jacob White, Jim Warren, and Martin Bazant.

Finally, I am grateful to advisor Craig Carter for funding me for the last 4.5 years, and also to Corning Inc. for being the source of funding for my Ph.D work. Monika Backhaus and Gaozhu Peng both expressed excitement in my work that helped to motivate me during difficult times. I hope that what you find here will be directly applicable to the problems you are trying to solve at Corning.

# Contents

<b>Contents</b>	<b>7</b>
<b>1 Introduction</b>	<b>11</b>
1.1 The basics of phase-field . . . . .	12
1.2 A history of multiphase and multicomponent models . . . . .	14
1.2.1 The Wheeler-Boettinger-McFadden model . . . . .	16
1.2.2 The Steinbach multiphase model and its successors . . . . .	18
1.3 Discussion . . . . .	22
1.4 Thesis outline . . . . .	25
References . . . . .	27
<b>2 A multicomponent multiphase model</b>	<b>33</b>
2.1 Derivation of the multiphase free energy functional . . . . .	34
2.1.1 Free energy of a binary system . . . . .	35
2.1.2 Free energy of a multicomponent system . . . . .	37
2.1.3 Definition of a phase . . . . .	39
2.1.4 Free energy of a multiphase, multicomponent system . . . . .	40
2.1.5 The multiphase, multicomponent diffuse interface . . . . .	42
2.1.6 Physical interpretation of the gradient energy matrices . . . . .	43
2.1.7 A barrier for phase transitions . . . . .	44
2.2 Component evolution . . . . .	45

2.2.1	Equivalence of Gibbs and Helmholtz potentials . . . . .	46
2.2.2	Generalized diffusion potential . . . . .	47
2.2.3	Evolution equations . . . . .	49
2.3	Phase evolution equations . . . . .	51
2.3.1	A problem with the phase equations . . . . .	52
2.3.2	A barrier function for phase fractions . . . . .	53
2.4	Material properties and phase-field parameters . . . . .	57
	References . . . . .	60
<b>3</b>	<b>Numerical methods for phase-field modeling</b>	<b>63</b>
3.1	The phase-field model for numerical analysis . . . . .	65
3.2	Finite Difference . . . . .	66
3.2.1	Comparison of two finite-difference schemes . . . . .	68
3.3	Implicit-Explicit spectral methods . . . . .	70
3.3.1	An IMEX splitting for the Cahn-Hilliard equation . . . . .	72
3.3.2	An IMEX splitting for the nonlinear diffusion equation . . . . .	73
3.4	Measuring error . . . . .	76
3.4.1	Discussion . . . . .	77
3.5	An adaptive timestep spectral method . . . . .	78
3.5.1	2nd-order Runge-Kutta timestepping . . . . .	79
3.5.2	Adaptive timestepping . . . . .	82
3.6	Benchmarks . . . . .	85
3.7	Future Work . . . . .	86
	References . . . . .	88
<b>4</b>	<b>Spherulitic growth in multiphase systems</b>	<b>91</b>
4.1	The free energy landscape . . . . .	92
4.2	Eutectic solidification morphologies . . . . .	95
4.3	Kaleidoscopic spherulites . . . . .	97



4.3.1	Growth mechanism . . . . .	100
4.3.2	Origin of symmetry . . . . .	101
4.3.3	Morphological stability . . . . .	102
4.4	Experimental evidence . . . . .	103
4.4.1	Similarity to snowflakes . . . . .	104
4.4.2	Growth front nucleation in polymers . . . . .	105
4.4.3	Ring structures . . . . .	106
4.4.4	Rhythmic ring growth . . . . .	107
4.5	Evidence in metallic systems . . . . .	108
4.6	Visualizing diffuse interfaces . . . . .	109
	References . . . . .	111
<b>5</b>	<b>Ternary eutectic solidification and melting</b>	<b>117</b>
5.1	Phase-field model for nucleation . . . . .	118
5.1.1	Stochastic Langevin noise . . . . .	119
5.1.2	Incorporating classical nucleation theory . . . . .	121
5.1.3	Nucleation algorithm . . . . .	125
5.2	Simulation of nucleation, growth, and coarsening . . . . .	125
5.2.1	Analysis of nucleation and growth . . . . .	127
5.2.2	Analysis of coarsening . . . . .	129
5.3	Coarsening at an elevated temperature . . . . .	130
5.3.1	Premelting and metastable liquid . . . . .	132
5.3.2	Instability of small particles . . . . .	134
5.4	Asymmetry introduced by unequal diffusivity . . . . .	135
	References . . . . .	139
<b>6</b>	<b>Transient liquids and reactive phases</b>	<b>143</b>
6.1	Simulation of transient liquid bonding . . . . .	144
6.1.1	The four stages of TLPB . . . . .	146

6.2	Discussion of TLPB models . . . . .	149
6.3	Cellular solidification . . . . .	152
6.4	Simulation of reactive bonding . . . . .	153
6.5	Future work . . . . .	157
	References . . . . .	157
<b>7</b>	<b>Conclusion</b>	<b>161</b>
7.1	Future work . . . . .	164
7.1.1	Numerical methods . . . . .	165
7.1.2	Transient liquid bonding . . . . .	166
7.1.3	Thermodynamic and kinetic data . . . . .	166
	References . . . . .	167
<b>A</b>	<b>Multiresolution phase-field modeling</b>	<b>169</b>
A.1	Introduction . . . . .	169
A.2	Background . . . . .	171
A.3	Expected results and their significance . . . . .	174
	References . . . . .	177

# Chapter 1

## Introduction

The primary goal of computational modeling is to gain a deeper understanding of experimental systems and to use this deeper understanding to improve technology. This work grew out of an industrial need for a better understanding of microstructural evolution in ternary ceramic mixtures. The specific motivation was to model the complex ternary reaction pathways that control the formation of cordierite, an exotic ceramic with nearly zero thermal expansion that is used as the substrate material for catalytic converters in automobiles. The formation of cordierite requires very high processing temperatures, and a computer model could be helpful for optimizing the reaction pathway so that cordierite is produced quickly and at lower temperature. Transient liquids, which are regions of solid microstructure that temporarily become liquid, were also observed to form under certain conditions and are thought to have a very important role in microstructural development.

A secondary goal of computational modeling is to develop simple models that generate new insight through accurate prediction of complex experimental observations. Microstructure evolution in multiphase, multicomponent systems is important to understand for industrial processes, and also interesting from an academic perspective [1, 2, 3]. Morphological evolution in ternary and multicomponent systems is much more complex than in binary systems.

Advancements in science are made when we take the work of others and risk heading in new directions instead of remaining in the safety of past successes. The phase-field method, which is described in detail throughout the rest of this work, is perhaps the best available tool for understanding the complexity of microstructure evolution. Although phase-field has been extended to handle multiple components *or* multiple phases, there has been limited progress on models that treat both multiple components and phases simultaneously, with the exception of binary two phase models. The multicomponent, multiphase model developed in this work opens the door for a variety of interesting kinetic studies of phase transitions, morphology, and microstructure evolution.

## 1.1 The basics of phase-field

Phase-field modeling has become an important part of computational materials science because it is a natural way to use thermodynamic data to study the kinetics of microstructure evolution. Phase-field has been used successfully to study first and second-order phase transitions, order-disorder transitions, nucleation and spinodal decomposition, grain growth, coarsening, the growth of dendrites in a super-cooled liquid, directional solidification, faceted crystal growth, diffusion controlled processes, solute drag, interdiffusion, and the effects of anisotropy. The newly developed phase-field crystal method has recently received attention for merging phase-field and molecular dynamics, providing a way to simulate microstructure on diffusive time scales not accessible by molecular dynamics, and atomistic length scales [4, 5, 6]. A substantial amount of literature has been written about the application of phase-field models to these areas, and the reader is referred to several recent review papers for an overview [7, 8, 9, 10, 3, 11].

Phase-field modeling is based on the idea that interfaces in microstructure are diffuse at the nanoscale and can be represented by one or more smoothly varying order

parameters, often taken to be concentration. Phase-field modeling eliminates the need to explicitly track interfaces, which would require defining boundary conditions and deriving evolution equations for each interface. Phase-field implicitly incorporates curvature driven physics and handles creation, destruction, and merging of interfaces, phenomena which are difficult to capture with a sharp interface model. The phase-field equations also capture behavior that occurs in the bulk, away from interfaces. Thus phase-field is ideally suited for modeling the complex morphologies that arise in the study of microstructure.

The order parameter contributes to a free energy functional which is defined for the system, and a variational method is applied to find evolution equations that evolve the system toward the minimum of the energy functional. The free energy functional is found by adding a gradient energy term to the homogeneous free energy density  $f(c)$ , and integrating over the system [12]:

$$F[c, \nabla c] = \int_V (f(c) + \kappa(\nabla c)^2) dV \quad (1.1)$$

$\kappa$  is a constant called the gradient energy coefficient, and the gradient energy term  $\kappa(\nabla c)^2$  penalizes regions with concentration varies sharply. In experimental systems, these regions would have a high driving force for diffusion. The free energy density is generally constructed to promote phase separation, in opposition to the gradient energy term. A stable interface then represents a balance between phase separation and interface formation.

Evolution equations for the order parameters are found by applying a variational approach to the free energy functional. When the time derivative is set equal to the divergence of a flux, evolution is governed by the Cahn-Hilliard equation, which applies to conserved order parameters such as composition:

$$\frac{\partial c}{\partial t} = \nabla \cdot \left( M(c) \nabla \frac{\delta F}{\delta c} \right) \quad (1.2)$$

$M(c)$  is the mobility of the diffusing species, and an important aspect of this thesis will be to determine the compositional dependence of mobility in a multicomponent system.

Setting the time derivative equal proportional to the variational derivative yields the Allen-Cahn equation [13]. This equation does not conserve  $\phi$  and can be used to model phase order parameters:

$$\frac{\partial \phi}{\partial t} = -M(\phi) \frac{\delta F}{\delta \phi} \quad (1.3)$$

The derivation of both equations and their application to multiphase modeling is described in detail in chapter 2.

## 1.2 A history of multiphase and multicomponent models

Multiphase modeling with a phase-field approach begins with a description of an interface between two phases, possibly in the presence of one or more diffusing solutes. In many systems, phase is thought of as binary variable that distinguishes regions separated by sharp interfaces. Phase is generally considered to be a smoothly varying quantity only for liquid-vapor boundaries close to the critical point. In a diffuse interface model however, phase and composition are modeled as smoothly varying quantities at all interfaces. To model such interfaces, a decision must be made whether to treat the interface as an interpolation between two phases with the same composition, or two phases with different compositions. It is not clear that one treatment is necessarily correct, but the two approaches lead to distinctly different models. The first approach was used in the classic WBM model [14, 15, 16] and is extended in this work to model systems with an arbitrary number of components and phases. The second approach was used to add component diffusion to the Steinbach

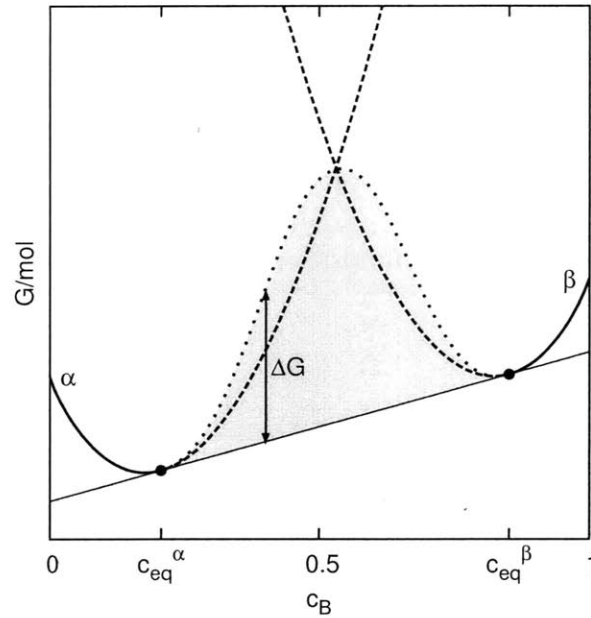


Figure 1-1: The WBM model assumes that the energy of interfacial compositions is a weighting of the dashed regions of the free energy curves, while extensions the Steinbach multiphase model to include solute diffusion assume that the energies of interfacial compositions lie on the common tangent line.

multiphase model [17, 18]. The development of both approaches will now be reviewed as it is important to understand the advantages and disadvantages of each method within the context of the modifications to be made in this thesis.

The fundamental difference between the two approaches is illustrated in figure 1-1, where free energy curves and the common tangent construction for two phases are drawn. A diffuse  $\alpha$ - $\beta$  interface must include compositions between the equilibrium concentrations  $c_{eq}^{\alpha}$  and  $c_{eq}^{\beta}$ , although the energy of these intermediate compositions is somewhat ambiguous. The WBM model assumes that each phase at an interface has the same composition, the composition of the system, and that the free energy of these interfacial points is a weighted average of the dashed portions of the  $\alpha$  and  $\beta$  free energy curves. In a system with no phase gradient energy, the diffuse interface would follow the minimum of the dashed curves, but when a phase gradient energy is included, a possible energy profile across an interface is illustrated by the dotted

line. The difference between the dotted and dashed line is the phase gradient energy contribution to surface energy.  $\Delta G$  in the figure denotes energy at an interfacial point relative to a mixture of  $\alpha$  and  $\beta$  at equilibrium. The gray shaded region is  $\Delta G$  integrated across an interface, and is the interfacial energy contribution due to incorporation of nonequilibrium composition at the interface. The contribution of the shaded area increases for wider interfaces because more nonequilibrium material must be introduced.

The other choice for modeling diffuse interfaces between phases is to assume each phase has its own composition which evolves toward the appropriate equilibrium concentration. At a diffuse interface, interpolation between phases at their equilibrium concentration produces intermediate compositions with energies that lie on the common tangent line. This choice ignores the dashed regions of the free energy curves in figure 1-1 and prevents any metastable phases from appearing, but permits interfaces to be arbitrarily thick for computational convenience.  $\Delta G$  is zero in this case, and widening the interface does not involve the addition of nonequilibrium material at the interface. Thus gradient energy is the only contributor to surface energy.

### 1.2.1 The Wheeler-Boettinger-McFadden model

Wheeler, Boettinger, and McFadden simulated isothermal phase transitions in binary alloys in what became known as the “classic” (WBM) two phase model [14, 15, 16]. A similar model was developed by Caginalp and Xie [19]. The WBM model was later modified to simulate non-isothermal solidification and used to model dendritic growth [20]. The WBM model introduces a non-conserved order parameter  $\phi$  to indicate which regions of the system are solid ( $\phi = 1$ ) and which are liquid ( $\phi = 0$ ). At an interface between liquid and solid,  $\phi$  varies smoothly. Thus the WBM free energy functional depends on both composition and phase gradients:

$$F[f, c, \phi] = \int_V \left( f(\phi, c, T) + \frac{1}{2}\epsilon_c(\nabla c)^2 + \frac{1}{2}\epsilon_\phi(\nabla \phi)^2 \right) dV \quad (1.4)$$



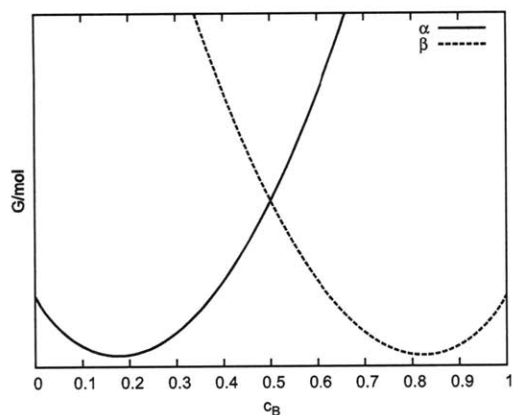
$\epsilon_c$  is a coefficient that specifies the composition gradient energy, and  $\epsilon_\phi$  is a coefficient that specifies the phase gradient energy. The gradient squared terms smooth and regularize the interface between separated phases and introduce interfacial energy.  $f(\phi, c, T)$  is a free energy density that promotes phase separation in the absence of interfacial energies.

Phase and composition gradients are coupled by the free energy functional and overlap at equilibrium to form an interface. The WBM model assumes that each point within a diffuse interface consists of a mixture of phases, each with identical composition. An interpolating function  $p(\phi)$  is used to merge the homogeneous free energy densities of the individual phases,  $f^{liquid}$  and  $f^{solid}$ , into one function:

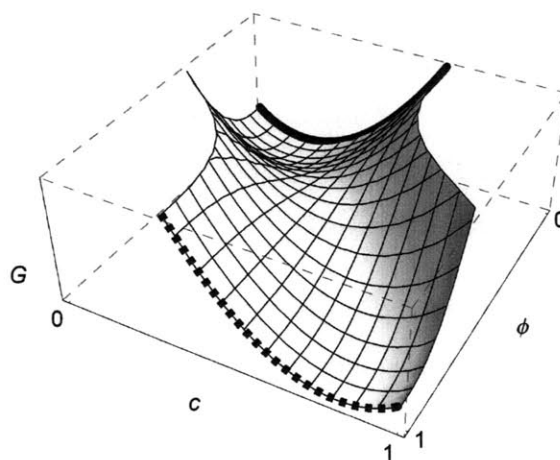
$$f(\phi, c, T) = p(\phi)f^{liquid}(c, T) + (1 - p(\phi))f^{solid}(c, T) \quad (1.5)$$

An interpolation between two free energy curves is illustrated in Fig. 1-2.  $p(\phi)$  has a minima at  $\phi = 0$  and  $\phi = 1$  and provides a barrier for transition from one phase to the other.  $\phi$  can be interpreted as  $\Delta H/\Delta H^{trans}$ , the fraction of molar latent heat that must be absorbed or released for the the system in order to transition from one phase to another. The interpolating function is chosen for numerical convenience, and several functions have been suggested [21]. Because there is no easy extension of the function for handling more than two free energy curves, a multiphase extension of the WBM model for more than three phases has never been developed.

The initial WBM model [14] did not include a  $(\nabla c)^2$  term. Although the model reduced to the sharp interface model in the asymptotic limit, the kinetics of the model disagreed with solute trapping experiments. The necessity of a composition gradient energy for correctly describing diffusion during spinodal decomposition was recognized, and the disagreement was fixed with the inclusion of  $(\nabla c)^2$  terms [15, 16]. However, a large gradient energy coefficient is often necessary for numerical stability but introduces spurious physics as discussed in section 1.3. It was later shown that



(a) Free energy curves for two phases  $\alpha$  and  $\beta$ .



(b) An interpolating function is used to smoothly connect the free energy curves.

Figure 1-2: The WBM model introduces a non-conserved order parameter  $\phi$  and an interpolating function to smoothly connect two free energy curves.

solute trapping could occur without a concentration gradient energy [7, 22], and the composition gradient energy was no longer included in many multiphase models.

### 1.2.2 The Steinbach multiphase model and its successors

Steinbach and Pezolla developed the first phase-field model that was capable of simulating the interaction of an arbitrary number of phases [17]. Their original model did not include solute diffusion and considered pairwise interactions between phases using double well interpolation functions and Allen-Cahn dynamics. The assumption that the dynamics of a multiphase system could be modeled as the sum of pair-wise interactions turned out to be incorrect, producing violations of Young's Law of interfacial stress balance at phase triple junctions. Reports of a foreign third phase appearing at two-phase interfaces are also common among phase-field models that use pair-wise interpolation to model multiphase interactions. Steinbach and Pezolla later improved on their original model with the introduction of interface fields, order parameters that indicate overlap between pairs of phases [18]. The interface fields method correctly

decomposes a multiphase problem into a sum of dual phase changes, allowing time constants and energy scales to be independently specified for each different type of interface.

Tiaden et al. [23] made the first attempt to add solute diffusion to the Steinbach multiphase model. The interfacial region was modeled as a mixture of phases each with a different composition, but with a constant composition ratio. In the Tiaden model, the concentration  $c$  for the whole system is a weighted sum of all  $c_\alpha$ , the concentration of  $c$  in phase  $\alpha$ :

$$c(x, t) = \sum_{\alpha} \phi_{\alpha} c_{\alpha} \quad (1.6)$$

where  $\phi_{\alpha}$  is the phase fraction of  $\alpha$ . Diffusion of a single component was addressed by partitioning the diffusing species amongst the different phases and solving separate diffusion equations in each phase.  $\nabla c_{\alpha}$  was defined as the driving force for component diffusion, and standard Fickian diffusion equations were solved in each phase. Partition coefficients were introduced to allow phases with different solute solubility to be modeled. The coefficients, which can be deduced from an equilibrium phase diagram and determine how solute is penalized, are specific to each phase. The diffusion equations were coupled to phase evolution equations, and the driving force for the phase parameters was a difference in free energy, which was determined from a local linearization of a phase diagram. Such an extrapolation scheme assumes a dilute solution with no demixing behavior, and prohibits the appearance of any metastable phases that lie close to but not on the common tangent.

Although the Tiaden model was important because it demonstrated the feasibility of modeling diffusional transport in a multiphase model, it has several limitations. First, because of its simplistic handling of solute partitioning, it was limited to dilute solute concentrations. Second, the model did not employ a variational approach with its handling of diffusion. The use of diffusion equations with  $\nabla c_i$  as the driving force

is incorrect because in non-ideal phase-separating systems it is the chemical potential of each component which becomes uniform everywhere at equilibrium. Third, because the model was an extension of the Steinbach model [17], the pair-wise handling of phase interactions in a multiphase environment is problematic. And finally, the use of partition coefficients permits phases to have different equilibrium concentrations, but the coefficients cannot easily be related to free energy density. Thus incorporating experimentally measured thermodynamic and kinetic data into the model is difficult.

The dilute solution limitation of the Tiaden model was removed in extension by Kim et al. [24]. Once again only single component diffusion was considered. The model employed the WBM interpolating function to merge free energy curves and relieve the dilute solution assumption, but used the Tiaden assumption that phases interpolated at a diffuse interface each have distinct composition fields. However, Kim introduced a more sophisticated condition of equal chemical potential to determine how to distribute solute amongst the phases at a diffuse interface.

Grafe et al. [25] developed the first multicomponent extension of the Tiaden model. In their model, the total flux of a component in a multiphase region is the sum of the flux of that component in each of the individual phases.  $c_i^\alpha$  is the concentration of component  $i$  in phase  $\alpha$ , and the fluxes are weighted by the phase fractions  $\phi_\alpha$ :

$$c_i(x, t) = \sum_{\alpha} \phi_{\alpha} c_i^{\alpha} \quad (1.7)$$

The driving force for diffusion was again chosen to be  $\nabla c_i^\alpha$ , the concentration gradient of component  $i$  in phase  $\alpha$ , which is a dilute solution approximation. To allow phases to exchange solute, the model assumes that where multiple phase fractions are simultaneously nonzero, such as at a phase boundary or triple junction, the components are able to instantaneously partition themselves amongst the phases as dictated by partition coefficients. The use of partition coefficients amounts to an extrapolation scheme, but the coefficients were assumed to be a function of composition and tem-

perature and were calculated with Thermo-Calc. Grafe chose to use  $\Delta G_{ij}$ , the change in Gibbs energy for the transformation of phase  $i$  to phase  $j$ , as the driving force in the phase-field model rather than an interpolation involving the individual free energy densities. The approximation of  $\Delta G_{ij}$  is only applicable for small undercooling of pure substances and dilute solutions.

Nestler and Wheeler extended the Steinbach multiphase model to study eutectic and peritectic binary alloys [26]. They modeled solute with a nonlinear diffusion equation based on a free energy formulation but did not include a composition gradient energy and assumed an ideal solution. Later on, Nestler, Garcke and Stinner proposed a nonisothermal multicomponent extension governed by an entropy functional [27, 28]. They claim the model applies to arbitrary free energies convex in  $c$  and concave in  $T$ , presumably because no composition energy gradient was included. A complicated phase barrier function was found to be necessary to prevent the appearance of a foreign third phase at a two-phase boundary.

Recently, Eiken et al. [29] developed a multicomponent extension to the Tiaden dilute solution multiphase model which removed the dilute solution limitation and allowed for easier inclusion of thermodynamic data. However, the driving force for solute diffusion was chosen to be the elimination of gradients in a “phase diffusion potential”  $\tilde{\mu}_i^\alpha = \frac{\partial \bar{G}_\alpha}{\partial c_i^\alpha}$  in each phase. Note that the “phase diffusion potential”<sup>1</sup> expresses the slope of the free energy curves and is conceptually different than the chemical potential  $\mu_i^\alpha = \frac{\partial G_\alpha}{\partial n_i^\alpha}$ , which is the thermodynamic quantity uniform everywhere at equilibrium. Apparently having confused slope with chemical potential, Eiken et al. chose the wrong quantity as the driving force for diffusion. The slope of free energy curves with respect to concentration is not required to be constant across a diffuse interface at equilibrium, and their criticism of the WBM model for not having constant “phase diffusional potential” at an interface at equilibrium is therefore incorrect. The appropriate potential for the WBM model, which is defined away from equilibrium

---

<sup>1</sup>Eiken’s choice of the name “phase diffusion potential” is confusing because phases don’t diffuse. The name intends to convey the idea of a diffusion potential within each phase.

and is equivalent to the chemical potential at equilibrium, is discussed in Ch. 2.2.2 for binary and a multicomponent alloys.

Furthermore, exchange of solute between phases in regions of phase-interpolation proved troublesome in the Eiken model [29]. With the assumption that locally coexisting phases can instantaneously exchange solute, a local minimization problem must be solved at each timestep and for every grid point to calculate solute distribution. The state that minimizes energy with respect to solute transfer between phases was called quasi-equilibrium. Approaching this state is very computationally expensive and requires complex thermodynamic calculations, but it eliminates the requirement of dilute solutions while avoiding the use of extrapolation schemes employed by Tieden and Grafe.

Several other models have been proposed that continue to building on the Steinbach line of models. Of particular interest are several that offer improved ways to incorporate experimental thermodynamic data. Grafe et al. reported linking a multicomponent, multiphase model to Thermo-Calc for thermodynamic data and Dictra for diffusion data [25]. Qin and Wallach developed a two-phase multicomponent solidification model [30] and a multiphase, multicomponent model [31] that were linked to the MTDATA thermodynamic database. Steinbach and Eiken recently reported obtaining thermodynamic data for their multiphase multicomponent model with CALPHAD methods and using the NIST mobility database for diffusion data [32].

### 1.3 Discussion

The different length scales that naturally occur in microstructure present a difficult numerical challenge that has influenced the development of phase-field models and still remains an outstanding problem [3, 10]. A detailed discussion of the computational challenges can be found in appendix A. In experimental systems, the width of an

interface might be at most 10nm while the single phase regions it separates (grains if crystallography is included in the model) could be on the order of micrometers in diameter, or larger. Important physics occurs at the length scale of interfaces, but properties of microstructure are determined at the length scale of grains. Since microscopic behavior often involves tens or hundreds of grains, performing realistic simulations that capture both length scales has been impossible. Since a phase-field interface must be resolved with 5-10 grid points for numerical stability, modeling a single grain with a regular grid in 3D might require  $1000^3$  gridpoints. Most of the gridpoints would be in the bulk of the grain where high resolution is not needed. Modeling just this one grain would be very time consuming, and modeling more than a couple of grains is currently impossible.

These computational limitations make it desirable to model interfaces that are unrealistically thick relative to the areas they separate, and thick interfaces introduce spurious physics. When interfaces are too wide, an unphysical jump in chemical potential is observed at moving interfaces [33] and the coalescence of neighboring particles is exaggerated, as are nonequilibrium effects like solute trapping and solute drag. If interfaces are thick and interfacial energy is heavily dependent on composition gradient energy, these interfaces will not obey the Gibbs-Thompson relation. Diffusion gradients in the bulk will contribute to the motion of a thick interface, although they should not according to Gibbs-Thompson. For accurate simulations, the computational interface width should not be larger than the atomistic width.

If the interface width used in a numerical calculation exceeds the atomistic width, either the numerical difficulty must be addressed directly, or else a technique is needed to separate the contribution from composition gradients at the interface and the contribution from gradients in the bulk. Karma and Rappel developed a successful technique to separate the kinetic contribution and the diffusional contribution [34]. They introduced an anti-trapping current to cancel out the chemical potential jump that results from simulating wide interfaces, and used their method to produce quantitatively

accurate simulations of dendrite formation with computationally thick interfaces [35]. Anti-trapping has recently been extended to multicomponent alloys, but is limited to dilute solutions [33]. Although the anti-trapping current fixes a problem that leads to inaccurate dendrite simulations, it is a limited solution because it does not address the underlying computational problem, a disparity in length scales. It merely allows the use of non-physical parameters to achieve physical results.

Much effort in phase-field studies is often invested in insuring that the phase-field equations reduce to a sharp interface model as the gradient energy coefficient approaches zero. Showing that phase-field has built-in curvature driven interfacial motion is certainly a valuable verification for both diffuse and sharp interface models and was an important step that lead toward the acceptance of phase-field as a viable method. However, a diffuse interface model should not be judged solely on its agreement with a sharp interface model. The sharp interface model and Gibbs-Thompson relation are not perfect descriptions of grain boundary motion. They are idealizations based on an infinitely thin Gibbs interface. They assume that all interfaces are identical and make the simplifying assumption that interfacial velocity only depends on curvature. Thus they fail to describe nucleation accurately because interfaces are often diffuse on the length scale of critical nuclei, and interfacial energy cannot technically be defined for a moving interface far from equilibrium.

It is reasonable then to expect that a diffuse interface model that includes composition gradient energy is necessary for studying nucleation and spinodal decomposition. But to our knowledge, no previously developed multicomponent, multiphase model has included a composition gradient energy. It appears that the leading reasons for not including a  $(\nabla c)^2$  in the multiphase models summarized in section 1.2.2 were (1) the demonstration of solute trapping behavior without a gradient energy, and (2) the observation that using an unrealistically large gradient energy coefficient, which is often necessary for numerical stability, produces dendrite tip velocities that do not agree with experiment. Removal of the composition gradient energy contradicts a



significant amount of research that has confirmed the Cahn-Hilliard theory as well as pioneering work by Wheeler, Boettinger, and McFadden that recognized the importance of the term for modeling solute trapping [15].

## 1.4 Thesis outline

Chapter 2 derives a phase-field model that is suited for modeling phase change phenomena in multiphase, multicomponent systems. The model was developed with the goal of studying the growth of small nuclei in multiphase ternary systems, and addresses several concerns with existing models. The multiphase, multicomponent model is derived from basic, accepted thermodynamic arguments without assumptions of dilute solutions and without decomposing the multiphase problem into a sum of pair-wise interactions. The appropriate free energy functional is obtained from a Taylor expansion of homogeneous free energy, and it is shown that a generalized diffusion potential is the appropriate driving force for diffusion. The relationship between model parameters and their experimentally measurable quantities is clarified.

Chapter 3 investigates numerical methods for solving phase-field equations such as those in chapter 2. Explicit finite difference and semi-implicit spectral methods are analyzed. Explicit finite difference is found to be very inefficient and suffer from discretization difficulties, while a semi-implicit spectral method is shown to be orders of magnitude more stable, but potentially inaccurate if large timesteps are used. First order time discretization and the dynamics of phase separation were found to be the two major sources of error. Error was significantly reduced with the use of a second-order implicit-explicit Runge-Kutta time integrator and adaptive timestepping.

Chapter 4 presents the discovery of a diffusion-limited growth instability that is unique to multiphase systems. Simulation of the growth of critical nuclei confined to a thin film in a ternary eutectic system was found to produce kaleidoscopic spherulites: symmetric circular patterns whose morphology is highly dependent on system param-

eters, much like snowflakes. The solidifying interface acts as a high energy nucleation site, and competition between the three solid phases, in combination with a changing radius of curvature, triggers morphological instability. A study of the parameter space reveals three unique growth modes. Because the instability has not yet been experimentally observed, the kaleidoscopic spherulites are rationalized by comparison to solidification structures in simpler systems.

Chapter 5 presents a statistical procedure for simulating nucleation in the multiphase model based on concepts from statistical mechanics that are adapted for computational efficiency. Nucleation and growth in a 2D ternary eutectic system are simulated and shown to agree quantitatively with the Johnson-Mehl-Avrami-Kolmogorov (JMAK) equation. A  $t^{1/2}$  coarsening regime is observed at longer times. The location of the metastable liquid curve is observed to have a profound effect on the developing microstructure. At temperatures slightly below the melting point, liquid appears at phase triple junctions and forms thin films at phase boundaries. The presence of these films increased the coarsening rate by 25%. The ability of metastable free energy curves to affect microstructure before the formation of a stable phase is proposed as an explanation for the experimentally observed phenomenon of premelting.

Chapter 6 applies the multiphase model to simulations of transient liquid phase bonding. The multiphase model is ideally suited for modeling transient liquid bonding and addresses all of the major assumptions of previous modeling efforts. Correct transient liquid bonding behavior emerges from the multiphase model with very little modification. This chapter is the first report of a single simulation that correctly captures all four stages of the bonding process, and composition profiles at each stage are reported for the first time. A simulation of cellular solidification, which is commonly observed during transient liquid bonding, is presented to illustrate how the model could be used to better understand and improve the performance of transient liquid bonds. The model is one of the first to simulate multi-dimensional non-planar

solidification geometries.

Chapter 7 concludes and offers suggestions for future work, including the development of improved numerical methods and further applications for the multiphase model developed in this work.

## References

- [1] W. J. Boettinger, S. R. Coriell, A. L. Greer, A. Karma, W. Kurz, M. Rappaz, and R. Trivedi. Solidification microstructures: Recent developments, future directions. *Acta Materialia*, 48(1):43–70, 2000.
- [2] U. Hecht, L. Granasy, T. Pusztai, B. Bottger, M. Apel, V. Witusiewicz, L. Ratke, J. De Wilde, L. Froyen, D. Camel, B. Drevet, G. Faivre, S. G. Fries, B. Legendre, and S. Rex. Multiphase solidification in multicomponent alloys. *Materials Science & Engineering R-Reports*, 46(1-2):1–49, 2004.
- [3] I. Singer-Loginova and H. M. Singer. The phase field technique for modeling multiphase materials. *Reports on Progress in Physics*, 71(10):32, 2008. Singer-Loginova, I. Singer, H. M. Swiss Federal Institute of Technology ETH, Zurich, Switzerland 374 IOP PUBLISHING LTD 362GS.
- [4] K. R. Elder, M. Katakowski, M. Haataja, and M. Grant. Modeling elasticity in crystal growth. *Physical Review Letters*, 88(24), 2002.
- [5] K. R. Elder and M. Grant. Modeling elastic and plastic deformations in nonequilibrium processing using phase field crystals. *Physical Review E*, 70(5), 2004. Part 1.
- [6] N. Provatas, J. A. Dantzig, B. Athreya, P. Chan, P. Stefanovic, N. Goldenfeld, and K. R. Elder. Using the phase-field crystal method in the multi-scale modeling of microstructure evolution. *Jom*, 59(7):83–90, 2007. Provatas, N. Dantzig, J. A.

- Athreya, B. Chan, P. Stefanovic, P. Goldenfeld, N. Elder, K. R. 78 MINERALS METALS MATERIALS SOC 188CD.
- [7] A. A. Wheeler, N. A. Ahmad, W. J. Boettinger, R. J. Braun, G. B. McFadden, and B. T. Murray. Recent developments in phase-field models of solidification. In H. J. Rath, editor, *G1 Symposium of COSPAR Scientific Commission G on Microgravity Sciences - Results and Analysis of Recent Spaceflights, at the 30th COSPAR Scientific Assembly*, volume 16, pages 163–172, Hamburg, Germany, 1994. Pergamon Press Ltd. 48 OXFORD 7 BD12P.
- [8] WJ Boettinger, JA Warren, C Beckermann, and A Karma. Phase-field simulation of solidification. *ANNUAL REVIEW OF MATERIALS RESEARCH*, 32:163–194, 2002.
- [9] L. Q. Chen. Phase-field models for microstructure evolution. *Annual Review of Materials Research*, 32:113–140, 2002.
- [10] N. Moelans, B. Blanpain, and P. Wollants. An introduction to phase-field modeling of microstructure evolution. *Calphad-Computer Coupling of Phase Diagrams and Thermochemistry*, 32(2):268–294, 2008. Moelans, Nele Blanpain, Bart Wollants, Patrick.
- [11] Ingo Steinbach. Phase-field models in materials science. *Modelling and Simulation in Materials Science and Engineering*, 17(7):073001 (31pp), 2009.
- [12] John W. Cahn and John E. Hilliard. Free energy of a nonuniform system. i. interfacial free energy. *Journal of Chemical Physics*, 28(2):258–267, 1958.
- [13] SM Allen and JW Cahn. Microscopic theory for antiphase boundary motion and its application to antiphase domain coarsening. *ACTA METALLURGICA*, 27(6):1085–1095, 1979.

- [14] AA Wheeler, WJ Boettinger, and GB McFadden. Phase-field model for isothermal phase-transitions in binary-alloys. *PHYSICAL REVIEW A*, 45(10):7424–7439, MAY 15 1992.
- [15] A. A. Wheeler, W. J. Boettinger, and G. B. McFadden. Phase-field model of solute trapping during solidification. *Physical Review E*, 47(3):1893–1909, 1993.
- [16] A. A. Wheeler, G. B. McFadden, and W. J. Boettinger. Phase-field model for solidification of a eutectic alloy. *Proceedings of the Royal Society of London Series a-Mathematical Physical and Engineering Sciences*, 452(1946):495–525, 1996. 39 ROYAL SOC LONDON UM232.
- [17] I Steinbach, F Pezzolla, B Nestler, M Seesselberg, R Prieler, GJ Schmitz, and JLL Rezende. A phase field concept for multiphase systems. *PHYSICA D*, 94(3):135–147, JUL 1 1996.
- [18] I Steinbach and F Pezzolla. A generalized field method for multiphase transformations using interface fields. *PHYSICA D*, 134(4):385–393, DEC 10 1999.
- [19] G. Caginalp and W. Xie. Phase-field and sharp-interface alloy models. *Physical Review E*, 48(3):1897–1909, 1993.
- [20] J. A. Warren and W. J. Boettinger. Prediction of dendritic growth and microsegregation patterns in a binary alloy using the phase-field method. *Acta Metallurgica Et Materialia*, 43(2):689–703, 1995.
- [21] S. L. Wang, R. F. Sekerka, A. A. Wheeler, B. T. Murray, S. R. Coriell, R. J. Braun, and G. B. McFadden. Thermodynamically-consistent phase-field models for solidification. *Physica D*, 69(1-2):189–200, 1993. 32 ELSEVIER SCIENCE BV MH387.

- [22] S. G. Kim, W. T. Kim, and T. Suzuki. Interfacial compositions of solid and liquid in a phase-field model with finite interface thickness for isothermal solidification in binary alloys. *Physical Review E*, 58(3):3316–3323, 1998. Part B.
- [23] J Tiaden, B Nestler, HJ Diepers, and I Steinbach. The multiphase-field model with an integrated concept for modelling solute diffusion. *PHYSICA D*, 115(1-2):73–86, APR 15 1998.
- [24] S. G. Kim, W. T. Kim, and T. Suzuki. Phase-field model for binary alloys. *Physical Review E*, 60(6):7186–7197, 1999. Part B.
- [25] U. Grafe, B. Bottger, J. Tiaden, and S. G. Fries. Coupling of multicomponent thermodynamic databases to a phase field model: Application to solidification and solid state transformations of superalloys. *Scripta Materialia*, 42(12):1179–1186, 2000.
- [26] B. Nestler and A. A. Wheeler. A multi-phase-field model of eutectic and peritectic alloys: numerical simulation of growth structures. *Physica D-Nonlinear Phenomena*, 138(1-2):114–133, 2000.
- [27] H. Garcke, B. Nestler, and B. Stinner. A diffuse interface model for alloys with multiple components and phases. *Siam Journal on Applied Mathematics*, 64(3):775–799, 2004. 45 SIAM PUBLICATIONS 815EW.
- [28] B. Nestler, H. Garcke, and B. Stinner. Multicomponent alloy solidification: Phase-field modeling and simulations. *Physical Review E*, 71(4), 2005. Part 1.
- [29] J. Eiken, B. Boettger, and I. Steinbach. Multiphase-field approach for multicomponent alloys with extrapolation scheme for numerical application. *PHYSICAL REVIEW E*, 73(6, Part 2), JUN 2006.

- [30] R. S. Qin and E. R. Wallach. A phase-field model coupled with a thermodynamic database. *Acta Materialia*, 51(20):6199–6210, 2003.
- [31] R. S. Qin, E. R. Wallach, and R. C. Thomson. A phase-field model for the solidification of multicomponent and multiphase alloys. *Journal of Crystal Growth*, 279(1-2):163–169, 2005. 25 ELSEVIER SCIENCE BV 929LU.
- [32] I. Steinbach, B. Boettger, J. Eiken, N. Warnken, and S. G. Fries. Calphad and phase-field modeling: A successful liaison. *JOURNAL OF PHASE EQUILIBRIA AND DIFFUSION*, 28(1):101–106, FEB 2007.
- [33] S. G. Kim. A phase-field model with antitrapping current for multicomponent alloys with arbitrary thermodynamic properties. *Acta Materialia*, 55(13):4391–4399, 2007. Kim, Seong Gyoou 50 PERGAMON-ELSEVIER SCIENCE LTD 195UC.
- [34] A. Karma and W. J. Rappel. Phase-field method for computationally efficient modeling of solidification with arbitrary interface kinetics. *Physical Review E*, 53(4):R3017–R3020, 1996. Part A.
- [35] A. Karma and W. J. Rappel. Quantitative phase-field modeling of dendritic growth in two and three dimensions. *Physical Review E*, 57(4):4323–4349, 1998.

THIS PAGE INTENTIONALLY LEFT BLANK



## Chapter 2

# A model for microstructure with multiple components and phases

The discussion in chapter 1 highlighted shortcomings of existing multiphase, multi-component phase-field models and argued that they are not adequate for modeling metastable phases, nucleation, and spinodal decomposition because of unjustifiable physical assumptions. Several models are also very computationally expensive. This chapter will present the derivation a new model that combines aspects of the WBM model, the Steinbach models, and nonlinear diffusion theory. The model is applicable to systems with an arbitrary number of components and phases, each with their own unique thermodynamic and kinetic properties. Isothermal conditions are assumed.

It is necessary to start from basic principles in order to correct subtle misconceptions that come from hasty application of the textbook concepts. Therefore the derivation of the free energy functional and all evolution equations will be presented in detail. The multiphase, multicomponent model is derived from basic, accepted thermodynamic arguments without assumptions of dilute solutions and without decomposing the multiphase problem into a sum of pair-wise interactions. Following the approach of Cahn and Hilliard [1], a free energy functional is derived from a Taylor expansion of homogeneous free energy. Three gradient energy parameters arise

from the Taylor expansion. One is the classic composition gradient energy coefficient, another controls the atomic width of an interface, and the third adds an additional energy penalty for composition gradients at an interface. The combination of three unique parameters allow the interfacial width and interfacial energy to be decoupled.

A common misconception addressed in this chapter is that the chemical potential of component  $i$  in a multicomponent system with composition gradient energies is  $\mu_i = \frac{\delta F}{\delta c_i}$  [2, 3, 4, 5]. This definition leads to a Cahn-Hilliard equation for each component in a multicomponent system:

$$\frac{\partial c_i}{\partial t} = \nabla \cdot \left( M \nabla \frac{\delta F}{\delta c_i} \right) \quad (2.1)$$

Although this formulation produces a monotonically decreasing energy and is correct for binary systems, it violates a basic result of thermodynamics. The Gibbs-Duhem relation states that when components are constrained, their chemical potentials are also constrained. A generalized diffusion potential will be introduced to resolve the misconception, and an important distinction will be made between the chemical potential and the diffusion potential, which is defined away from equilibrium but approaches the chemical potential at equilibrium. The generalized diffusion potential will then be used in the derivation of component evolution equations, and phase evolution equations are derived with a special cutoff boundary condition to prevent the appearance of negative phase fractions. Finally, the relationship between model parameters and their experimentally measurable quantities is clarified.

## 2.1 Derivation of the multiphase free energy functional

An important part of a phase field model is the free energy functional. Once the free energy functional is defined and gradient coefficients specified, the evolution equations

can be derived. This section begins with the derivation of the free energy functional for a single phase binary system, then progresses to multicomponent systems, and finally progresses to multicomponent, multiphase systems. Differences between the free energy functions are highlighted.

### 2.1.1 Free energy of a binary system

In an influential paper that laid the foundation for phase field modeling, Cahn and Hilliard derived an expression for the free energy of an inhomogeneous binary system [1]. Their approach was to assume that the free energy of an infinitesimal volume in a nonuniform system depends both on its composition and the composition of its nearby environment. Total free energy cannot depend solely on local composition because different spatial configurations with the same volume fraction are not energetically equivalent; a heterogeneous system has more interfacial area and will have a higher energy. Therefore Cahn and Hilliard assumed that free energy depends both on composition and its derivatives for an inhomogeneous system.

Cahn and Hilliard started with the homogeneous free energy density for a binary system  $f(c)$ , and performed a Taylor expansion on  $f(c)$  in terms of the derivatives of composition to approximate  $f(c, \nabla c, \nabla^2 c, \dots)$ . Because the mole fractions of a binary system must obey the relationship  $c_1 + c_2 = 1$ , only one mole fraction and one chemical potential are independent. The expansion of  $f(c, \nabla c, \nabla^2 c, \dots)$  about the

point  $f_0 = f(c, 0, 0, \dots)$  yields:

$$\begin{aligned}
 f(c, \nabla c, \nabla^2 c, \dots) &= f_0 + \left( \frac{\partial f}{\partial \nabla c} \right)_0 (\nabla c - 0) + \left( \frac{\partial f}{\partial \nabla^2 c} \right)_0 (\nabla^2 c - 0) + \dots \\
 &\quad + \frac{1}{2} \left( \frac{\partial^2 f}{\partial (\nabla c)^2} \right)_0 (\nabla c - 0)^2 + \frac{1}{2} \left( \frac{\partial^2 f}{\partial (\nabla^2 c)^2} \right)_0 (\nabla^2 c - 0)^2 + \dots \\
 &\quad + \left( \frac{\partial^2 f}{\partial \nabla c \partial \nabla^2 c} \right)_0 (\nabla c - 0)(\nabla^2 c - 0) + \dots \\
 &\quad + \dots
 \end{aligned} \tag{2.2}$$

The definition of Taylor's theorem for a function of  $n$  variables has been included in an endnote<sup>1</sup>. Performing the Taylor expansion assumes that concentration is continuous over the entire system and differentiable to whatever order is required. The subscript 0 is used to represent evaluation of a quantity under homogeneous conditions where  $c$  is constant and all derivatives  $\nabla c, \nabla^2 c, \dots$  are zero. The terms with this subscript express how  $f$  varies spatially and are related to crystal symmetry. For example, the term  $(\partial f / \partial \nabla c)_0$  is a vector and  $(\partial^2 f / \partial (\nabla c)^2)_0$  is a second-rank tensor. Morris [6] provides justification for excluding  $|\nabla c|$  terms from the expansion, and for including terms in  $\nabla c$  only for systems with symmetries derived from the point group  $C_{\infty v}$ . For higher symmetries (or any system with inversion symmetry),  $(\partial f / \partial \nabla c)_0$  is zero. Furthermore for isotropic or cubic symmetry,  $(\partial^2 f / \partial (\nabla c)^2)_0$  reduces to a scalar. Thus for an isotropic or cubic material, Eq. 2.2 simplifies to an equation with constant coefficients and even powers of  $\nabla c$ :

$$f(c, \nabla c, \nabla^2 c, \dots) = f_0 + \kappa_1 \nabla^2 c + \frac{1}{2} \kappa_2 (\nabla c)^2 + \frac{1}{2} \kappa_3 (\nabla^2 c)^2 + \kappa_4 \nabla^4 c + \dots \tag{2.3}$$

Cahn and Hilliard argued that the derivative terms with even powers  $\nabla^2 c, \nabla^4 c, \nabla^6 c$ , etc. should vanish. They used the divergence theorem to break  $\nabla^2 c$  into the sum of a term in  $(\nabla c)^2$  and a flux through an external surface, which can be chosen so that it is zero. Thus even power derivatives can be discarded. Because of the

assumption that the free energy density is influenced only by concentration within a small neighborhood of a volume, it is reasonable to truncate the expansion after very few terms when  $c$  is well-behaved. Keeping only terms up to second-order produces the Cahn-Hilliard free energy functional:

$$F[f, c] = \int_V (f(c) + \kappa(\nabla c)^2) dV \quad (2.4)$$

where  $\kappa$  is a gradient energy coefficient that penalizes the formation of sharp interfaces.

### 2.1.2 Free energy of a multicomponent system

The approach of Cahn and Hilliard is now applied to a system with an arbitrary number of components. A system with  $M$  components has  $M - 1$  independent mole fractions<sup>1</sup> that obey the following constraint:

$$\sum_{i=1}^M c_i = 1 \quad (2.5)$$

The inhomogeneous free energy becomes a function of each independent component in the system as well as their derivatives:

$$f(c_1, c_2, \dots, \nabla c_1, \nabla c_2, \dots, \nabla^2 c_1, \nabla^2 c_2, \dots) \quad (2.6)$$

---

<sup>1</sup>Note that if density is assumed to be constant everywhere in the system, mole fractions and concentrations are equivalent quantities.

The Taylor expansion of the multicomponent  $f$  about a homogeneous point  $f_0 = f(c_1, c_2, \dots, 0, 0, \dots, 0, 0, \dots)$  is:

$$\begin{aligned}
f(c_1, c_2, \dots, \nabla c_1, \nabla c_2, \dots, \nabla^2 c_1, \nabla^2 c_2, \dots) &= f_0 \\
&+ \left( \frac{\partial f}{\partial \nabla c_1} \right)_0 \nabla c_1 + \left( \frac{\partial f}{\partial \nabla c_2} \right)_0 \nabla c_2 + \dots \\
&+ \left( \frac{\partial f}{\partial \nabla^2 c_1} \right)_0 \nabla^2 c_1 + \left( \frac{\partial f}{\partial \nabla^2 c_2} \right)_0 \nabla^2 c_2 + \dots \\
&+ \frac{1}{2} \left( \frac{\partial^2 f}{\partial (\nabla c_1)^2} \right)_0 (\nabla c_1)^2 + \frac{1}{2} \left( \frac{\partial^2 f}{\partial (\nabla c_2)^2} \right)_0 (\nabla c_2)^2 + \dots \\
&+ \left( \frac{\partial^2 f}{\partial \nabla c_1 \partial \nabla c_2} \right)_0 \nabla c_1 \cdot \nabla c_2 + \dots \\
&+ \dots
\end{aligned} \tag{2.7}$$

For simplicity only terms for two components up to second-order have been written out because higher order terms will be excluded from the expansion. Higher order terms and terms for additional components follow the suggested pattern. The biggest difference between the binary expansion (Eq. 2.2) and the multicomponent expansion (Eq. 2.7) is that the multicomponent expansion has terms that couple pairs of composition gradients. These terms appear on line 5 of Eq. 2.7.

The assumptions previously discussed in section 2.1.1 are kept. Only isotropic and cubic symmetry of  $f$  is considered, allowing the tensors to be replaced with constants, and terms in  $\nabla c$ , as well as even derivatives, are excluded. The Taylor expansion of  $f$  in terms of the  $M - 1$  independent components and their derivatives is:

$$f(c_1, c_2, \dots, \nabla c_1, \nabla c_2, \dots) = f_0 + \sum_{i=1}^{M-1} \frac{1}{2} \kappa_i (\nabla c_i)^2 + \sum_{j < i} \sum_{i=1}^{M-1} \kappa_{ij} \nabla c_i \cdot \nabla c_j \tag{2.8}$$

This equation has been previously reported in literature [7]. Multicomponent systems with gradient energies were first studied in the thesis work of DeFontaine [8], and his approach is summarized by Eyre [2] and by Elliott and Garcke [3]. Multicomponent gradient energies have since been used by Morral and Cahn [9], Hoyt [10], and Eyre

[11] in spinodal decomposition studies in ternary systems.

A simpler form for Eq. 2.8 can be found by combining the summation terms:

$$f(c_1, c_2, \dots, \nabla c_1, \nabla c_2, \dots) = f(c_1, c_2, \dots) + \sum_{i,j=1}^{M-1} \frac{1}{2} \kappa_{ij} \nabla c_i \cdot \nabla c_j \quad (2.9)$$

$\kappa_{ij}$  is a symmetric matrix of gradient energy coefficients that will be discussed in detail in section 2.1.6. A free energy functional that expresses the energy of the entire system is found by integrating the inhomogenous free energy:

$$F[f, \{c\}] = \int_V \left( f(\{c\}) + \sum_{i,j=1}^{M-1} \frac{1}{2} \kappa_{ij} \nabla c_i \cdot \nabla c_j \right) dV \quad (2.10)$$

where  $\{c\}$  denotes a sets of  $M - 1$  independent mole fraction fields.

### 2.1.3 Definition of a phase

A phase is a region of a microstructure with homogeneous properties that is physically distinct from other regions of the system, excluding geometric transformations that map one region onto another. In the study of microstructure, phases most commonly differ in composition and/or crystal structure, although many other physical differences can distinguish phases. Although the volume fraction of phases in equilibrium is predicted from thermodynamics, phase itself is not a thermodynamic state variable; phase provides a thermodynamic state function. Phase may be thought of as a labeling device for identifying regions with different state functions, and in this work the definition of a phase is taken to be a region of microstructure characterized by a homogeneous free energy density  $f_\alpha$  that differs from the free energy densities of the other phases.

Phase fraction variables are introduced for the purpose of associating regions of the system with different free energy curves. Each phase is assigned a phase fraction  $\phi$  that varies between 0 and 1. For a multiphase system,  $\phi_\alpha$  is a spatially varying

order parameter that indicates where the  $\alpha$ -phase exists in a microstructure. Regions of  $\phi_\alpha = 0$  designate areas where no  $\alpha$ -phase is present, and areas of  $\phi_\alpha = 1$  correspond to single-phase regions of  $\alpha$ . For a system with  $N$  phases, the phase fractions obey a phase fraction constraint:

$$\sum_{\alpha=1}^N \phi_\alpha = 1 \quad (2.11)$$

In single phase regions the homogeneous free energy is simply  $f_\alpha$ , the homogeneous free energy of the  $\alpha$ -phase. Microstructure (excluding grain boundaries, defects, etc.) is composed of single phase regions separated by interfaces, and only at the interfaces are more than one  $\phi$  non-zero. The free energy density at interfaces is a function of multiple phase fractions, free energy functions, and components. Because the thermodynamic potential of a multiphase system is equal to the summation of potentials over all all phases,[12] a linear weighting of the free energy densities by phase fractions is used for the homogeneous free energy of a multiphase system:

$$f(\{c\}, \{\phi_1, \phi_2, \dots, \phi_N\}) = \sum_{\alpha=1}^N \phi_\alpha f_\alpha(\{c\}) \quad (2.12)$$

This form reduces to  $f_\alpha(\{c\})$  when only the  $\alpha$ -phase is present, yet can be constructed for an arbitrary number of phases. Additionally, the free energy where three or more phases are simultaneously nonzero in the diffuse interface model is treated directly. Treating a phase triple junction as a sum of pair-wise interactions caused problems in other multiphase models as discussed in chapter 1.

### 2.1.4 Free energy of a multiphase, multicomponent system

The free energy functional approach reviewed for binary systems in section 2.1.1 and extended to multicomponent systems in section 2.1.2 is applied here to derive a free energy functional for multiphase, multicomponent systems. For an  $N$ -phase,  $M$ -component system,  $f(\{c\}, \{\phi\}, \{\nabla c\}, \{\nabla \phi\}, \dots)$  is a function of a set of  $M - 1$



independent mole fractions and  $N - 1$  independent phase fractions. Once again only isotropic and cubic symmetry of the free energy is considered, terms in  $\nabla c$  and even derivatives of  $c$  are excluded from the Taylor expansion, and only terms up to second-order are kept. The full expansion about the homogeneous free energy  $f(\{c\}, \{\phi\}, \{0\}, \{0\}, \dots)$  is not algebraically difficult but has many terms and is not explicitly written out here. It is analogous to Eq. 2.10 but with terms for  $\phi$  in addition to  $c$ . There is one new set of second-order terms in the expansion that couple composition gradients and phase gradients:

$$\left( \frac{\partial^2 f}{\partial \nabla c \partial \nabla \phi} \right)_0 \nabla c \cdot \nabla \phi \quad (2.13)$$

It is assumed for simplicity that there is no coupling between  $\nabla c$  and  $\nabla \phi$  and that these terms are all zero. These terms could be pertinent certain circumstances as they provide a third parameter for adjusting interfacial energy. They penalize a concentration gradient within an interfacial region independently of  $\kappa_{ij}$ . The Taylor expansion of the homogeneous free energy is simplified in the manner used to reach Eq. 2.10 and integrated to produce the multiphase, multicomponent free energy functional:

$$F[\{f\}, \{c\}, \{\phi\}] = \int_V \left( \sum_{\alpha=1}^N \phi_{\alpha} f_{\alpha}(\{c\}) + \sum_{\alpha, \beta=1}^{N-1} \frac{1}{2} \lambda_{\alpha\beta} \nabla \phi_{\alpha} \cdot \nabla \phi_{\beta} + \sum_{i, j=1}^{M-1} \frac{1}{2} \kappa_{ij} \nabla c_i \cdot \nabla c_j \right) dV \quad (2.14)$$

where  $\lambda_{\alpha\beta}$  is a matrix of phase gradient energy coefficients that couples phase gradients. Eq. 2.14, which is the central equation of focus in this work, is a first order approximation of the free energy of a system with an inhomogeneous distribution of phases and components. It reduces to the Cahn-Hilliard equation for a single phase, two-component system.

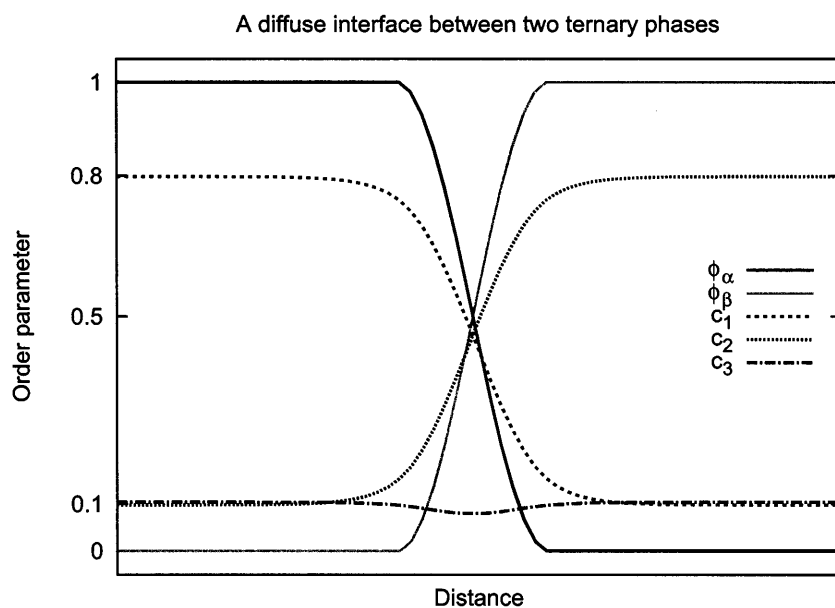


Figure 2-1: A diffuse interface computation of the of the boundary between two phases  $\alpha$  and  $\beta$  in a ternary system. The order parameters vary smoothly at the interface and are at their equilibrium values far from the interface. The equilibrium composition of  $\alpha$  is  $c_1 = .8$  and  $c_2 = .1$ , and the equilibrium composition of  $\beta$  is  $c_1 = .1$  and  $c_2 = .8$ .

### 2.1.5 The multiphase, multicomponent diffuse interface

The interface between two phases is assumed to consist of a thin layer across which the physical properties vary continuously from those of the interior of one phase to those of the interior of the other. Fig. 2-1 illustrates how composition and phase vary at a diffuse interface in a ternary system described by Eq. 2.14. A diffuse interface at equilibrium represents a balance between free energy curves, composition gradients, and phase gradients. The free energy curves are the driving force for phase separation, and the gradient energy coefficients  $\lambda_{\alpha\beta}$  and  $\kappa_{ij}$  penalize gradients that develop, creating a surface energy at phase boundaries.  $\kappa_{ij}$  penalizes phases for differing in composition. Holding  $\kappa_{ij}$  constant, phases that differ more in composition will naturally have larger gradients that will be more harshly penalized.  $\lambda_{\alpha\beta}$  introduces additional energy not captured by the composition gradients at phase boundaries.

This energy derives from some physical difference between the phases other than composition.

### 2.1.6 Physical interpretation of the gradient energy matrices

For an  $N$ -phase,  $M$ -component system, the phase gradient energy matrix  $\lambda$  has dimension  $N - 1$  and the component gradient energy matrix  $\kappa$  has dimension  $M - 1$ . The gradient energy coefficients coupling the implicitly defined  $N^{\text{th}}$  phase (and  $M^{\text{th}}$  component) are not explicitly defined in  $\lambda$  and  $\kappa$ , but are instead distributed across all of the coefficients.  $\lambda$  and  $\kappa$ , which appear in the free energy functional, are in fact dense versions of larger matrices that have a direct physical interpretation. These matrices are  $\Lambda$ , which couples the  $N$  phase gradients, and  $K$  which couples the  $M$  composition gradients. For example, the coupling of  $N$  phase gradients can be written in matrix form as:

$$\frac{1}{2} \begin{bmatrix} \nabla\phi_1 & \nabla\phi_2 & \cdots & \nabla\phi_N \end{bmatrix} \begin{bmatrix} \Lambda_{11} & \Lambda_{12} & \cdots & \Lambda_{1N} \\ \Lambda_{21} & \Lambda_{22} & \cdots & \Lambda_{2N} \\ \vdots & \vdots & \ddots & \vdots \\ \Lambda_{N1} & \Lambda_{N2} & \cdots & \Lambda_{NN} \end{bmatrix} \begin{bmatrix} \nabla\phi_1 \\ \nabla\phi_2 \\ \vdots \\ \nabla\phi_N \end{bmatrix} \quad (2.15)$$

A similar expression relating composition gradients can also be written. Eq. 2.15 illustrates the physical basis of  $\Lambda$ . The coefficients of  $\Lambda$  determine the energy of different configurations of interfaces by imposing an energy penalty for every possible pair of overlapping gradients. An analogous  $M \times M$  matrix  $K$  contains the composition gradient energy coefficients  $K_{ij}$  and introduces an energy penalty for overlapping composition gradients. Recall that no coupling between phase and concentration gradients was assumed, so the combination of  $\Lambda$  and  $K$  independently control the interfacial energy of every combination of phases.

If the phase conservation constraint  $\nabla\phi_N = -(\nabla\phi_1 + \nabla\phi_2 + \dots + \nabla\phi_{N-1})$  (Eq. 2.11) is substituted into Eq. 2.15 and the matrix multiplication is performed, an

expression representing the gradient energy in terms of the  $N - 1$  phase gradients is obtained. The coefficients of the terms in this equation are related to the  $\lambda_{\alpha\beta}$  that form the matrix  $\lambda$  with  $N - 1$  rows and columns. The diagonal terms  $\lambda_{\alpha\alpha}$  are the coefficients of the squared terms, and the off diagonal terms  $\lambda_{\alpha\beta}$  are equal to the coefficients of the cross terms multiplied by  $\frac{1}{2}$ .

Because of the dependence of the  $N^{th}$  phase on all other phases, elimination of the  $N^{th}$  row and column of  $\Lambda$  has distributed the gradient energy coefficients for the  $N^{th}$  phase across all coefficients of  $\lambda$ . In general  $\lambda$  will be a fully dense matrix because the coefficient  $\Lambda_{NN}$  must always be positive.

The physical basis for  $\Lambda$  and  $K$  requires that they be symmetric positive definite matrices. The symmetry of the matrices can be justified because free energy must be invariant to reflection. Switching the direction of all gradients at an interface should not change the free energy. The simplification of the summation terms from Eq. 2.8 to Eq. 2.9 (and the analogous simplification to reach Eq. 2.14) illustrates how symmetry has also been built in to the gradient energy matrices  $\lambda$  and  $k$ .  $\Lambda$  and  $K$  must also be positive-definite because, if the matrices had negative eigenvalues, there would be a coupling of gradients (i.e. in the direction of the eigenvector corresponding to the negative eigenvalue) for which making an increasingly sharp interface would lower the free energy of the system, producing a physically impossible negative surface energy. The set of evolution equations would then become ill-posed, as solving diffusion equations with a negative diffusivity is unconditionally unstable.

### 2.1.7 A barrier for phase transitions

A potential problem with Eq. 2.14 as stated is that the linear weighting of free energy curves (Eq. 2.12) relies on the shape of the free energy curves to create a phase transition barrier with respect to changes in composition. If composition does not change in a phase transition, the model does not provide a barrier and transition occurs without an interface (i.e. the interface has infinite width). Thus

without modification the model does not correctly handle phase transitions for pure components.

Although a phase barrier may not be necessary for phases that differ significantly in composition, a barrier can be easily incorporated into the model when needed. A result of the cutoff constraint developed in section 2.3.2 is that *any* function can be used as a barrier, regardless of its slope at  $\phi = 0$  and  $\phi = 1$ . A simple barrier between  $\alpha$  and  $\beta$  of the form  $4W_{\alpha\beta}\phi_\alpha\phi_\beta$  is suggested, where  $W_{\alpha\beta}$  is the height of the barrier. The homogeneous free energy with this barrier then becomes:

$$f(\{c\}, \{\phi_1, \phi_2, \dots, \phi_N\}, T) = \sum_{\alpha=1}^N \phi_\alpha f_\alpha(\{c\}, T) + \sum_{\beta \neq \alpha} 4W_{\alpha\beta} \phi_\alpha \phi_\beta \quad (2.16)$$

Eq. 2.16 is similar to the regular solution model, but applied phase fractions instead of mole fractions, and the new barrier term  $4W_{\alpha\beta}\phi_\alpha\phi_\beta$  functions like a positive enthalpy of mixing for phases.

## 2.2 Component evolution

Component evolution equations are derived here for a non-ideal ternary system characterized by a free energy functional. Extension to systems with more components (or fewer, a binary system) follows the same approach but becomes algebraically tedious. Parts of this derivation were drawn from nonlinear diffusion papers by Nauman and Balsara [13] and Nauman and He [14, 15].

The thermodynamic condition defining equilibrium in phase-separating systems is the elimination of all chemical potential gradients. Fickian diffusion with  $\nabla c$  as the driving force applies only to the special case of an ideal system where there is no enthalpy of mixing. Systems which undergo phase separation exhibit “uphill diffusion”, and Fickian diffusion must not hold for these non-ideal systems. To derive component evolution equations for a system characterized by a free energy functional,

it is necessary to begin with the generalized form of Fick's first law:

$$\vec{J}_i = -M_i \nabla \mu_i \quad (2.17)$$

$J_i$  is the flux of component  $i$ ,  $M_i$  is its mobility, and  $\mu_i$  is its diffusion potential. In principle  $J_i$  might also depend the diffusion potential gradients of other components besides  $i$ , but this work focuses on the case where diffusivity is a scalar quantity and there is no cross-diffusion. Emmanuel et al. have derived nonlinear diffusion equations for non-ideal systems where diffusivity is a tensor quantity [16].

$M_i$ , the mobility of component  $i$ , is related to the diffusivity  $D_i$  by the Nernst-Einstein relation:

$$M_i = \frac{D_i c_i}{RT} \quad (2.18)$$

where  $RT$  sets the energy scale of the system. The diffusivity  $D_i$  is a macroscopic quantity determined by the random walks of microscopic particles, according to the relationship  $D = \Gamma \langle r^2 \rangle / 6$  [17].  $\Gamma$  is a local jump attempt rate that could be a function of composition, and  $\langle r^2 \rangle$  is the mean squared jump distance. If  $\Gamma$  is assumed to be a weak function of composition,  $c_i$  will be the leading term in the mobility expression.

It is sensible that mobility should be proportional to  $c_i$  because when the mole fraction of a component approaches zero, the flux of that component must also approach zero. If mobility did not depend on  $c_i$ , it would be possible to have a flux of a component without any of that component being present, behavior that is not possible for conserved quantities. An alternative justification of the form of the component flux equation comes from combining the Einstein relation with the definitions of flux and mobility, and is presented in an endnote.<sup>2</sup>

### 2.2.1 Equivalence of Gibbs and Helmholtz potentials

Chemical potential is defined only at equilibrium once the natural variables of  $f_\alpha$  have been specified. Gibbs free energy is minimized if temperature and pressure

are held constant, but if temperature and volume are held constant Helmholtz free energy is minimized. The fundamental relations (Euler integrals) for molar Gibbs and Helmholtz energies, respectively, are:

$$\bar{G} = \sum_i \mu_i c_i \quad (2.19a)$$

$$\bar{A} = -P\bar{V} + \sum_i \mu_i c_i \quad (2.19b)$$

The Euler integrals show how the Gibbs and Helmholtz potentials differ only by a constant term  $P\bar{V}$ , where  $\bar{V}$  is molar volume. In many phase-field simulations the system is assumed to be incompressible, meaning that volume does not change with pressure. In such a system constant volume and constant pressure are equivalent,  $d\bar{G} = d\bar{A}$ , and minimization is the same under either potential.

### 2.2.2 Generalized diffusion potential

When interfaces are present at equilibrium, the free energy functional  $F$  is minimized instead of Gibbs or Helmholtz energy.  $F$  may be thought of a Gibbs or Helmholtz energy plus nonequilibrium terms that depend on concentration and phase gradients:

$$F = G + \int_V \left( \sum_{\alpha, \beta=1}^{N-1} \frac{1}{2} \lambda_{\alpha\beta} \nabla \phi_\alpha \cdot \nabla \phi_\beta + \sum_{i, j=1}^{M-1} \frac{1}{2} \kappa_{ij} \nabla c_i \cdot \nabla c_j \right) dV \quad (2.20)$$

The Gibbs energy can be treated with equilibrium thermodynamics, but the presence of gradient terms requires a nonequilibrium treatment. Thus it is desirable to define a quantity, the generalized diffusion potential, that will account for gradients and become uniform across an interface at equilibrium. In the same way that a functional is a generalization of a function, the functional derivative is a generalization of a

partial derivative. Since  $F$  is a functional, the functional derivative<sup>2</sup> can be used to define generalized diffusion potentials, which are fields:

$$\tilde{\mu}_1 = \left( \frac{\delta F}{\delta n_1} \right)_{T,P,n_2,n_3}, \quad \tilde{\mu}_2 = \left( \frac{\delta F}{\delta n_2} \right)_{T,P,n_1,n_3}, \quad \tilde{\mu}_3 = \left( \frac{\delta F}{\delta n_3} \right)_{T,P,n_1,n_2} \quad (2.22)$$

$n_i$  is the number of moles of component  $i$ , and tilde notation indicates that the generalized diffusion potential  $\tilde{\mu}_i$  is a different quantity from the chemical potential:

$$\mu_i = \left( \frac{\partial G}{\partial n_i} \right)_{T,P,n_j \neq i} \quad (2.23)$$

In the absence of concentration gradients, the variational derivatives in Eq. 2.22 become partial derivatives, and the generalized diffusion potential is equivalent to the chemical potential. Therefore  $\tilde{\mu}_i = \mu_i$  in bulk single-phase regions at equilibrium. Furthermore, because  $\tilde{\mu}_i$  is the driving force for diffusion in a system with gradient energies, it becomes uniform at equilibrium. Thus the generalized diffusion potential approaches the chemical potential everywhere as equilibrium is approached, even when diffuse interfaces are present.

The fundamental relation for the ternary free energy functional  $F$  at constant temperature and pressure can now be written as:

$$\bar{F} = \frac{F}{n} = \tilde{\mu}_1 c_1 + \tilde{\mu}_2 c_2 + \tilde{\mu}_3 c_3 \quad (2.24)$$

where  $n = n_1 + n_2 + n_3$  is the total number of moles in the system, and  $\bar{F}$  is a molar quantity. The number of moles in the system is an independent quantity that must be defined, and it is convenient to define  $n = 1$  so that  $\bar{F} = F$ .

---

<sup>2</sup> The variational derivative of a functional  $F[y] = \int_V L(y, \nabla y) dV$ , where  $y$  is a spatially varying field, is found using the Euler-Lagrange equation:

$$\frac{\delta F}{\delta y} = \frac{\partial L}{\partial y} - \nabla \cdot \frac{\partial L}{\partial \nabla y} \quad (2.21)$$



It can be shown by standard thermodynamic arguments that the generalized diffusion potentials obey a generalized Gibbs-Duhem relation<sup>3</sup> that places a constraint on how the chemical potentials may vary. At constant temperature and pressure, this relation is:

$$\sum c_i d\tilde{\mu}_i = 0 \quad (2.25)$$

Application of the mole fraction constraint (Eq. 2.5) to Eq. 2.24 to eliminate  $c_3$  reveals that the variational derivatives of  $\bar{F}$  are related to a differences in generalized diffusion potentials:

$$\left(\frac{\delta\bar{F}}{\delta c_1}\right)_{T,P,c_2} = \tilde{\mu}_1 - \tilde{\mu}_3 \quad (2.26a)$$

$$\left(\frac{\delta\bar{F}}{\delta c_2}\right)_{T,P,c_1} = \tilde{\mu}_2 - \tilde{\mu}_3 \quad (2.26b)$$

### 2.2.3 Evolution equations

The derivation of evolution equations begins with the observation that when individual chemical potentials are defined, their gradients are linked by the Gibbs-Duhem equation [18]. If local thermodynamic equilibrium is assumed, the Gibbs-Duhem equation relates gradients in chemical potential  $\nabla\mu_i$  instead of changes in chemical potential  $d\mu_i$ . The assumption of local equilibrium implies that global intensive parameters vary so slowly that small neighborhoods around a point can be considered at equilibrium. For a system not at global equilibrium, local equilibrium is a necessary assumption for chemical potential to be defined.

In section 2.2.2, the generalized diffusion potential  $\tilde{\mu}$  was defined as the quantity which becomes uniform at equilibrium for a system with gradient energies. If a local equilibrium assumption is made, the generalized Gibbs-Duhem relation can be written to relate gradients in generalized diffusion potential. For a ternary system at constant

---

<sup>3</sup>The Gibbs-Duhem equation is:  $\sum n_i d\mu_i = -SdT + VdP$

temperature and pressure, this generalized Gibbs-Duhem relation is:

$$c_1 \nabla \tilde{\mu}_1 + c_2 \nabla \tilde{\mu}_2 + c_3 \nabla \tilde{\mu}_3 = 0 \quad (2.27)$$

The mole fraction constraint (Eq. 2.5) can be used to eliminate  $c_3$ , and the equation can be rearranged to put  $\nabla \tilde{\mu}_1$  on the left hand side:

$$\begin{aligned} \nabla \tilde{\mu}_1 &= (\nabla \tilde{\mu}_1 - \nabla \tilde{\mu}_3) - c_1(\nabla \tilde{\mu}_1 - \nabla \tilde{\mu}_3) - c_2(\nabla \tilde{\mu}_2 - \nabla \tilde{\mu}_3) \\ &= (1 - c_1)\nabla(\tilde{\mu}_1 - \tilde{\mu}_3) - c_2\nabla(\tilde{\mu}_2 - \tilde{\mu}_3) \end{aligned} \quad (2.28)$$

The variational derivatives (Eq. 2.26) can now be substituted in place of the chemical potential differences:

$$\nabla \tilde{\mu}_1 = (1 - c_1)\nabla \frac{\delta \bar{F}}{\delta c_1} - c_2 \nabla \frac{\delta \bar{F}}{\delta c_2} \quad (2.29a)$$

The same procedure can be used to find  $\nabla \tilde{\mu}_2$  in terms of the variational derivatives of  $\bar{F}$ :

$$\nabla \tilde{\mu}_2 = (1 - c_2)\nabla \frac{\delta \bar{F}}{\delta c_2} - c_1 \nabla \frac{\delta \bar{F}}{\delta c_1} \quad (2.29b)$$

Combining Fick's second law and generalized first law (Eq. 2.17) with the Nernst-Einstein relation (Eq. 2.17) and the expression for the chemical potential gradients (Eq. 2.29) produces the ternary evolution equations:

$$\frac{\partial c_1}{\partial t} = \nabla \cdot \left( \frac{D_1 c_1}{RT} \left( (1 - c_1)\nabla \frac{\delta \bar{F}}{\delta c_1} - c_2 \nabla \frac{\delta \bar{F}}{\delta c_2} \right) \right) \quad (2.30a)$$

$$\frac{\partial c_2}{\partial t} = \nabla \cdot \left( \frac{D_2 c_2}{RT} \left( (1 - c_2)\nabla \frac{\delta \bar{F}}{\delta c_2} - c_1 \nabla \frac{\delta \bar{F}}{\delta c_1} \right) \right) \quad (2.30b)$$

The variational derivative  $\frac{\delta \bar{F}}{\delta c_i}$  which appears in the component evolution equations is found by defining the number of moles in the system and then applying the Euler-

Lagrange equation (Eq. 2.21) to the free energy functional (Eq. 2.14):

$$\frac{\delta \bar{F}}{\delta c_i} = \sum_{\alpha=1}^N \phi_{\alpha} \frac{\partial f_{\alpha}}{\partial c_i} - \sum_{j=1}^{M-1} \kappa_{ij} \nabla^2 c_j \quad (2.31)$$

## 2.3 Phase evolution equations

The purpose of the phase fractions introduced in section 2.1.4 is to associate each region of a microstructure with a specific free energy curve. Phase fractions are not constrained by thermodynamics, and phase is not a conserved quantity, as phases are created and destroyed in phase transitions. In a nucleation event for example, appearance of the nucleating phase is expected without any of the phase being present initially. Evolution of the phase fractions follows Allen-Cahn dynamics, which was originally used to describe a non-conserved order parameter in anti-phase domain coarsening [19]:

$$\frac{\partial \phi_{\alpha}}{\partial t} = -\frac{1}{\tau_{\alpha}} \frac{\delta F}{\delta \phi_{\alpha}} \quad (2.32)$$

$\tau_{\alpha}$  is a relaxation time associated with how quickly the  $\alpha$ -phase can transform to another phase. It affects the velocity of moving  $\alpha$  interfaces.

$\frac{\delta F}{\delta \phi_{\alpha}}$  is found by applying the Euler-Lagrange equation (Eq. 2.21) to the multiphase multicomponent free energy functional (Eq. 2.14):

$$\frac{\delta F}{\delta \phi_{\alpha}} = f_{\alpha} - f_N - \sum_{\beta=1}^{N-1} \lambda_{\alpha\beta} \nabla^2 \phi_{\beta} \quad (2.33)$$

$f_N$  is the free energy function of the implicitly defined  $N^{\text{th}}$  phase and appears because  $\frac{\partial \phi_N}{\partial \phi_{\alpha}} = -1$  due to the phase fraction constraint. The driving force for phase separation is a difference in homogeneous free energy functions, and this force is balanced by diffusive terms that introduce a phase surface energy.

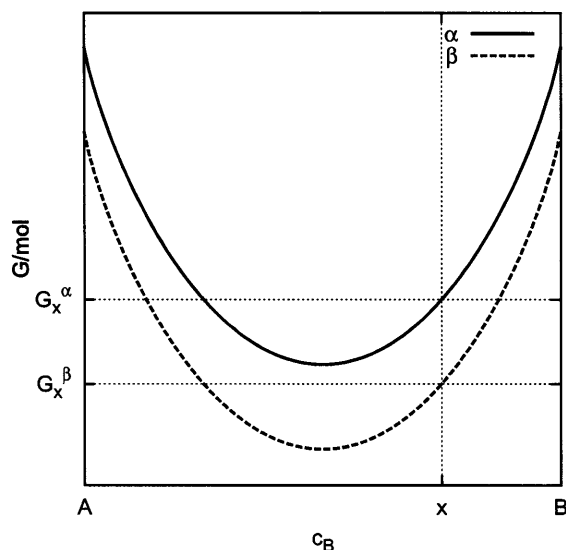


Figure 2-2: For a homogeneous system of composition  $c_B = x$ , converting phase  $\alpha$  to phase  $\beta$  decreases free energy by an amount  $G_x^\beta - G_x^\alpha$ .

### 2.3.1 A problem with the phase equations

The definition of the phase fraction as a positive quantity less than or equal to 1 imposes a constraint on the phase evolution equations (Eq. 2.33) which was not included in their derivation. In fact, negative phase fractions would be energetically favorable if they had physical meaning<sup>4</sup>. To illustrate this point, free energy curves are drawn in Fig. 2-2 for a binary system with two phases,  $\alpha$  and  $\beta$ . For a homogeneous system of composition  $c_B = x$ , converting  $\alpha$  to  $\beta$  always decreases free energy by  $G_x^\beta - G_x^\alpha$ . Imagine now a two phase system consisting of 150%  $\beta$  and -50%  $\alpha$ . This hypothetical system obeys the phase constraint that all phase fractions add to 1 (Eq. 2.11), but the energy is less than if the system were 100%  $\beta$ , the low energy phase. This situation represents arbitrage where the system can always lower its free energy by producing more of the lowest energy phase while creating negative high energy phase. The problem from an energy minimization perspective is that the global

<sup>4</sup>In systems where borrowing is allowed, negative percentages have meaning. Consider financial leveraging - taking out a loan to make an investment. It could be profitable to say, invest 150% of your income by taking out a -50% loan, if you expect the return on the investment to be higher than the interest due on the loan.

energy minima are not contained within the bounds of the constraint.

Phase-field models typically avoid addressing the phase constraint problem by constructing  $f(c, \phi)$  so that it has steep slopes for  $\phi < 0$  and  $\phi > 1$  to discourage but not prohibit the formation of negative phases. Such a restriction is computationally useful but not a physical requirement for modeling phase fractions. Furthermore, restrictions on the form of the interpolating function makes it particularly difficult to construct a function for handling an arbitrary number of phases. For this reason the WBM model has not been extended to handle more than two free energy curves.

Interestingly, the constraint for the component evolution equations (Eq. 2.30) is built-in, a side effect of their thermodynamic derivation.  $c$  is confined to the range  $[0, 1]$  by the  $c(1 - c)$  term in the component equations that insures the flux of a component goes to zero as its mole fraction goes to  $c = 0$  or  $c = 1$ . In practice however, numerically solving a diffusion equation where the flux becomes zero at just one point is challenging. Any small step over the boundary results in negative mole fractions and ill-posed diffusion equations. Overstepping the boundary can be avoided with an appropriately constructed free energy density. It is justifiable for the free energy density function to include  $c \ln c$  terms to account for the entropy of mixing, and these terms cause the free energy density to approach the boundary with infinite slope. The combination of  $c \ln c$  terms and a free energy density with large or infinite slopes at the boundaries was found to be sufficient for solving the component equations.

### 2.3.2 A barrier function for phase fractions

The issue of constraints can be addressed with concepts from the field of linear programming [20]. Barrier methods that convert a constrained problem into a sequence of unconstrained problems are often applied to minimization problems subject to one or more inequality constraints. Phase-field can be thought of as an energy minimization problem (or entropy maximization, the dual case) under a set of physical

constraints. Unlike many optimization problems where only the location of the minimum is desired, in phase-field modeling the path taken to reach the energy minimum is very important because it is described by kinetics. Therefore any phase fraction constraint should ideally not affect the kinetics of the model except exactly at the constraint boundary.

Barrier methods define a feasible region of phase space where the set of constraints are not violated. A barrier function is then defined in the feasible region, and it adds a high cost for approaching the boundary from within the feasible region. the barrier function must be continuous and usually approaches  $\infty$  near the boundary as one of the constraints approaches zero. Constrained optimization then consists of minimizing the sum of the original potential and the barrier functions representing the inequality constraints. Logarithms<sup>5</sup> and  $\frac{1}{x}$  inverse functions are commonly used barriers. These barrier functions however are not ideal candidates for phase fractions which spend a lot of time in the vicinity of  $\phi = 0$  where the barriers are undefined. Single phase-regions in a multiphase system would be unstable for instance, as would any evolution directed along the boundary of the feasible region, which corresponds to a phase transition. Finally, the functions are non-zero in the feasible region and will therefore affect the kinetic path a phase-field system takes.

A cutoff barrier function is proposed here for constraining phase fractions and its algorithmic implementation for a multiphase system will be presented. The barrier function is zero everywhere inside the feasible region and on the boundary, but infinite everywhere outside the feasible region. This type of barrier, under the name double obstacle potential, has previously been studied in a mathematical context by Blowey and Elliott [21], who used asymptotic analysis to show that the barrier was consistent with curvature dependent phase boundary motion. The double obstacle is useful in practice because it can be combined with other arbitrary barrier functions yet still enforces the necessary boundary conditions [22, 23]. An algorithmic implementation

---

<sup>5</sup>In fact, the  $x \ln(x)$  terms in the ideal entropy of mixing are a barrier function for components that has a thermodynamic justification.

---

**Algorithm 1** cutoffBarrier2D( $\phi_1$ )

---

```

if  $\phi_1 < 0$  then
   $\phi_1 \leftarrow 0$ 
else if  $1 - \phi_1 < 0$  then
   $\phi_1 \leftarrow 1$ 
end if

```

---

of the barrier, however, has not been rigorously developed, and is presented here for a system of  $N$  order parameters that obey a mass constraint (Eq. 2.11).

First, the phase fraction constraint problem must be formulated as a set of inequalities. Because an  $N$ -phase system has only  $N - 1$  independent phase fractions, enforcing that all  $N$  phase fractions remain positive is enough to insure that all  $N$  phase fractions will also be less than 1. Recall that the implicitly defined  $N^{\text{th}}$  phase is defined by the phase fraction constraint (Eq. 2.11):

$$\phi_N = 1 - \sum_{\alpha=1}^{N-1} \phi_\alpha \quad (2.34)$$

Enforcing that  $\phi_N$  remain positive insures that no  $\phi_\alpha$  can be greater than 1.

For a two-phase system there is only one independent phase fraction  $\phi_1$ , and performing the projection is simple. If  $\phi_1$  becomes negative after an iteration, set  $\phi_1 = 0$ . On the other hand if  $1 - \phi_1$  becomes negative, set  $\phi_1 = 1$ . The procedure is written in algorithmic notation in Algorithm 1.

Applying the cutoff barrier to a system with more than two phases is more complicated. The phases in an  $N$ -phase system form the vertices of an  $N$ -simplex, and the feasible set of phase fractions lie on or within this simplex. The boundary conditions are implemented by projecting a vector of phase fractions back onto the surface of the simplex when one or more phase fractions becomes negative as a result of timestepping the evolution equations.

Fig. 2-3 offers a geometric description of the cutoff projection for a three-phase system. Orthogonal axes are drawn to represent the two independent phase fractions

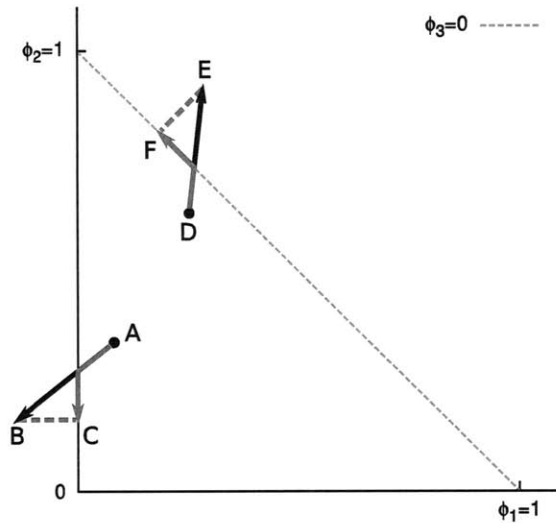


Figure 2-3: Illustration of the cutoff barrier function for a three-phase system.

$\phi_1$  and  $\phi_2$ , and each coordinate in the graph corresponds to a unique point in phase space.  $\phi_1$  and  $\phi_2$  must be positive, so the feasible region lies in the first quadrant. The dependent phase fraction  $\phi_3$  introduces additional constraints. At the origin  $\phi_3 = 1$ , and  $\phi_3 = 0$  corresponds to the dashed line connecting  $\phi_1 = 1$  and  $\phi_2 = 1$ . The constraint that all three  $\phi$  be positive restricts the feasible region to the triangle with vertices at the origin,  $\phi_1 = 1$ , and  $\phi_2 = 1$ . Any point outside of this triangle is non-physical and is given an infinite energy penalty by the cutoff barrier.

Two potential violations and the appropriate projection fix are illustrated in Fig. 2-3. Suppose a system at point A evolves one timestep and lands outside the feasibility triangle at point B. Point B is a violation because  $\phi_1 < 0$ , so B is projected onto the  $\phi_1 = 0$  surface to point C which lies on the  $\phi_2$ -axis. The effect of the projection is to set the negative  $\phi_1$  to zero. The projection has reduced the three-phase system to a two-phase system, and it is now necessary to check that C falls within the feasible region for a two-phase system. This is done by applying the 2D cutoff procedure to  $\phi_2$  and  $\phi_3$ . In the example there are no additional violations to fix because C lies on the feasible triangle, and the original straight line path AB is replaced by the bent path AC.



---

**Algorithm 2** cutoffBarrier3D( $\phi_1, \phi_2$ )

---

```

if  $\phi_1 < 0$  then
   $\phi_1 \leftarrow 0$ 
end if
if  $\phi_2 < 0$  then
   $\phi_2 \leftarrow 0$ 
end if
 $\phi_3 \leftarrow 1 - \phi_1 - \phi_2$ 
if  $\phi_3 < 0$  then
   $\phi_1 \leftarrow \phi_1 + \frac{\phi_3}{2}$ 
  cutoffBarrier2D( $\phi_1$ )
   $\phi_2 \leftarrow 1 - \phi_1$ 
end if

```

---

A more complicated violation occurs when the dependent phase fraction  $\phi_3$  becomes negative after an iteration. An example of this is illustrated in Fig. 2-3, where point D is evolved to point E. The negative  $\phi_3$  must be corrected, but  $\phi_3$  is implicitly defined and cannot explicitly be set to zero. Point E must be projected onto the  $\phi_3 = 0$  surface by moving in the direction  $(-1, -1)$ . This corresponds to subtracting equal quantities from  $\phi_1$  and  $\phi_2$  to make  $\phi_3 = 0$ . After projection onto the  $\phi_3 = 0$  surface, the 2D constraint must then be applied to  $\phi_1$  and  $\phi_2$ . Algorithm 2 presents implementation of the barrier for a three-phase constraint system.

Generalization of the projection procedure for an N-phase system involves fixing violations and then recursively projecting the system to lower dimensions to fix additional violations until the system has been projected back onto the simplex. The recursive procedure for an N-phase system is given in Algorithm 3.

## 2.4 Relationship between material properties and phase-field parameters

In order to simulate real materials systems it is necessary to relate the parameters in the phase-field model to physical quantities. The physical quantities that arise

---

**Algorithm 3** cutoffBarrier( $N, \{\phi_1, \dots, \phi_{N-1}\}$ )
 

---

```

for  $\phi_i = \phi_1 \dots \phi_{N-1}$  do
  if  $\phi_i < 0$  then
     $\phi_i = 0$ 
  end if
end for
 $\phi_N \leftarrow 1 - \sum_{i=1}^{N-1} \phi_i$ 
if  $\phi_N < 0$  then
  for  $\phi_i = \phi_1 \dots \phi_{N-2}$  do
     $\phi_i \leftarrow \phi_i + \frac{\phi_N}{N-1}$ 
  end for
  cutoffBarrier( $N - 1, \{\phi_1, \dots, \phi_{N-2}\}$ )
   $\phi_{N-1} \leftarrow 1 - \sum_{i=1}^{N-2} \phi_i$ 
end if

```

---

in studies of microstructure are the Gibbs free energy of each phase as a function of composition and temperature, the interfacial energy at phase boundaries, and the diffusivity of the components in each phase. The simulation parameters in the phase-field model are the homogeneous free energy densities for each phase  $f_\alpha(c)$ , the gradient energy coefficient matrices  $\lambda_{\alpha\beta}$  and  $k_{ij}$ , and the diffusivities  $D_i$ . The free energy functions and diffusivities in the model are directly equivalent to the physically measured quantities. The free energy functions are commonly obtained from CALPHAD databases and diffusivities can be obtained from DICTRA databases or the NIST mobility database. Diffusivity could in principle be a matrix, as is the case with coupled diffusion, and it is not uncommon for the diffusion constant to be composition dependent in multicomponent systems. A diffusivity dependent on concentration is important for some materials systems and gives rise to phenomena such as the Kirkendall effect.

Unfortunately it is only possible to calculate an analytic expression for surface energy in phase-field models with very simple free energy functions. For the case of arbitrary free energy functions, interfacial energy must be computed numerically. In general, surface energy in a diffuse interface model has two contributions. One contribution comes from the sharp gradients which are present at the interface, and

the other results from composition straying from its equilibrium values at the interface as illustrated in figure 1-1. The surface energy of a diffuse interface is the difference between the free energy functional and the free energy the system would have if the properties of the phases were continuous throughout. Surface energy is calculated by numerical integration across an interface at equilibrium:

$$\sigma = \int_V F[f, c, \phi] - (\mu_1^e c_1 + \mu_2^e c_2 + \mu_3^e c_3) dV \quad (2.35)$$

$\mu_i^e$  is the chemical potential of component  $i$  at equilibrium, and will be the same in all phases. The  $\mu_i^e$  can either be found by computing the tangent plane to the free energy curves or by numerically relaxing an interface and computing the  $\mu_i^e$  (using Eq. 2.19a and Eq. 2.26) away from the interface in the bulk, where there are no gradients in phase or composition. Where no gradients are present, the functional derivative is equivalent to the partial derivative and equilibrium chemical potentials can be calculated.

## Notes

<sup>1</sup>The Taylor Polynomial of degree  $m$  for a function  $f(\vec{x})$  of  $n$  variables, evaluated at  $\vec{a}$  is [24]:

$$P_m(\vec{x}) = \sum_{|J| \leq m} \frac{1}{J!} (D_J f)(\vec{a}) (\vec{x} - \vec{a})^J \quad (2.36)$$

$J$  is a sequence  $J = (j_1, j_2, \dots, j_n)$  of nonnegative integers with  $|J| = j_1 + j_2 + \dots + j_n$  and  $J! = j_1! j_2! \dots j_n!$ , and  $(\vec{x} - \vec{a})^J = (x_1 - a_1)^{j_1} (x_2 - a_2)^{j_2} \dots (x_n - a_n)^{j_n}$ .  $D_J$  is a differential operator: of the

$$D_J = \frac{\partial^k}{\partial x_1^{j_1} \partial x_2^{j_2} \dots \partial x_n^{j_n}} \quad (2.37)$$

<sup>2</sup>An alternative derivation of the flux of a component starts with the definition of flux as the product of a density  $\sigma$  and a drift velocity  $v_d$ :

$$J = \sigma v_d \quad (2.38)$$

The drift velocity (or root mean squared velocity)  $v_d$  is defined as the product of a driving force  $F$  and a mobility  $M$ :

$$v_d = FM \quad (2.39)$$

The Einstein relation connecting diffusivity and mobility is:

$$D = MkT \quad (2.40)$$

Combination of equations 2.39, 2.38, and 2.40 produces:

$$J = \sigma F \frac{D}{kT} \quad (2.41)$$

For a system of diffusing particles with constant volume, the density  $\sigma$  is the same as the concentration  $c$ , the driving force is a chemical potential gradient  $F = \nabla\mu$ , and  $k = R$ , where  $R$  is the universal gas constant. Thus:

$$J = \frac{Dc}{RT} \nabla\mu \quad (2.42)$$

## References

- [1] John W. Cahn and John E. Hilliard. Free energy of a nonuniform system. i. interfacial free energy. *Journal of Chemical Physics*, 28(2):258–267, 1958.
- [2] DJ Eyre. Systems of cahn-hilliard equations. *SIAM JOURNAL ON APPLIED MATHEMATICS*, 53(6):1686–1712, DEC 1993.
- [3] C. M. Elliott and H. Garcke. Diffusional phase transitions in multicomponent systems with a concentration dependent mobility matrix. *Physica D*, 109(3-4):242–256, 1997.
- [4] PR Cha, DH Yeon, and JK Yoon. A phase field model for isothermal solidification of multicomponent alloys. *ACTA MATERIALIA*, 49(16):3295–3307, SEP 20 2001.

- [5] RJ Zhang, T Jing, WQ Jie, and BC Liu. Phase-field simulation of solidification in multicomponent alloys coupled with thermodynamic and diffusion mobility databases. *ACTA MATERIALIA*, 54(8):2235–2239, MAY 2006.
- [6] J. W. Morris. The influence of a concentration gradient on the free energy of a binary solution. *Philosophical Magazine*, 23(185):1041–1052, 1971.
- [7] MV Ariyapadi and EB Nauman. Free-energy of an inhomogeneous polymer polymer solvent system .2. *JOURNAL OF POLYMER SCIENCE PART B-POLYMER PHYSICS*, 30(6):533–538, 1992. Cited References Count:13.
- [8] Didier DeFontaine. *A computer simulation of the evolution of coherent composition variations in solid solutions*. PhD thesis, Northwestern University, 1967.
- [9] J.E. Morral and J.W. Cahn. Spinodal decomposition in ternary systems. *Acta Metallurgica*, 19:1037–1045, 1971.
- [10] J. J. Hoyt. Spinodal decomposition in ternary alloys. *Acta Metallurgica*, 37(9):2489–2497, 1989.
- [11] David J. Eyre. Cascades of spinodal decompositions in the ternary cahn-hilliard equations. In *Mathematics of Microstructure Evolution*, pages 367–378, 1996.
- [12] E.A. Guggenheim. *Thermodynamics: an advanced treatment for chemists and physicists*. North-Holland Publishing Company, 1967.
- [13] E. B. Nauman and N. P. Balsara. Phase-equilibria and the landau-ginzburg functional. *Fluid Phase Equilibria*, 45(2-3):229–250, 1989. 14 ELSEVIER SCIENCE BV U3176.
- [14] E. B. Nauman and D. Q. He. Morphology predictions for ternary polymer blends undergoing spinodal decomposition. *Polymer*, 35(11):2243–2255, 1994.

- [15] EB Nauman and DQ He. Nonlinear diffusion and phase separation. *CHEMICAL ENGINEERING SCIENCE*, 56(6):1999–2018, MAR 2001.
- [16] S. Emmanuel, A. Cortis, and B. Berkowitz. Diffusion in multicomponent systems: a free energy approach. *Chemical Physics*, 302(1-3):21–30, 2004.
- [17] Robert W. Balluffi, Samuel M. Allen, and W. Craig Carter. *Kinetics of Materials*. John Wiley & Sons, Inc., 2005.
- [18] J. W. Cahn and F. C. Larche. An invariant formulation of multicomponent diffusion in crystals. *Scripta Metallurgica*, 17(7):927–932, 1983.
- [19] SM Allen and JW Cahn. Microscopic theory for antiphase boundary motion and its application to antiphase domain coarsening. *ACTA METALLURGICA*, 27(6):1085–1095, 1979.
- [20] Dimitri P. Bertsekas. *Nonlinear Programming*. Athena Scientific, 1999.
- [21] J.F. Blowey and C.M. Elliott. Curvature dependent phase boundary motion and parabolic double obstacle problems. *The IMA Volumes in Mathematics and its Applications*, 47, 1993.
- [22] H. Garcke, B. Nestler, and B. Stoth. A multiphase field concept: Numerical simulations of moving phase boundaries and multiple junctions. *Siam Journal on Applied Mathematics*, 60(1):295–315, 1999.
- [23] H. Garcke, B. Nestler, and B. Stinner. A diffuse interface model for alloys with multiple components and phases. *Siam Journal on Applied Mathematics*, 64(3):775–799, 2004. 45 SIAM PUBLICATIONS 815EW.
- [24] Lawrence J. Corwin and Robert Henry Szczerba. *Calculus in vector spaces*. Monographs and textbooks in pure and applied mathematics ;. M. Dekker, New York, 2nd edition, 1995. Lawrence J. Corwin, Robert H. Szczerba. ill. ; 24 cm. Includes index.

## Chapter 3

# Numerical methods for phase-field modeling

Computational modeling has often been driven by demonstration of impressive results rather than development of improved models. One of the side effects of the massive increases in computing speed and affordability over the last two decades has been frequent acclaim for simulations that are large, complicated, or pretty but provide few new scientific insights. The 1990's was a particularly notorious time for papers whose major finding was that they had performed the largest known computation. While increases in computing power have no doubt revolutionized computational modeling, there is still wisdom in the careful development of simple models that correctly describe complex behavior.

Phase-field modeling is particularly vulnerable to qualitative verification because, unlike other modeling approaches, obtaining quantitative data from simulations is a major challenge. Incorporating parameters from experiment is not easy, but solving the phase-field equations with these correct parameters presents an even more difficult numerical challenge. Interfaces much thicker than experimentally justifiable are almost always simulated, and phase-field models are evaluated on whether or not they look correct. A detailed discussion can be found in appendix A. Such vague

validation criteria has the negative effect of discouraging meticulous development of models and numerical methods, even though both are needed.

While the goal of chapter 2 was to present a carefully derived phase-field model for studying complex systems, this chapter explores numerical challenges involved in solving the evolution equations. The multiphase, multicomponent model produces a set of coupled nonlinear differential equations that are numerically stiff with a fourth spatial derivative in the diffusion equations. Because the equations are nonlinear and the free energy density is assumed to be arbitrary, an analytic solution of the equations is not possible. Therefore development of numerical methods that estimate and control error is important.

Explicit finite difference and implicit-explicit Fourier spectral methods are considered here, and spectral methods were found to be several orders of magnitude more stable. However, the large timesteps that become possible with semi-implicit integration introduce a significant amount of error. One source of error is the first-order accurate time integrator commonly used in spectral methods, and the other source arises from the dynamics of phase separation itself. Both sources of error are addressed here with a second-order Runge-Kutta time integrator and adaptive timestepping.

Because finite difference is a commonly used method, its application to the multiphase equations will be reviewed and several pitfalls will be highlighted. Appropriate finite difference schemes for the nonlinear diffusion equations will be presented, although the difficulties that arise further increase the appeal of spectral methods.



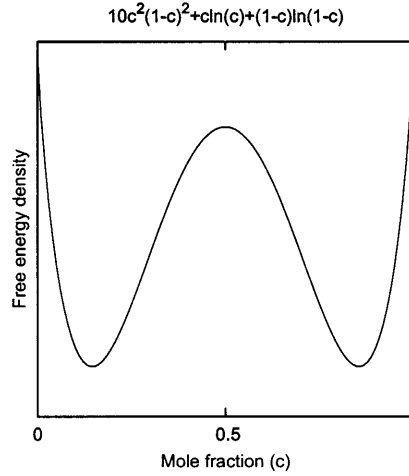


Figure 3-1: The binary double-well free energy function used for numerical analysis.

### 3.1 The phase-field model for numerical analysis

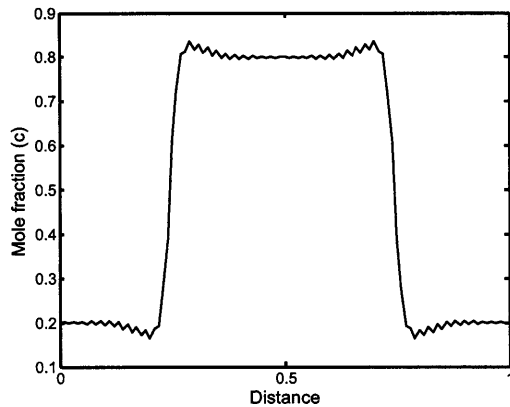
Numerical analysis in this chapter will focus on solving the component diffusion equation for a single-phase binary system:

$$\frac{\partial c}{\partial t} = \nabla \cdot \left( c(1-c) \nabla \left( \frac{\partial f}{\partial c} - \kappa \nabla^2 c \right) \right) \quad (3.1)$$

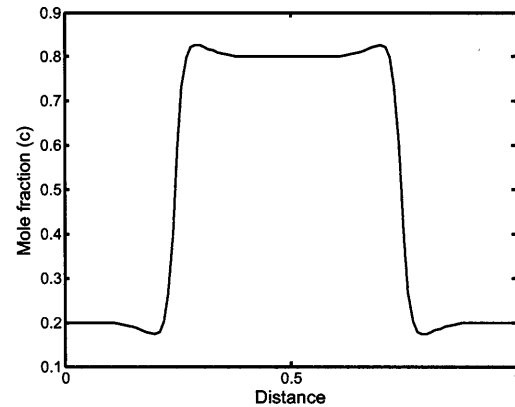
This diffusion equation was chosen because it is the simplest equation that exhibits the numerical difficulties of the multiphase model described in chapter 2. Simulating a multiphase, multicomponent system involves solving a set of coupled equations, but the numerical difficulty lies in the nonlinearity and stiffness of the diffusion equations. The phase evolution equations, in contrast, are less stiff and linear, and are easily treated with a variety of numerical methods. Thus the solution to the numerical challenge should focus on solving the diffusion equations.

The free energy density  $f(c)$  to be used in all calculations is a standard double well with an entropy of mixing:

$$10c^2(1-c)^2 + c \ln c + (1-c) \ln(1-c) \quad (3.2)$$



(a) Evolving interface profile calculated with centered differences.



(b) Evolving interface profile calculated with one forward and one backward difference.

Figure 3-2: Use of the centered finite difference for evaluating the first derivatives in Eq. 3.1 produces zig-zag artifacts which appear while an interface is evolving. They slowly disappear at longer times.

Illustrated in figure 3-1, the function is used to simulate spinodal decomposition in a binary system and has minima near  $c = .15$  and  $c = .85$ .

## 3.2 Finite Difference

Explicit finite difference is perhaps the most commonly used method for solving phase-field equations because it is simple to understand, easy to code, and straightforward to parallelize. But unfortunately it turns out to be a poor choice. To begin with, the diffusion equations are nonlinear and difficult to discretize. Even with a good discretization though, the method suffers from severe instability problems due to the fourth derivative and extremely small timesteps are required.

Discretizing Eq. 3.1 using finite difference is not straightforward. A naive first approach is to use the standard second-order accurate discretization for the first and second spatial derivatives:

$$\nabla c \approx \frac{c_{i+1} - c_{i-1}}{2h} \quad (3.3a)$$

$$\nabla^2 c \approx \frac{c_{i+1} - 2c_i + c_{i-1}}{h^2} \quad (3.3b)$$

However application of the centered first derivative discretization (Eq. 3.3a) twice produces a stretched version of the Laplacian operator that depends on neighboring gridpoints a distance of two grids spacings away:

$$\nabla \cdot \nabla c \approx \frac{c_{i+2} - 2c_i + c_{i-2}}{(2h)^2} \quad (3.4)$$

Although this discretization's spatial convergence is second-order, it is poorly suited for solving diffusion equations. There is no connection between point  $u_i$  and its nearest neighbors, and oscillations on the length scale of the grid spacing can appear during evolution, as illustrated in figure 3-2. These zig-zags are artifacts that slowly disappear at long times and are not predicted by the dynamics of the diffusion equation.

Another problem arises with the centered difference operator if the outer gradient is distributed over the inner nonlinear terms in the following manner:

$$\begin{aligned} \frac{\partial c}{\partial t} &= \nabla \cdot (x \nabla y) = x \nabla^2 y + \nabla x \cdot \nabla y \\ x &= c(1 - c) \\ y &= \frac{\partial f}{\partial c} - k \nabla^2 c \end{aligned} \quad (3.5)$$

Distributing the gradient in this manner may appear advantageous because the equation has been decomposed into the sum of a constant coefficient Cahn-Hilliard equation plus nonlinear terms. However, applying the centered difference operator to  $\nabla x \cdot \nabla y$  leads to a scheme that does not conserve composition. A proof of the loss of conservation can be found in an endnote<sup>3</sup>.

### 3.2.1 Comparison of two finite-difference schemes

A simple solution to the discretization problem is to use a forward difference  $\nabla_+$  for one gradient, and a backward difference  $\nabla_-$  for the other:

$$\begin{aligned}\frac{\partial c}{\partial t} &= \nabla_+ \cdot \left( c(1-c) \nabla_- \left( \frac{\partial f}{\partial c} - \kappa \nabla^2 c \right) \right) \\ \nabla_+ c &\approx \frac{c_{i+1} - c_i}{h} \\ \nabla_- c &\approx \frac{c_i - c_{i-1}}{h}\end{aligned}\tag{3.6}$$

This scheme, called the forward-backward scheme, does not exhibit the aliasing observed with centered differences (figure 3-2b). The forward and backward gradient discretizations are only first-order accurate themselves, but the combination of  $\nabla_+ \cdot \nabla_-$  is known to produce the second-order accurate Laplacian operator (Eq. 3.3b). Although Eq. 3.6 is nonlinear, it is possible that the scheme might exhibit second-order spatial convergence, but it is necessary to numerically verify the spatial convergence of the scheme.

An alternative discretization approach avoids using the centered difference operator entirely. The diffusion equation can be formulated in such a way that only Laplacian finite difference operators are necessary:

$$\begin{aligned}\frac{\partial c}{\partial t} &= \nabla \cdot (x \nabla y) = \frac{1}{2} (\nabla^2(xy) + x \nabla^2 y - y \nabla^2 x) \\ x &= c(1-c) \\ y &= \frac{\partial f}{\partial c} - \kappa \nabla^2 c\end{aligned}\tag{3.7}$$

The derivation of this form is presented in an endnote<sup>4</sup>. This approach has the advantage of being second-order accurate in space because it only uses the second-order Laplacian discretization. It is more computationally expensive than the forward-backward scheme because three Laplacian operators must be evaluated, although the additional cost could be reduced by evaluating the terms in Eq. 3.7 in parallel.

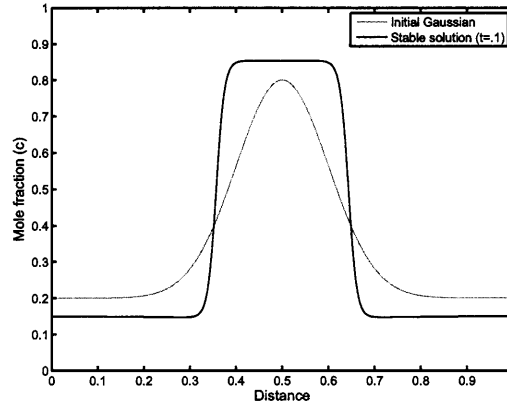


Figure 3-3: Initial and final phase-field solutions used to measure the spatial convergence of finite difference discretization schemes.

A spatial convergence test was performed to evaluate the performance of the two proposed finite difference schemes. To measure discretization error, the Gaussian  $c_0 = .2 + .6e^{-50(c-.5)^2}$  illustrated in figure 3-3 was relaxed to steady state at  $t = .1$  at several different grid resolutions. A Gaussian was chosen as the initial condition because it is a smooth function that can be represented well on coarse grids. Because no analytic solutions to the evolution equation are known, a reference solution was computed on a very fine grid ( $N=2048$ ) and interpolated to the coarser grids ( $N=1024, 512, 256, 128$ ) to measure error. To obtain the reference solution, the right-hand side of the equation was evaluated using the pseudo-spectral approach discussed in section 3.3.2. All solutions were calculated using the fifth-order accurate numerical differentiation formulas (the function `ode15s` in MATLAB) with a maximum timestep of  $1 \times 10^{-5}$ . Error was computed in the  $L_2$  and  $L_\infty$  norms. Because the number of gridpoints is different at each resolution, relative error is reported:

$$\begin{aligned} \|e\|_2 &= \frac{\|c - \tilde{c}\|_2}{\|c\|_2} \\ \|e\|_\infty &= \frac{\|c - \tilde{c}\|_\infty}{\|c\|_\infty} \end{aligned} \quad (3.8)$$

$c$  is the exact solution (i.e. calculated at  $N=2048$ ), and  $\tilde{c}$  is an approximate solution

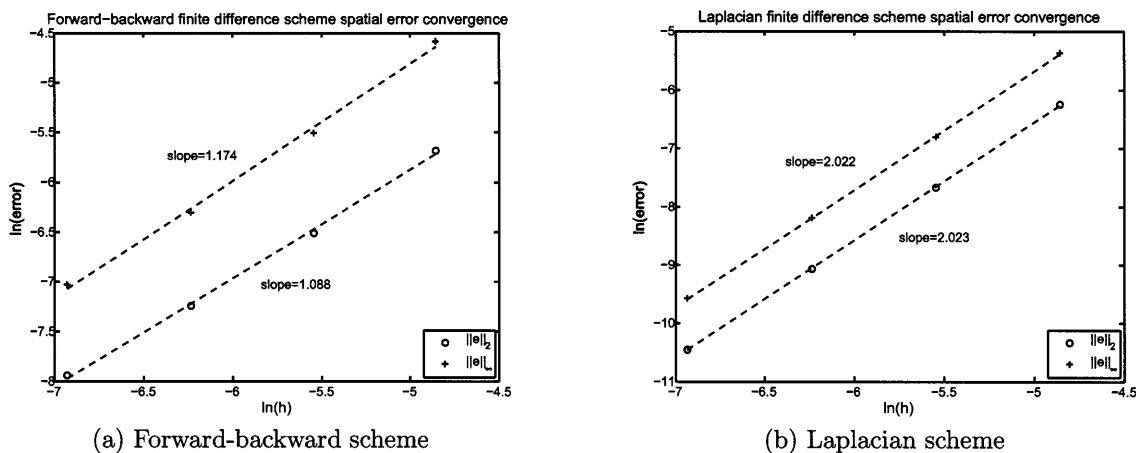


Figure 3-4: Spatial convergence of two different finite different schemes used to solve the nonlinear diffusion equation (Eq. 3.1). The forward-backward scheme (Eq. 3.6) is first-order accurate and Laplacian scheme (Eq. 3.7) is second-order accurate.

calculated on a coarse grid.

Results from the test show that the Laplacian scheme offers better convergence than the forward-backward scheme, although it is more computationally expensive. Figure 3-4 presents the results of the spatial convergence test.  $\ln(e)$  is plotted against  $\ln(h)$ , where  $h$  is the grid spacing, and the slope of the data in these plots is the order of spatial convergence. The slopes, where were measured with linear regression, reveal that the forward-backward difference scheme (Eq. 3.6) is first-order accurate in space, and the Laplacian scheme (Eq. 3.7) is second-order accurate.

### 3.3 Implicit-Explicit spectral methods

Discretization difficulties aside, the major challenge with solving the phase-field diffusion equation is that it is both stiff and nonlinear. The stiffness issue could be addressed with an implicit solver, but many of the usual numerical methods are difficult to apply because of the nonlinearity. The free energy densities are arbitrary functions with no guarantee of invertibility. They might not have symmetric or even

semi-definite Jacobians, and an iterative solver for the implicit equations might be necessary. It could be desirable, then, to handle the nonlinear terms explicitly and the linear terms implicitly. Such a splitting is referred to as an implicit-explicit (or semi-implicit) method and is a common method for solving partial differential equations [1].

Spectral and pseudo-spectral methods have emerged as powerful methods for solving partial differential equations [2, 3, 4]. In particular, the Fourier transform provides a simple and inexpensive way of accurately evaluating spatial derivatives. The implicit solution of a differential equation can be found by a division operation in Fourier space rather than a matrix inversion in real space. The discrete Fourier transform can be computed efficiently for use in numerical computation with the fast Fourier transform (FFT) algorithm. The algorithm scales as  $O(N \ln N)$ , and implementations of the algorithm have been highly optimized to run on modern multi-core computers [5].

The Fourier transform  $\hat{f}(k)$  of a function  $f(x)$  is:

$$F[f(x)] = \hat{f}(k) = \int_{-\infty}^{\infty} f(x)e^{-ikx} dx \quad (3.9)$$

$k$  is a wavenumber and  $\hat{f}(k)$  is the representation of  $f(x)$  in frequency space. The inverse Fourier transform converts  $\hat{f}(k)$  back to  $f(x)$ :

$$F^{-1}[\hat{f}(k)] = f(x) = \frac{1}{2\pi} \int_{-\infty}^{\infty} \hat{f}(k)e^{ikx} dk \quad (3.10)$$

The derivative of  $f'(x)$  in Fourier space can be found by taking the derivative of Eq. 3.10:

$$\begin{aligned} f'(x) &= \int_{-\infty}^{\infty} \frac{\partial}{\partial x} (\hat{f}(k)e^{ikx}) dk = \int_{-\infty}^{\infty} ik \hat{f}(k)e^{ikx} dk \\ &= F^{-1}[ik\hat{f}(k)] \end{aligned} \quad (3.11)$$

Thus the derivative in real space is merely a multiplication by  $ik$  in Fourier space. In addition to avoiding the inconvenience of discretizing a difficult equation, using the Fourier transform to calculate derivatives also offers optimal spatial accuracy. Finite difference only considers nearby neighbors for evaluating a derivative, but Fourier transform methods can be thought of as a finite difference scheme with the largest possible stencil that incorporates all available data.

### 3.3.1 An IMEX splitting for the Cahn-Hilliard equation

The use of implicit-explicit Fourier spectral methods in phase-field became popular after L.Q. Chen and Jie Shen showed that an IMEX spectral method was between two and three times more efficient than explicit finite difference for solving the Cahn-Hilliard equation [6]. They showed that the spectral solver offered better spatial accuracy and was several orders of magnitude more stable, without introducing a significant amount of error. The IMEX method proposed by Chen and Shen will now be reviewed, as it is important to start with a simple example that illustrates how the discrete Fourier transform can be used to efficiently solve a differential equation that has been split into a linear part to be solved implicitly, and nonlinear part to be solved explicitly. The Cahn-Hilliard equation with mobility  $M = 1$  will be used as an example:

$$\frac{\partial c}{\partial t} = \nabla^2 f'(c) - \kappa \nabla^4 c \quad (3.12)$$

$\nabla^2 f'(c)$  is nonlinear and will be integrated explicitly and  $-\kappa \nabla^4 c$  is stiff and linear and will be integrated implicitly to avoid stability problems. A first-order forward Euler discretization is used to approximate the temporal derivative:

$$\frac{c^{n+1} - c^n}{\Delta t} = \nabla^2 f'(c^n) - \kappa \nabla^4 c^{n+1} \quad (3.13)$$



and the discrete Fourier transform is employed to evaluate partial derivatives:

$$\frac{\widehat{c^{n+1}} - \widehat{c^n}}{\Delta t} = -k^2 \widehat{f'(c^n)} - \kappa k^4 \widehat{c^{n+1}} \quad (3.14)$$

Hat notation is used here to indicate the Fourier transform of a quantity (i.e.  $\widehat{c^{n+1}} = F[c^{n+1}]$ ). Eq. 3.14 can be rearranged and solved for  $\widehat{c^{n+1}}$ , the solution at the next timestep:

$$\begin{aligned} \widehat{c^{n+1}} + \Delta t \kappa k^4 \widehat{c^{n+1}} &= \widehat{c^n} - \Delta t k^2 \widehat{f'(c^n)} \\ \widehat{c^{n+1}} &= \frac{\widehat{c^n} - \Delta t k^2 \widehat{f'(c^n)}}{1 + \Delta t \kappa k^4} \\ c^{n+1} &= F^{-1} \left[ \frac{\widehat{c^n} - \Delta t k^2 \widehat{f'(c^n)}}{1 + \Delta t \kappa k^4} \right] \end{aligned} \quad (3.15)$$

With the use of the Fourier transform, the implicit solution to the forward Euler timestep has become a division in Fourier space. The increased stability that results from the implicit solve can be rationalized by noting that the denominator contains only positive terms that will always be greater than one. Dividing by a number greater than one will reduce the amplification of each Fourier mode and tend to promote stability. The IMEX discretization is not unconditionally stable because  $\Delta t$  also appears in the numerator as a result of the explicit treatment of the nonlinear terms. Increasing  $\Delta t$  to large values will amplify frequencies by factors greater than one at each timestep, resulting in instability.  $\left| \frac{1 - \Delta t k^2}{1 + \Delta t \kappa k^4} \right|$  becomes large for large values of  $\Delta t$  and small values of  $k$ .

### 3.3.2 An IMEX splitting for the nonlinear diffusion equation

In Chapter 2, nonlinear diffusion equations were derived for multicomponent, multiphase systems from basic thermodynamic and kinetic arguments. The simplest

diffusion equation is for the case of a binary single phase system:

$$\frac{\partial c}{\partial t} = \nabla \cdot (c(1-c)\nabla (f'(c) - \kappa\nabla^2 c)) \quad (3.16)$$

This equation is the Cahn-Hilliard equation with a mobility that depends on  $c(1-c)$ . The spectral evaluation of the right-hand side is complicated by the fact that the multiplication of two functions in real space is not equivalent to the multiplication of the Fourier transforms of the two functions. Multiplication by  $c(1-c)$  must be performed in real space, and the spectral discretization of Eq. 3.16 involves an additional Fourier transform and inverse transform:

$$\widehat{\frac{\partial c}{\partial t}} = ik \left( F \left[ c(1-c)F^{-1} \left[ ik \left( \widehat{f'(c)} + \kappa k^2 \widehat{c} \right) \right] \right] \right) \quad (3.17)$$

A more serious problem is that the  $c(1-c)$  terms make the entire equation nonlinear, and the IMEX splitting of section 3.3.1 can no longer be applied. Unfortunately, an explicit treatment of Eq. 3.17 exhibits severe timestep restrictions. Zhu and Chen [7] proposed a way to stabilize the equation with the inclusion of a stiff linear term that can be solved implicitly. The term  $-A\nabla^4 c$  is added to the implicit part of the splitting and subtracted from the explicit part in the following manner:

$$\begin{aligned} \frac{\partial c}{\partial t} &= N(c^n) + L(c^{n+1}) \\ N(c) &= A\kappa\nabla^4 c + \nabla \cdot (c(1-c)\nabla (f'(c) - \kappa\nabla^2 c)) \\ L(c) &= -A\kappa\nabla^4 c \end{aligned} \quad (3.18)$$

$N(c^n)$  contains the nonlinear terms to be solved explicitly and  $L(c^{n+1})$  contains the linear term that will be handled implicitly.  $A$  is a constant, and  $A = 0$  corresponds to the original non-stabilized equation. As  $A$  is increased, the equation becomes more stable but less accurate. This is because the splitting is attempting to implicitly solve of a linear portion of the  $c(1-c)\kappa\nabla^4 c$  term, which is the nonlinear fourth-order term

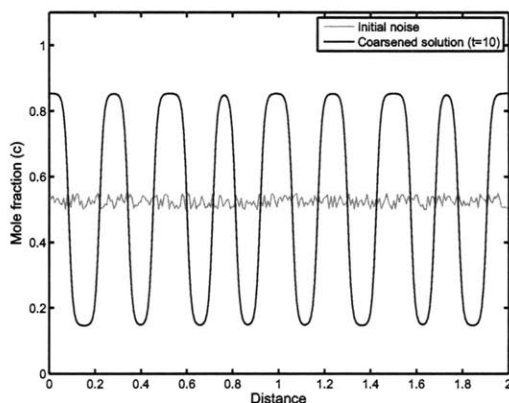


Figure 3-5: Coarsening of random noise was used to measure the accuracy of finite difference and spectral solvers. The initial noise and the coarsened solution at  $t = 10$  are shown. A grid of 256 points with a grid spacing of  $h = 1/128$  was used.

in Eq. 3.16. The implicit stabilization term must have the same sign as this nonlinear term for numerical stability and should be approximately the same magnitude as the nonlinear term to minimize error. Thus the value of  $A$  should be on the order of the average value of  $c(1 - c)$ . Zhu and Chen report that  $A = .5$  was found to work well in practice and produced stability for timesteps orders of magnitude larger than for explicit finite difference.

Using a forward Euler discretization in time, the resulting stabilized equation is:

$$\begin{aligned} \frac{c^{n+1} - c^n}{\Delta t} &= N(c^n) + L(c^{n+1}) \\ \widehat{c^{n+1}} - \widehat{c^n} &= \Delta t \widehat{N(c^n)} - \Delta t A \kappa k^4 \widehat{c^{n+1}} \\ \widehat{c^{n+1}} &= \frac{\widehat{c^n} + \Delta t \widehat{N(c^n)}}{1 + \Delta t A \kappa k^4} \end{aligned} \quad (3.19)$$

Eq. 3.17 must be employed to evaluate  $\widehat{N(c^n)}$ .

		$\Delta t = 2 \times 10^{-7}$		$\Delta t = \Delta t_{max}$	
$A$	$\Delta t_{max}$	$\ e\ _2$	$\ e\ _\infty$	$\ e\ _2$	$\ e\ _\infty$
0	$3 \times 10^{-7}$	—	—	$2.07 \times 10^{-4}$	$8.88 \times 10^{-4}$
.0625	$7 \times 10^{-7}$	$1.40 \times 10^{-4}$	$5.64 \times 10^{-4}$	$5.94 \times 10^{-1}$	$7.32 \times 10^{-1}$
.125	$1 \times 10^{-4}$	$2.88 \times 10^{-4}$	$1.16 \times 10^{-3}$	$6.20 \times 10^{-1}$	$8.28 \times 10^{-1}$
.25	$1 \times 10^{-3}$	$5.92 \times 10^{-4}$	$2.40 \times 10^{-3}$	$7.32 \times 10^{-1}$	$8.27 \times 10^{-1}$
.5	$2 \times 10^{-3}$	$1.22 \times 10^{-3}$	$4.97 \times 10^{-3}$	$7.23 \times 10^{-1}$	$8.29 \times 10^{-1}$
1	$5 \times 10^{-3}$	$2.52 \times 10^{-3}$	$1.03 \times 10^{-2}$	$7.22 \times 10^{-1}$	$8.27 \times 10^{-1}$
finite difference	$2 \times 10^{-6}$	$2.41 \times 10^{-2}$	$9.18 \times 10^{-2}$	$2.40 \times 10^{-2}$	$9.12 \times 10^{-2}$

Table 3.1: Measurements of largest stable timestep and error for different values of the parameter  $A$ . Large values of  $A$  increase stability but decrease accuracy. Using a large timestep introduced a significant amount of error.

### 3.4 Measuring error introduced by the stabilization method

Since the stabilization method introduced in the previous section has altered the diffusion equation with the introduction of a stiff linear term scaled by a constant  $A$ , it is important to measure the effect of  $A$  on the accuracy and stability of the IMEX spectral solver. A representative phase-field simulation involving dampening of sharp gradients followed by phase-separation and then coarsening was performed for different values of  $A$  to quantify its effect. The simulation consisted of randomly generated noise with a value between  $c = .45$  and  $c = .55$  which was coarsened to a time of  $t = 10$ . The initial and final conditions are shown in figure 3-5. All tests were performed using 256 gridpoints and a grid spacing of  $h = 1/128$ . A reference solution was computed using  $A = 0$  and a very small timestep of  $\Delta t = 2 \times 10^{-7}$ . Computing the reference solution took several hours of computing time, even for a 1D grid.

Numerical tests results for several values of  $A$  can be found in table 3.1. The maximum stable timestep is reported for each  $A$ , along with the relative errors for  $\Delta t = 2 \times 10^{-7}$ , the small timestep used to compute the reference solution, and error for the maximum stable timestep. The  $\Delta t = 2 \times 10^{-7}$  error quantifies how  $A$  affects accuracy independent of the timestep, and the  $\Delta t_{max}$  error provides an estimate of

the error introduced by using a large timestep.

Two trends in table 3.1 are clear:  $A$  does not introduce significant error when small timesteps are used, but error increases dramatically as  $A$  is increased and the equation becomes more stable. Errors in the 60-80% range, as were measured in some cases with the maximum stable timestep, are unacceptable for any type of simulation. Since  $A$  by itself only introduces a modest amount of error, the accuracy problem is likely the result of accumulated error from using large timesteps.

### 3.4.1 Discussion

It is surprising that Chen et al. [6], Zhu et al. [7], and the hundreds of papers that have applied their methods have never acknowledged temporal resolution of phase-separation dynamics as a significant source of numerical error. With the potential for errors as high as 80%, the findings of many phase-field papers might be questioned, especially since most papers make no attempt to estimate error. It seems likely that many authors may have overlooked the fact that stability of a numerical method does not imply accuracy. Ignoring error does not make it irrelevant.

Even more unsettling are the unsupported and misleading claims of Chen and Zhu et al. that their methods are more accurate than explicit finite difference, in addition to orders of magnitude more stable. This claim seems to arise from a focus on the improvement in spatial accuracy that spectral methods offer without considering the effect of dynamic temporal error. Chen attempted to measure error while using the largest stable timestep, but did so for a relatively static problem, the formation of an equilibrium diffuse interface from an initially sharp interface. Zhu et al. claim that the use of large timesteps is acceptable but did not measure error for different timesteps. To their credit, both papers did suggest that second and third order accurate time integrators (using a BDF/AB scheme) would increase accuracy, but did not specify whether such schemes were necessary, quantify the accuracy of the schemes, or use higher-order schemes in their own calculations. Furthermore, the data in the previous

section shows that even a higher-order time integrator can still introduce significant error when a large timestep is used to simulate high frequency dynamics.

An interesting finding in table 3.1 is that explicit finite difference does not suffer from accuracy problems, largely because very small timesteps are required for stability, and a consequence of small timesteps is good temporal accuracy. An appropriate argument for using an implicit-explicit spectral method is that it can achieve a desired level of accuracy much more efficiently than explicit finite difference.

The fact that so many phase-field models can be developed using suspect numerical methods highlights one of the pitfalls of phase-field. Phase-field models almost always produce pretty pictures that appear qualitatively correct, even when the model is wrong for many possible reasons. The eye cannot possibly determine whether a model is accurate or not, but pretty pictures have the psychological effect of seeming convincing and discourage careful attention to detail. But carefully derived models are exactly what phase-field needs, as verification of phase-field with appeal to experiment is very difficult.

The following sections will identify two significant sources of error with the stabilization method (Eq. 3.18) and present appropriate fixes: a higher order Runge-Kutta time integrator and adaptive timestep control. The adaptive Runge-Kutta was found to improve the efficiency of Zhu's stabilization technique by two orders of magnitude when a simulation is required to meet acceptable error tolerances.

### **3.5 An adaptive timestep spectral method**

There are two sources responsible for the large errors measured in table 3.1, and each must be addressed separately. First, the forward Euler time discretization used in Eq. 3.19 is only first-order accurate in time. This results in error proportional to the timestep size. The stabilization method has increased the stable timestep by orders of magnitude with the side effect of increasing error by orders of magnitude. One

improvement then is to use a more accurate time integrator.

The Euler time integrator did not cause problems for the finite difference solver because very small timesteps were required to maintain stability. One redeeming feature of explicit finite difference then is that it usually becomes unstable before it becomes inaccurate. The last row of table 3.1 shows that for finite difference with the largest stable timestep, the  $L_2$  error is only about 2.5%, which is acceptable for a long coarsening simulation.

The second source of error comes from the the dynamic time scales that occur during phase separation. High frequency oscillations are smoothed on a very short time scale, while phase separation then occurs on an intermediate timescale, and coarsening on a long timescale. Typically for coarsening in 3D, the radius of particles is expected to grow as  $t^{\frac{1}{3}}$ . A small timestep accurately captures decay of high frequencies as well as phase-separation, but renders the long time coarsening regime inaccessible. A large timestep allows simulations of coarsening, but does not provide the resolution to accurately simulate high frequencies and phase separation. Error from different timescales can be addressed with an adaptive timestep method that automatically adjusts the timestep according to the current dynamics in a simulation. Using a fixed timestep is inefficient.

The following two sections demonstrate how both sources of error can be reduced with the use of a second-order IMEX Runge-Kutta time integrator, an error estimator, and adaptive timestep controller. Holding total accumulated error constant, the second-order time integrator and timestep controller were each found to provide a magnitude improvement in running time compared to the first-order IMEX scheme.

### 3.5.1 2nd-order Runge-Kutta timestepping

Runge-Kutta methods are popular multi-step integrators for ordinary differential equations. For a review of Runge-Kutta techniques, the reader is referred to books by Hairer [8, 9]. Runge-Kutta methods take small intermediate steps between the

current time  $t$  and the next step  $t + \Delta t$ , and weights the intermediate steps to compute an accurate solution at the next timestep  $t + \Delta t$ . The methods are popular because they offer high accuracy, good stability, and are self-starting, only requiring knowledge of the field at its current timestep. Runge-Kutta also provides a natural way to estimate truncation error and, unlike other multistep methods, is well suited for variable timesteps.

Ascher et al. developed a set of Runge-Kutta methods for solving differential equations with an implicit-explicit splitting [10]. Such IMEX-RK schemes use a different Runge-Kutta tableau for the implicit and explicit parts, and the tableaus are constructed in such a way that higher order temporal accuracy is achieved. The Ascher schemes were analyzed by Kennedy and Carpenter [11] (see table 11, bottom of pg 163) who found that the Ascher (2,3,2) scheme<sup>1</sup> has very good numerical properties compared to many other multistep schemes. Kennedy and Carpenter also note marginal improvement in efficiency of higher-order methods at practical tolerances. Since the right-hand side of the diffusion equation is expensive to evaluate and very high accuracy is generally not necessary in phase-field modeling, a second-order accurate time integrator is likely a good choice.

Because the implicit-explicit splitting of the nonlinear diffusion equation (Eq. 3.18) produced both a stiff linear term and a stiff nonlinear term, it is important that the scheme be stiffly accurate. This criteria is necessary because it has been observed that the order of diagonally-implicit Runge-Kutta schemes can be reduced for stiff problems [8]. The stiffly accurate requirement rules out several of the other Ascher schemes, including the (2,3,2) scheme. The closely related Ascher (2,2,2) scheme (2 implicit stages, 2 explicit stages, 2<sup>nd</sup> order accurate) is stiffly accurate and was used

---

<sup>1</sup>In Ascher's notation, (2,3,2) denotes a Runge-Kutta scheme with 2 implicit stages and 3 explicit stages that is 2<sup>nd</sup> order accurate.



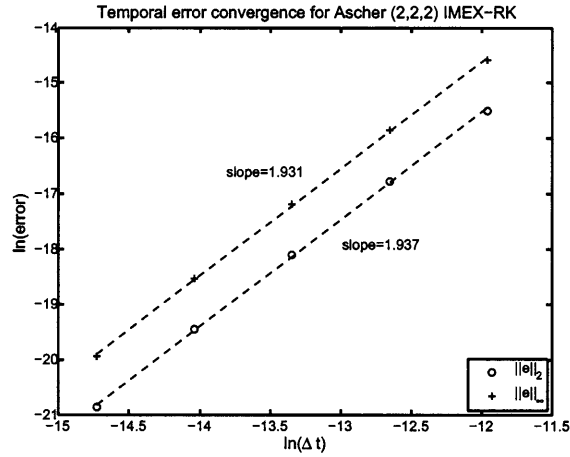


Figure 3-6: Temporal error convergence for the Ascher (2,2,2) IMEX-RK time integrator.

in this work. The Butcher tableau for the scheme is [10]:

$$\begin{array}{c|cc}
 & \text{Implicit} & \text{Explicit} \\
 0 & 0 & 0 \\
 \gamma & 0 & \gamma \\
 1 & 0 & 1 - \gamma \\
 \hline
 & 0 & 1 - \gamma \\
 \hline
 \end{array}
 \quad
 \begin{array}{c|ccc}
 & \text{Explicit} & & \\
 0 & 0 & & \\
 \gamma & \gamma & & \\
 1 & \delta & 1 - \delta & \\
 \hline
 & \delta & 1 - \delta & 0 \\
 \hline
 \end{array}
 \quad (3.20)$$

with  $\gamma = (2 - \sqrt{2})/2$  and  $\delta = 1 - 1/(2\gamma)$ .

It is important to verify that the chosen IMEX-RK scheme is second-order accurate when applied to the nonlinear diffusion equation because of the possibility of order reduction for stiff equations. The Gaussian initial condition (figure 3-3) and free energy function from section 3-1 were used to measure temporal convergence. This simulation was chosen instead of spinodal decomposition because it minimizes error resulting from the temporal dynamics of the simulation. Dynamic error will be properly be addressed with an adaptive timestepping approach. A grid spacing of  $1/128$  was used, and a reference solution was computed using the IMEX-RK time integrator with  $A = 0$  and  $\Delta t = 1 \times 10^{-7}$ . Timesteps much smaller than the max-

imum stable timestep ( $\Delta t = \{4, 8, 16, 32, 64\} \times 10^{-7}$ ) were used as well to minimize error. Figure 3-6 plots the natural log of both  $L_2$  and  $L_\infty$  error versus timestep. The slope of the fit lines are very close to 2, confirming that the method is second-order accurate in time.

### 3.5.2 Adaptive timestepping

In a recent paper [12], Cueto-Felgueroso and Peraire remark that timestep control for the Cahn-Hilliard equation is virtually absent from literature despite frequent application of the equation in models of phase transformations. They note that the equation is very stiff due to the biharmonic  $\nabla^4 c$  term, and also rich on the temporal scale. To address these concerns, Cueto-Felgueroso applied a time-adaptive implicit Runge-Kutta integrator to the Cahn-Hilliard equation using a finite volume method. Since a fully implicit solver is often expensive in practice, a time-adaptive implementation of an IMEX spectral solver is presented here.

Runge-Kutta with adaptive timestep control relies on the idea that truncation error can be computed by comparing a solution of order  $p$  to a solution of order  $p - 1$ . For example, the difference between a second-order accurate solution and a first-order accurate solution  $\|u_2 - u_1\|$  is proportional to  $\Delta t^2$ . In this work, the second-order solution is computed using the Ascher (2,2,2) scheme (Eq. 3.20), and the first-order solution is calculated using Eq. 3.19, the forward-backward Euler discretization, which is stiffly accurate. This discretization can also be described with a Runge-Kutta tableau:

$$\begin{array}{cc|cc}
 \text{Implicit} & & \text{Explicit} & \\
 0 & | & 0 & | \\
 1 & | & 1 & | \\
 \hline
 & | & & | \\
 & | & 0 & | \\
 & | & 1 & | \\
 & | & & |
 \end{array} \quad (3.21)$$

The algorithm for adaptive timestepping used in this work is described by Hairer

$e_0$	$\Delta t_{ave}$	total steps	$\ e\ _2$	$\ e\ _\infty$
$1 \times 10^{-6}$	$1.33 \times 10^{-4}$	74942	$1.47 \times 10^{-3}$	$6.36 \times 10^{-3}$
$1 \times 10^{-5}$	$5.03 \times 10^{-4}$	20594	$5.08 \times 10^{-3}$	$2.22 \times 10^{-2}$
$1 \times 10^{-4}$	$1.11 \times 10^{-3}$	9997	$2.25 \times 10^{-2}$	$9.50 \times 10^{-2}$
$1 \times 10^{-3}$	$1.39 \times 10^{-3}$	8416	$4.78 \times 10^{-1}$	$8.28 \times 10^{-1}$

Table 3.2: Performance of the adaptive timestepping method for different error tolerances ( $A = .25$ ).

[8], and the equation for picking the next timestep is:

$$\Delta t_{new} = .95 \Delta t_{old} \left( \frac{\|u_1 - u_2\|_2}{e_0} \right)^{\frac{1}{2}} \quad (3.22)$$

where  $e_0$  is a desired error tolerance for each step and error is measured in the  $L_2$  norm. The new  $\Delta t$  is chosen so as to keep the estimated error approximately equal to the error tolerance. If the estimated error is less than  $e_0$ , the iteration is accepted and the the timestep is increased for the next iteration. If the estimated error is larger than  $e_0$  however, the iteration is rejected and the timestep is reduced for the next iteration. .95 is a safety factor that decreases the number of rejected steps by slightly reducing the new timestep choice.

The trade-off between grid spacing and timestep is replaced with a trade-off between running and time and accuracy, and adaptive timestepping provides a method to pick an appropriate timestep to stay within error bounds. Being able to safely reject an iteration has other benefits as well. For example if  $c$  were to become negative as a result of overstepping the  $c = 0$  boundary, perhaps because of a large timestep, the diffusion equation would become ill-posed. The adaptive timestep algorithm would reject such an iteration and reduce the timestep.

Tables 3.2 and 3.3 present performance data for adaptive timestepping applied to the 1D coarsening problem (figure 3-5). Table 3.2 shows how different values of the error tolerance  $e_0$  affect the total error in the solution as well as the number of required iterations. Table 3.3 confirms that for values of  $A < .25$ , the diffusion

$A$	$\Delta t_{ave}$	total steps	$\ e\ _2$	$\ e\ _\infty$
.125	$2.82 \times 10^{-6}$	4008130	$2.05 \times 10^{-3}$	$6.27 \times 10^{-3}$
.25	$1.11 \times 10^{-3}$	9997	$2.25 \times 10^{-2}$	$9.50 \times 10^{-2}$
.5	$1.67 \times 10^{-3}$	6515	$3.92 \times 10^{-2}$	$1.66 \times 10^{-1}$
1	$1.76 \times 10^{-3}$	6058	$1.06 \times 10^{-1}$	$4.25 \times 10^{-1}$

Table 3.3: Performance of the adaptive timestepping method for different values of  $A$  ( $e_0 = 1 \times 10^{-4}$ ).

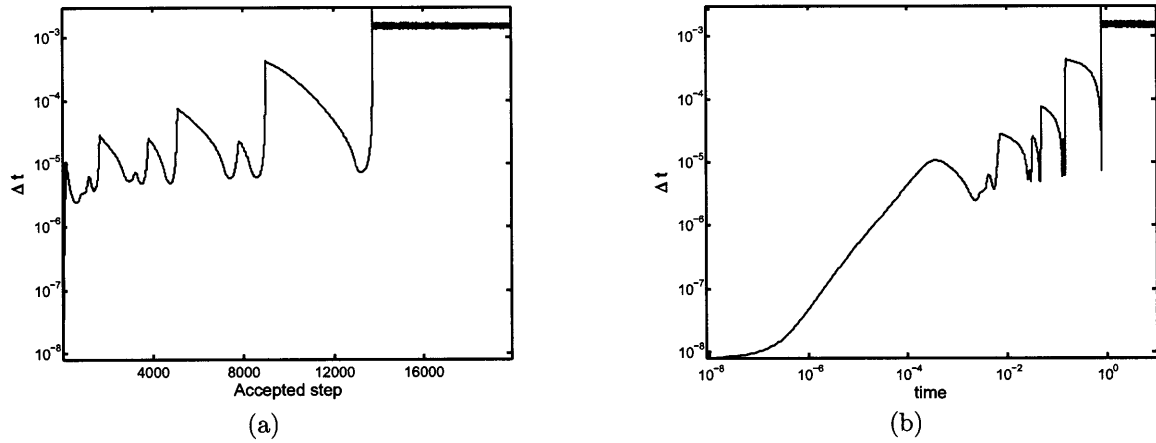


Figure 3-7: The timestep  $\Delta t$  chosen by the adaptive timestep algorithm for the phase separation simulation with  $e_0 = 1 \times 10^{-5}$ .

equation is unstable and a large number of iterations are necessary, even with time adaptivity. The table also confirms that large values of  $A$  increase the total error independent of the time integrator used.

Figure 3-7 shows the timestep chosen by the adaptive algorithm for the coarsening problem when an error tolerance of  $e_0 = 1 \times 10^{-5}$  was used. Timestep is plotted versus iteration number in figure 3-7a to convey how a large fraction of the computation effort is focused on accurately capturing spinodal decomposition with small timesteps at the beginning of the simulation. The complex dynamics of spinodal decomposition is reflected in the shape of the  $\Delta t$  curve. Part way through the simulation, the timestep stabilizes around  $\Delta t = 10^{-3}$ . The beginning of this stable region corresponds to the start of the coarsening regime in the simulation. Figure 3-7b shows  $\Delta t$  as a function

Method	CPU time (sec)	$\ e\ _2$	$\ e\ _\infty$
Explicit finite difference, $\Delta t = 2 \times 10^{-6}$	1051	$2.40 \times 10^{-2}$	$9.07 \times 10^{-2}$
RK1, $A = .25, \Delta t = 5 \times 10^{-6}$	286	$2.52 \times 10^{-2}$	$1.06 \times 10^{-1}$
RK2, $A = .25, \Delta t = 1 \times 10^{-4}$	28	$3.06 \times 10^{-2}$	$1.25 \times 10^{-1}$
Adaptive RK2, $A = .25, e_0 = 1 \times 10^{-4}$	3	$2.25 \times 10^{-2}$	$9.50 \times 10^{-2}$

Table 3.4: Running time of different integrators coded in MATLAB. The slow time measured for explicit finite difference iterations might be partially explained by inefficient implementation in MATLAB.

of simulation time on a log scale. This plot shows the fine timestep adjustments at the beginning of the simulation which are difficult to see in figure 3-7a. From start to finish, the timestep was varied over five orders of magnitude.

### 3.6 Benchmarks

Perhaps the most important consideration when developing a numerical method for engineering problems is the computational efficiency. Accuracy and stability are important considerations as well, but in the end, results must be obtainable in a reasonable amount of time. Running times for several different methods applied to the 1D coarsening problem are presented in table 3.4. The simulations were all performed in MATLAB. Total accumulated error was held roughly constant at about 2.5% in the  $L_2$  norm and about 10% in the  $L_\infty$  norm. The timestep of each method was adjusted to achieve these tolerances. Table 3.4 shows that the adaptive Runge-Kutta method is about three orders of magnitude more efficient than explicit finite difference, two orders of magnitude more efficient than first-order RK1 timestepping, and an order of magnitude more efficient than second-order RK2 timestepping. The adaptive RK2 algorithm is by far the most expensive per iteration, but wins out by taking its steps very efficiently. The order of magnitude difference between RK1 and RK2 reflects the fact that solving Eq. 3.19 with constant timesteps, and is common practice in phase-field modeling, is either inaccurate or inefficient depending on the

problem. The order of magnitude difference between RK2 and adaptive RK2 reflects the rich temporal time scales in phase separation problems.

### 3.7 Future Work

A discussion on future work related to numerical methods for phase-field modeling can be found in section 7.1.1 and appendix A.

## Notes

<sup>3</sup> Distributing the outer divergence operator in the Cahn-Hilliard equation and using centered differences produces a discretization that does not conserve when mobility is non-constant. A proof of the loss of conservation in a 1D periodic system follows. Begin by distributing the outer gradient and substitute centered finite differences for the gradients:

$$\begin{aligned}
\frac{\partial c}{\partial t} &= -\nabla \cdot J = \nabla \cdot \left( M \nabla \frac{\delta f}{\delta c} \right) \\
&= \nabla M \cdot \nabla \frac{\delta F}{\delta c} + M \nabla^2 \frac{\delta f}{\delta c} \\
\frac{\Delta c_i}{\Delta t} &= \frac{M_{i+1} - M_{i-1}}{2\Delta x} \cdot \frac{\delta_{i+1} - \delta_{i-1}}{2\Delta x} + M_i \cdot \frac{\delta_{i+1} - 2\delta_i + \delta_{i-1}}{\Delta x^2} \\
&= \frac{1}{4\Delta x^2} (M_{i+1}\delta_{i+1} - M_{i+1}\delta_{i-1} - M_{i-1}\delta_{i+1} + M_{i-1}\delta_{i-1} + 4M_i\delta_{i+1} + 4M_i\delta_{i-1} - 8M_i\delta_i)
\end{aligned} \tag{3.23}$$

The symbol  $\delta_i$  was used in place of  $\frac{\delta F}{\delta c_i}$  for simplicity. The following summations over the system hold because periodic boundary conditions are assumed:

$$\begin{aligned}
\sum_i M_{i+1}\delta_{i+1} &= \sum_i M_i\delta_i \\
\sum_i M_{i+1}\delta_{i-1} &= \sum_i M_i\delta_{i-2} \\
\sum_i M_{i-1}\delta_{i+1} &= \sum_i M_i\delta_{i+2} \\
\sum_i M_{i-1}\delta_{i-1} &= \sum_i M_i\delta_i
\end{aligned} \tag{3.24}$$

Using these relationships, Eq. 3.23 can be simplified:

$$\begin{aligned}
\sum_i \frac{\Delta c_i}{\Delta t} &= \frac{1}{4\Delta x^2} \sum_i (M_i \delta_i - M_i \delta_{i-2} - M_i \delta_{i+2} + M_i \delta_i + 4M_i \delta_{i+1} + 4M_i \delta_{i-1} - 8M_i \delta_i) \\
&= \frac{1}{4\Delta x^2} \sum_i M_i (-\delta_{i-2} + 4\delta_{i-1} + 6\delta_i + 4\delta_{i+1} - \delta_{i+2}) \\
&\neq 0
\end{aligned} \tag{3.25}$$

Concentration is not conserved because  $\sum_i \frac{\Delta c_i}{\Delta t} \neq 0$ . If the Laplacian operator is not distributed, the same approach can be used to show that mean concentration is conserved:

$$\begin{aligned}
\frac{\partial c}{\partial t} &= \nabla \cdot \left( M \nabla \frac{\delta f}{\delta c} \right) \\
\frac{\Delta c_i}{\Delta t} &= \nabla \cdot \left( M_i \frac{\delta_{i+1} - \delta_{i-1}}{2\Delta x} \right) \\
&= \nabla \cdot \left( \frac{1}{2\Delta x} (M_i \delta_{i+1} - M_i \delta_{i-1}) \right) \\
&= \frac{1}{2\Delta x} \left( \frac{M_{i+1} \delta_{i+2} - M_{i-1} \delta_i}{2\Delta x} - \frac{M_{i+1} \delta_i - M_{i-1} \delta_{i-2}}{2\Delta x} \right) \\
&= \frac{1}{4\Delta x^2} (M_{i+1} \delta_{i+2} - M_{i-1} \delta_i - M_{i+1} \delta_i + M_{i-1} \delta_{i+2})
\end{aligned} \tag{3.26}$$

$$\begin{aligned}
\sum_i \frac{\Delta c_i}{\Delta t} &= \frac{1}{4\Delta x^2} \left( \sum_i M_i \delta_{i+1} - \sum_i M_i \delta_{i+1} - \sum_i M_i \delta_{i-1} + \sum_i M_i \delta_{i-1} \right) \\
&= 0
\end{aligned} \tag{3.27}$$

<sup>4</sup> Starting with an equation of the form:

$$\nabla \cdot (x(c) \nabla y(c)) \tag{3.28}$$

Distribute the outer gradient operator to obtain:

$$\nabla \cdot (x \nabla y) = \nabla x \cdot \nabla y + x \nabla^2 y \tag{3.29}$$

Now expand  $\nabla^2(xy)$  and solve for  $\nabla x \cdot \nabla y$ :

$$\nabla^2(xy) = x \nabla^2 y + 2 \nabla x \cdot \nabla y + y \nabla^2 x \tag{3.30a}$$

$$\nabla x \cdot \nabla y = \frac{1}{2} (\nabla^2(xy) - x \nabla^2 y - y \nabla^2 x) \tag{3.30b}$$

Substitute Eq. 3.30b into Eq. 3.29 to obtain an expression with only Laplacian operators:

$$\nabla \cdot (x\nabla y) = \frac{1}{2} (\nabla^2(xy) + x\nabla^2 y - y\nabla^2 x) \quad (3.31)$$

## References

- [1] U. M. Ascher, S. J. Ruuth, and B. T. R. Wetton. Implicit explicit methods for time-dependent partial-differential equations. *Siam Journal on Numerical Analysis*, 32(3):797–823, 1995.
- [2] Lloyd N. Trefethen. Finite difference and spectral methods for ordinary and partial differential equations. Unpublished text, 1996, available at <http://www.comlab.ox.ac.uk/nick.trefethen/pdetext.html>.
- [3] Lloyd N. Trefethen. *Spectral methods in MATLAB*. Society for Industrial and Applied Mathematics, 2000.
- [4] David Gottlieb and Steven A. Orszag. *Numerical analysis of spectral methods : theory and applications*. Society for Industrial and Applied Mathematics, 1977.
- [5] Matteo Frigo and Steven G. Johnson. The design and implementation of FFTW3. *Proceedings of the IEEE*, 93(2):216–231, 2005. Special issue on “Program Generation, Optimization, and Platform Adaptation”.
- [6] L. Q. Chen and J. Shen. Applications of semi-implicit fourier-spectral method to phase field equations. *Computer Physics Communications*, 108(2-3):147–158, 1998. 22 ELSEVIER SCIENCE BV ZD584.
- [7] J. Z. Zhu, L. Q. Chen, J. Shen, and V. Tikare. Coarsening kinetics from a variable-mobility cahn-hilliard equation: Application of a semi-implicit fourier spectral method. *Physical Review E*, 60(4):3564–3572, 1999. 18 AMERICAN PHYSICAL SOC Part A 250XD.



- [8] E. Hairer, S.P. Norsett, and G. Wanner. *Solving Ordinary Differential Equations I: Nonstiff Problems*. Springer-Verlag, 1993.
- [9] E. Hairer, S.P. Norsett, and G. Wanner. *Solving Ordinary Differential Equations II: Stiff and Differential-Algebraic Problems*. Springer-Verlag, 1991.
- [10] U. M. Ascher, S. J. Ruuth, and R. J. Spiteri. Implicit-explicit runge-kutta methods for time-dependent partial differential equations. *Applied Numerical Mathematics*, 25(2-3):151–167, 1997. Workshop on Innovative Time Integrators OCT 30-NOV 01, 1996 CTR MATH & COMP SCI, AMSTERDAM, NETHERLANDS.
- [11] C. A. Kennedy and M. H. Carpenter. Additive runge-kutta schemes for convection-diffusion-reaction equations. *Applied Numerical Mathematics*, 44(1-2):139–181, 2003.
- [12] L. Cueto-Felgueroso and J. Peraire. A time-adaptive finite volume method for the cahn-hilliard and kuramoto-sivashinsky equations. *Journal of Computational Physics*, 227(24):9985–10017, 2008. Cueto-Felgueroso, Luis Peraire, Jaume.

THIS PAGE INTENTIONALLY LEFT BLANK

## Chapter 4

# Spherulitic growth in multiphase systems

The phase-field model developed in chapter 2 is used here to study the growth of a critical nucleus in a ternary eutectic system. Little is known about phase-separation in ternary systems [1], and this work represents a new direction in multiphase modeling, which has focused largely on two and three phase binary systems [2]. This chapter shows that under certain conditions nucleus growth in multiphase is kaleidoscopic, with complex symmetric patterns being formed through growth-front nucleation mechanism. The conditions governing the formation of these kaleidoscopic spherulites is studied and, much like snowflakes, it was found that small parameter changes were found to produce completely different patterns. Several features observed in the spherulites are related to experimental observations in simpler systems and new way of visualizing and interpreting microstructure is also introduced. The chapter begins with a description of the ternary eutectic free energy landscape used throughout the rest of this thesis.

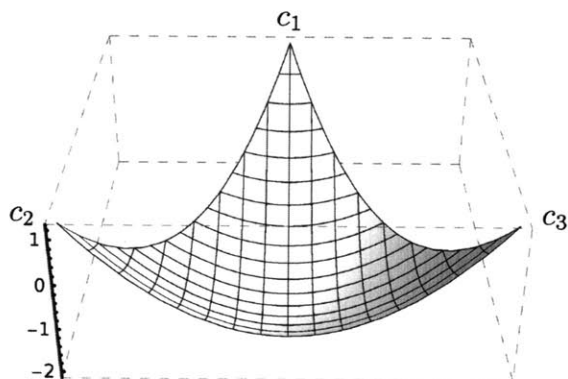


Figure 4-1: A ternary function of the form  $f(c_1, c_2) = -\psi(c_1c_2 + c_1c_3 + c_2c_3)$ .

## 4.1 The free energy landscape

Perhaps the most important input to a phase-field model are the free energy density functions. The free energy functions used here to study a four-phase ternary eutectic system are based on simple parabola-shaped functions of the form:

$$\begin{aligned}
 f(c_1, c_2) &= -\psi(c_1c_2 + c_1c_3 + c_2c_3) \\
 c_3 &= 1 - c_1 - c_2
 \end{aligned}
 \tag{4.1}$$

This function is plotted on a triangular grid in figure 4-1 with the three components as vertices of the triangle. The function is symmetric with respect to the three components and has a minimum at  $(c_1, c_2, c_3) = (\frac{1}{3}, \frac{1}{3}, \frac{1}{3})$ .  $\psi$  is a constant that adjusts the sharpness of the free energy curves and sets the energy scale.  $\psi = 10$  was used in this work.

A four-phase free energy landscape was created by translating the bowl function to create curves with minima at different compositions. The four free energy functions

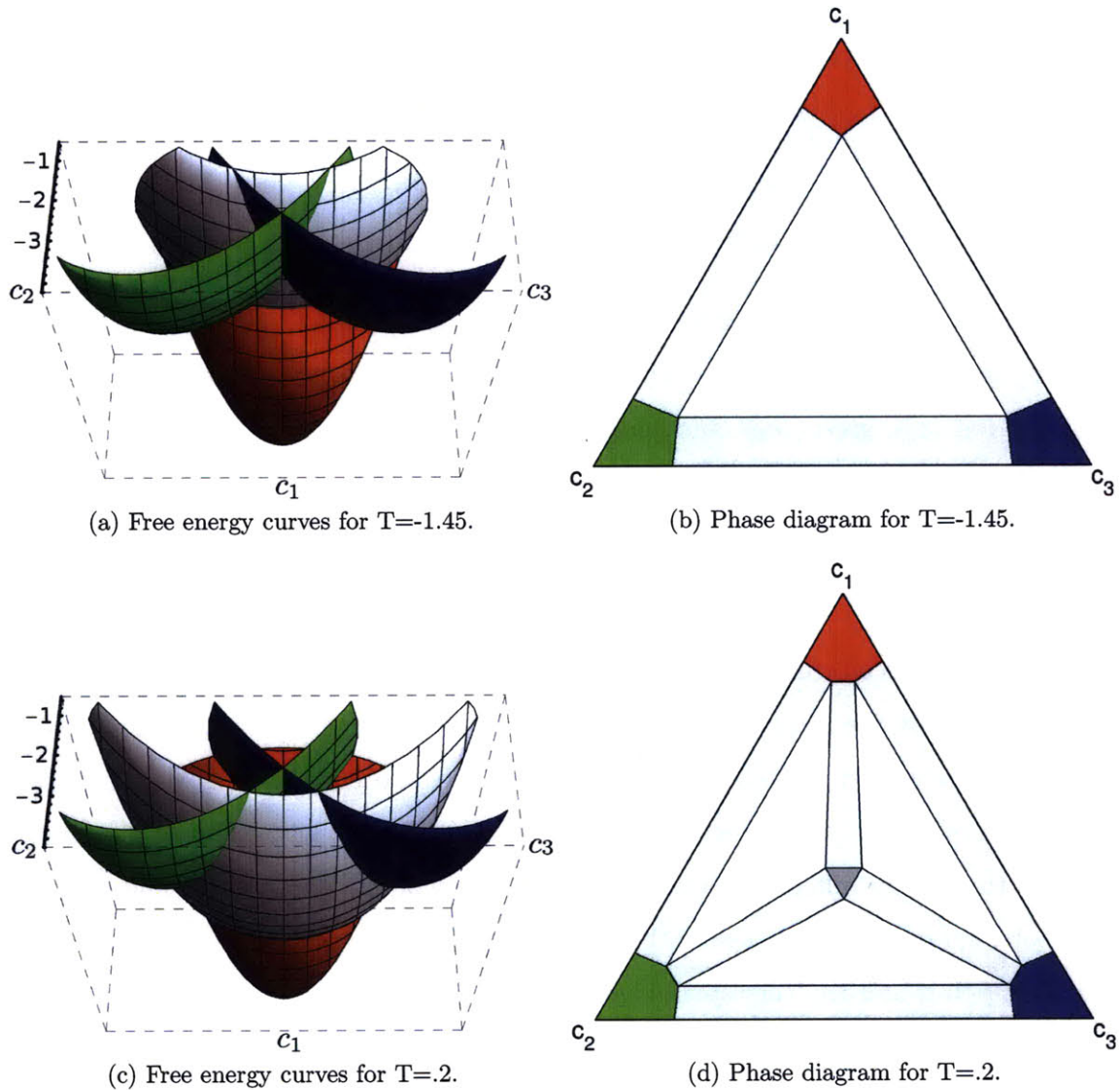


Figure 4-2: Ternary eutectic free energy curves, viewed from below, and the calculated phase diagrams. The diffusing components are colored red, green and blue, and there are three solid phases: a red-rich phase, a green-rich phase, and a blue-rich phase. A silver liquid phase appears in the center of the triangle, and the energy at its minimum relative to the solid curves is controlled by a dimensionless temperature.

are:

$$\begin{aligned}
 f_1(c_1, c_2) &= f(c_1 + 1/3 - .9, c_2 + 1/3 - .05) + \Delta G_{mix} \\
 f_2(c_1, c_2) &= f(c_1 + 1/3 - .05, c_2 + 1/3 - .9) + \Delta G_{mix} \\
 f_3(c_1, c_2) &= f(c_1 + 1/3 - .05, c_2 + 1/3 - .05) + \Delta G_{mix} \\
 f_4(c_1, c_2, T) &= f(c_1, c_2) - T + .5266 + \Delta G_{mix} \\
 \Delta G_{mix} &= c_1 \ln(c_1) + c_2 \ln(c_2) + (1 - c_1 - c_2) \ln(1 - c_1 - c_2)
 \end{aligned}
 \tag{4.2}$$

The curves are plotted in figure 4-2 at two different temperatures along with the corresponding phase diagrams. The three diffusing components in the system are colored red ( $c_1$ ), green ( $c_2$ ), and blue ( $c_3$ ), and the free energy curves are colored according to the concentration of their stable phase. The red curve is a red-rich phase, the green curve a green-rich phase, and the blue curve a blue-rich phase. The fourth phase is colored silver and its minimum is at the center of the ternary triangle.

The system is a ternary eutectic in the sense that the “liquid” phase first appears in the center of the phase diagram, and upon cooling, separates into three “solid” phases, each with a limited amount of solubility. The energy of the liquid curve minimum relative to the other curves is specified by  $T$ , a dimensionless temperature.  $T$  sets the energy difference between the minimum of the liquid curve and that of the solid curves. Fig. 4-2a shows the free energy curves for a temperature below the melting point, and the corresponding phase diagram in figure 4-2b shows no stable liquid at equilibrium. Figure 4-2c shows free energy curves for a temperature above the melting point. The minimum of the liquid curve is lower than the solid curves, and a single-phase liquid region now appears in the center of the phase diagram.

The liquid curve in 4-2a is higher in energy than the solid curves everywhere except for a small region of composition space close to the center of the ternary triangle. Over this small composition range liquid is the lowest energy phase, but liquid is metastable because the system can further lower its energy by phase-separating into the three

solid phases. The remainder of this chapter will investigate the process by which such a metastable eutectic liquid phase separates into three solid phases.

## 4.2 Eutectic solidification morphologies

A eutectic reaction occurs when a liquid is cooled and solidifies into two or more distinct solid phases. Eutectic solidification has been extensively studied for binary systems, and the resulting structures are generally limited and predictable [3, 4, 5, 6]. Ternary systems in contrast have more degrees of freedom and are much less predictable. This section will review some current theory related to binary and ternary eutectic solidification. A thorough review of the application of phase-field to solidification microstructures has been written by Boettinger [7].

The morphology of a binary eutectic is almost completely determined by the relative volume fractions of the equilibrium phases. Quenched binary eutectic liquid often forms a lamellar structure, but if the volume fraction of one of the equilibrium phases is small, rods or fibers of that phase grow embedded within a matrix of the high volume fraction phase. The rod morphology minimizes interfacial area and forms when the minor phase has a small volume fraction. A transition from rods to a lamellar structure occurs when the minor phase has a volume fraction greater than .32 [3]. The lamellar structure has the advantage that the relative thicknesses of the layers can change without introducing additional surface area.

Theory for interface stability in ternary solidification has been developed [8, 9], but morphological studies in ternary systems have often focused on systems where at least one phase has a small volume fraction at equilibrium. When one phase is not prevalent, it precipitates as droplets while the two remaining phases behave like a binary eutectic. Morphologies in ternary systems become interesting when the volume fraction of the equilibrium phases are approximately equal and phase triple junctions become a common feature in the microstructure. On this topic, Hecht [1]

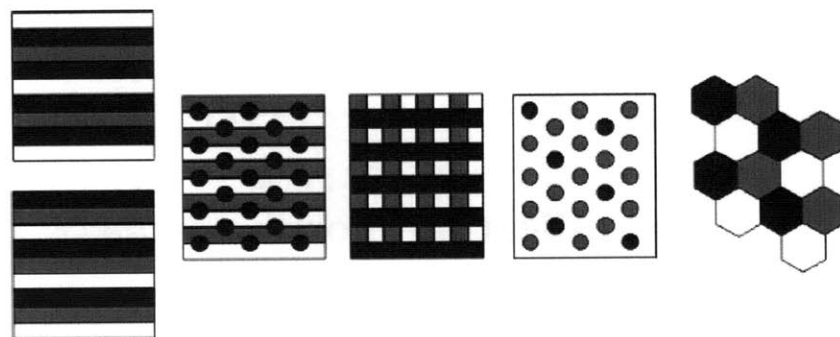


Figure 4-3: A sketch of possible morphologies for the solidification of a ternary eutectic liquid. The growth direction of the solidifying interface is out of the page. From left to right, the geometries are three lamellar planes, one fibrous and two lamellar, two fibrous and one lamellar, two fibrous in a matrix of the third, and three fibers. [10]

comments that “it emerges as challenging to question what coupled growth patterns will select, when forcing the alloy to grow in 2D confinement, i.e. when prohibiting the formation of quadruple points”. The next section will begin to investigate solidifying three-phase morphologies in 2D and reveal the importance of phase triple junctions on growth structures.

Ternary eutectics solidify into three-phase microstructures, and many more possible morphologies can be formed than in a binary system. With three interfacial energies, a three phase system will have phase triple junctions with contact angles dictated by surface energies. Ruggerio and Rutter [11] offer a verbal description of five morphologies expected to form during solidification of three phase eutectics, and a drawing of these morphologies is provided in figure 4-3. In addition to combinations of lamellar and fibrous structures, it is noteworthy that three-phase systems are able to form hexagonal arrays.

Himemiya and Umeda [12] analyzed three-phase growth morphologies including a regular lamellar structure, a rod and hexagon structure, and a brick-like structure resembling the middle picture in figure 4-3. Their analysis assumed only planar, flat interfaces, although solidifying eutectics often form of cellular structures. They admitted that there are likely many possible three-phase morphologies, and that



enumerating the morphologies and determining which morphology a specific system will form is a very difficult problem. It will be demonstrated in this chapter that the multiphase model is a very useful tool for investigating multiphase morphology problems because it obviates Himemiya's assumption of planar growth.

### 4.3 Kaleidoscopic spherulites

Liquids which are rapidly solidified under nonequilibrium conditions are often observed to form spherulites, which can be broadly described as microstructure that grows from a single nucleus and maintains a roughly spherical shape (circular in 2D). Spherulites are observed in pure materials, metallic alloys, ceramics, glasses, polymers, minerals, volcanic rocks, and even biological molecules [13, 14]. Despite their prevalence in everyday materials, there is no concrete theory to describe the formation and growth of these structures.

Experimental studies of spherulites has lead to classification into two categories. The first category grow spherically from the nucleation site. This type is similar to the lamellar structure which forms in a solidifying eutectic. The second category begin as rods which grow in opposite directions. The rods branch as they grow, eventually becoming spherical at longer times, but leaving two uncrystallized eyes near the center of the spherulite. This type of spherulite is not considered in this work.

There have been just a few phase-field studies of spherulite formation and growth [15, 16], and they have demonstrated that a relatively simple phase-field model could replicate many of the intricate spherulite morphologies that arise in microstructure. This previous work specifically focused on the effects of crystalline and interfacial anisotropy in binary systems and has not addressed the morphologies that are possible in multiphase systems.

An interesting morphological class of spherulites can be formed by systems that

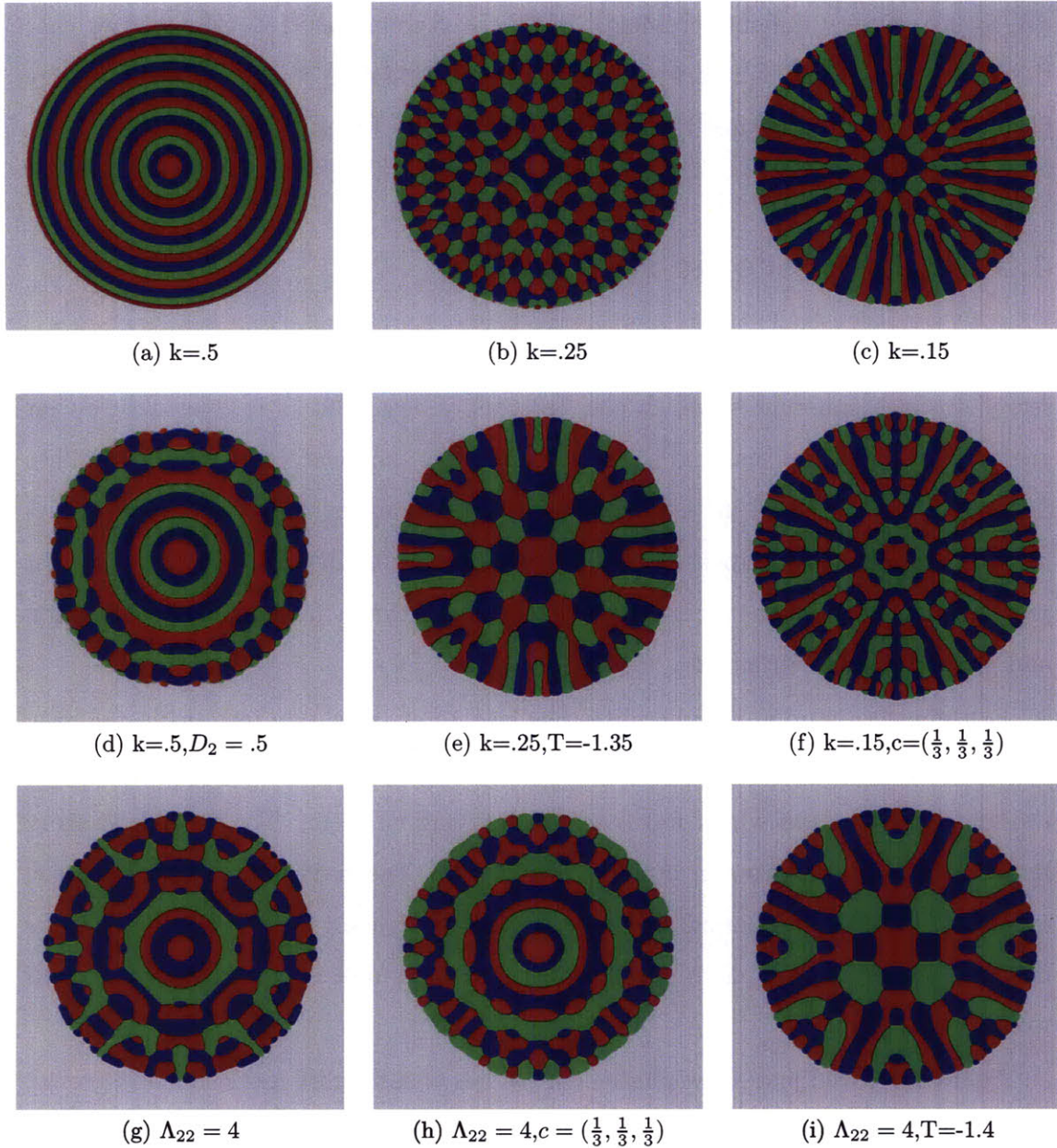


Figure 4-4: Three-phase spherulite morphologies under a variety of different conditions. Unless otherwise specified  $k = .25$ ,  $T = -1.45$ , and  $c = (.35, .31, .34)$ . (a)-(c) show the effect of decreasing interfacial energy. The middle row shows how subtle parameter changes lead to dramatic morphological changes. (f)-(g) shows the effect of changing the contact angle of the green phase with the other two phases so that green takes up more than 120 degrees at a phase triple junction.

phase-separate into more than two phases. Several examples of the growth of a critical solid nucleus from a metastable ternary eutectic liquid confined to a thin film are presented in figure 4-4. These structures will be referred to as kaleidoscopic spherulites. The spherulites were grown under different conditions, and it was found that phase barrier height, interfacial energy, interfacial velocity, contact angles of the different phases, and the mean composition of the system all play a role in the development of kaleidoscopic structures. In the figure,  $k$  is the value used for all gradient energy coefficients (both composition and phase), and the gradient energy matrices  $K$  and  $\Lambda$  are assumed to be diagonal.

The first row of structures in figure 4-4 show three different growth modes that were found to occur for different interfacial energies. The formation of ring spherulites in (a) corresponds to large interfacial energy, while an intermediate interfacial energy produces hexagons in (b), and a small interfacial energy and hence slow interfacial velocity results in a radiating lamellar structure in (c). Large interfacial energy tends to promote fast interface velocity, but it is unclear whether interfacial energy, growth velocity, or some combination of the two is responsible for the morphology changes. The ring morphology in (a) may be related to the phenomenon of halo formation observed in off-eutectic solidification [17]. Radiating lamellar structures qualitatively similar to (c) have been previously reported in binary eutectic phase-field simulations [18].

The second row of figure 4-4 shows how small parameter changes from the conditions in the first row result in drastic morphology changes. In (d), the diffusivity of  $c_2$  was reduced, in (e) the temperature was increased, and in (f) the composition of the liquid was changed. The structures in the second row show coexistence of the different growth modes from the top row. In (d) rings grow initially but break up as the radius increases, in (e) the initial growth is hexagonal but then transitions to radial lamellar growth, and (f) exhibits characteristics of all three modes.

The final row of figure 4-4 shows what happens when the green-red and green-

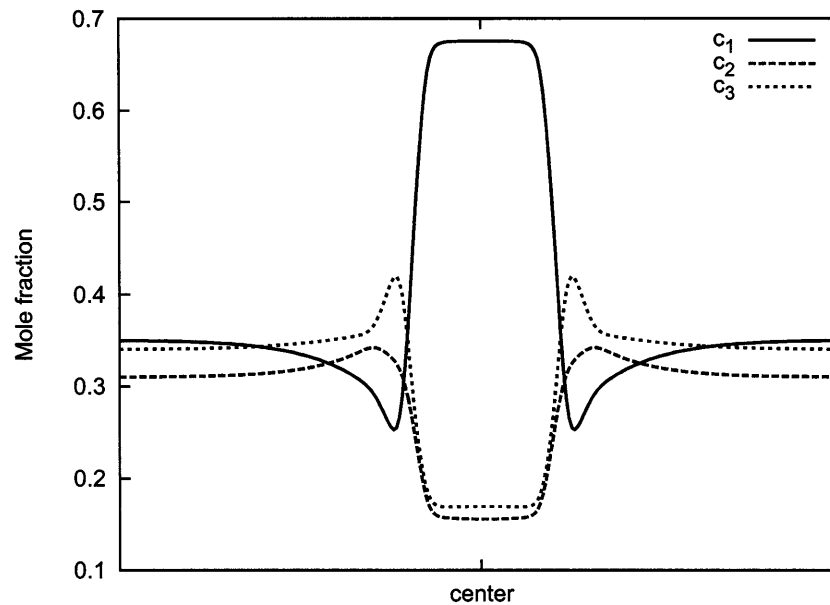


Figure 4-5: Accumulation and depletion of solute outside a growing nucleus in a ternary system governed by diffusion-limited growth.

blue surface energies are larger than the red-blue surface energy. Force balance at triple junctions requires that the angle taken by green becomes larger than 120. The formation of hexagonal patterns is disrupted and results in noticeably different morphologies.

### 4.3.1 Growth mechanism

The spherulites were observed to grow by a process of secondary or growth front nucleation, which has frequently been reported to play a role in the growth of spherulites [13, 19, 20, 16]. Drolet et al. studied a similar growth mechanism in binary eutectics with phase-field [18]. After nucleation of the primary nucleus at the center of the spherulite, the growing interface acts as a high-energy site that aids in the nucleation of new phases. The nucleation of new phases on the solidification front can be seen in several of the spherulites in figure 4-4. Phase triple junctions which form at the growing interface are particularly favorable high energy sites for secondary nucleation.

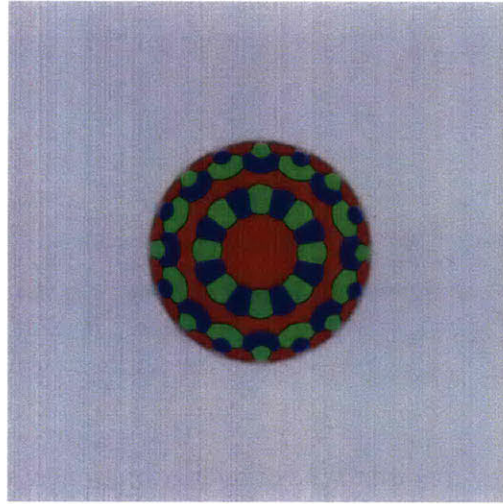


Figure 4-6: A spherulite that grew initially with 8-fold symmetry due to geometrical restrictions imposed by the natural length scales of the microstructure.  $k = .5$ ,  $W = 0$ ,  $c = (.36, .32, .32)$ .

The growth of the spherulites is also controlled by diffusion of solute in front of the solidifying interface. Figure 4-5 shows solute building up in front of a growing red nucleus. As the red-rich nucleus grows, red is depleted from the nearby environment and blue and green accumulate outside the nucleus. The red phase can only grow as fast as red can diffuse to the interface, and growth is therefore limited by diffusion. The build up of solute outside the interface affects the growth of the spherulite, and the high concentrations of blue and green just outside the interface reduce the nucleation barrier, resulting in the nucleation of red and green phases at the growing interface.

### 4.3.2 Origin of symmetry

It is tempting at first to believe that the four-fold symmetry of the spherulites is a numerical effect arising from the use of a square grid, periodic boundary conditions, and a four-fold symmetric initial nucleus. These tend to promote four-fold symmetry, there are other forces at play as well. The free energy functions and gradient energy

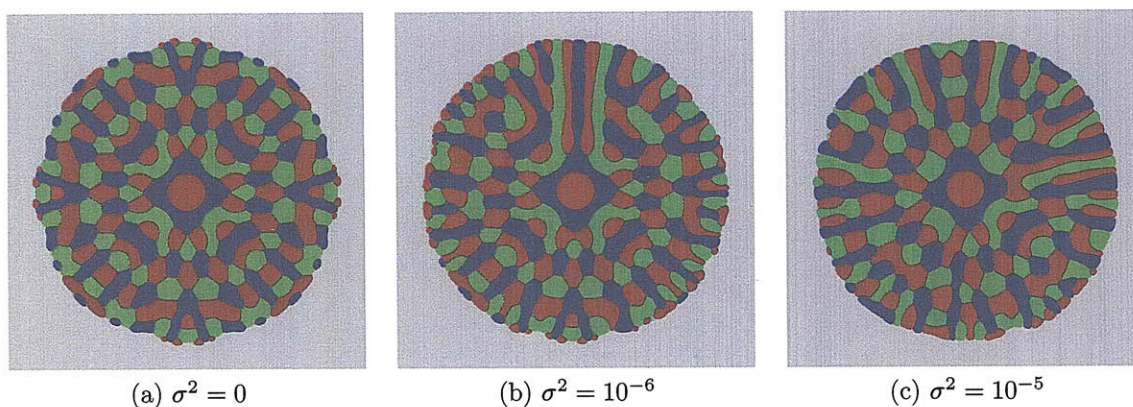


Figure 4-7: Adding Langevin noise to the diffusing components disrupts the symmetry in a growing kaleidoscopic spherulite.  $\Lambda_{22} = 2$  and  $\Lambda_{33} = 2$  for these spherulites.

coefficients define characteristic length scales for the microstructure, and the mean composition of the system sets the volume fraction of equilibrium phases. These geometric restrictions combined with the radial growth of the spherulites can lead to other symmetries. An example is shown in figure 4-6, where the initial growth of a spherulite exhibited eight-fold symmetry. The phase barrier height  $W$  was set to zero, and  $c_2$  and  $c_3$  in the homogeneous liquid were set equal so that the blue and green phases are energetically equivalent. The result is that spinodal decomposition is triggered but only in the vicinity of the moving interface. As the spherulite grows larger, the 8-fold symmetry disappears, presumably an effect of the periodic boundaries.

### 4.3.3 Morphological stability

The spherulites in figure 4-4 were simulated without the addition of any noise so that the different growth modes might be highlighted. In experimental systems, thermal fluctuations will affect the stability of moving interfaces. Noise was added to the composition variables as described in section 5.1.1 to investigate morphological stability. A finding that emerged from running many simulations over the large parameter space was that slow diffusivity in the solid relative to the liquid functions

as a stabilizing force in the presence of noise.

Figure 4-7 shows the effect of different degrees of thermally induced noise on the growth of a kaleidoscopic spherulite with equal solid and liquid diffusivities. Although the noise disrupts symmetric growth, it does not dramatically change the characteristics of the spherulites. It is interesting that the introduction of noise is able to initiate radial lamellar growth in isolated regions of the spherulites in figures (b) and (c).

Composition plays an important role in the stability of interfaces, and morphologies formed from liquid with a composition very close to  $c = (\frac{1}{3}, \frac{1}{3}, \frac{1}{3})$  are inherently unstable and prone to breaking symmetry. The instability can be rationalized because  $c = (\frac{1}{3}, \frac{1}{3}, \frac{1}{3})$  is equidistant from each of the three solid phases and all energy barriers are equal. Small composition fluctuations are easily able to nudge the local composition toward one of the phases at random and cause that phase to precipitate.

## 4.4 Experimental evidence

No direct experimental observation of kaleidoscopic growth could be found, possibly because there has been little experimental or theoretical work studying morphology in multiphase systems. Kaleidoscopic growth is expected when the volume fraction of the phases at equilibrium are approximately equal, but most previous multiphase work has focused on the case where at least one of the phases has a small volume fraction at equilibrium. Although the multiphase growth instability has not yet been experimentally observed, many features found in the spherulites have been observed in experiments of diffusion controlled growth. It is possible to rationalize that kaleidoscopic growth could occur in multiphase systems by studying spherulite grown in simpler systems.

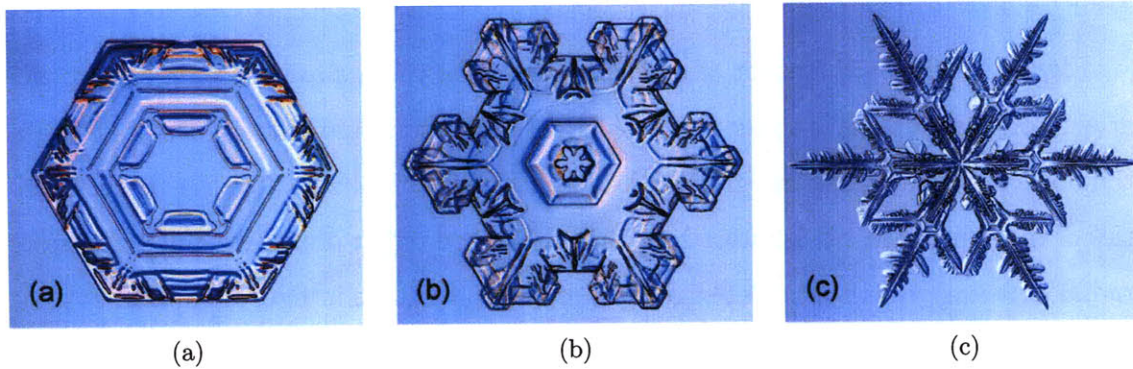


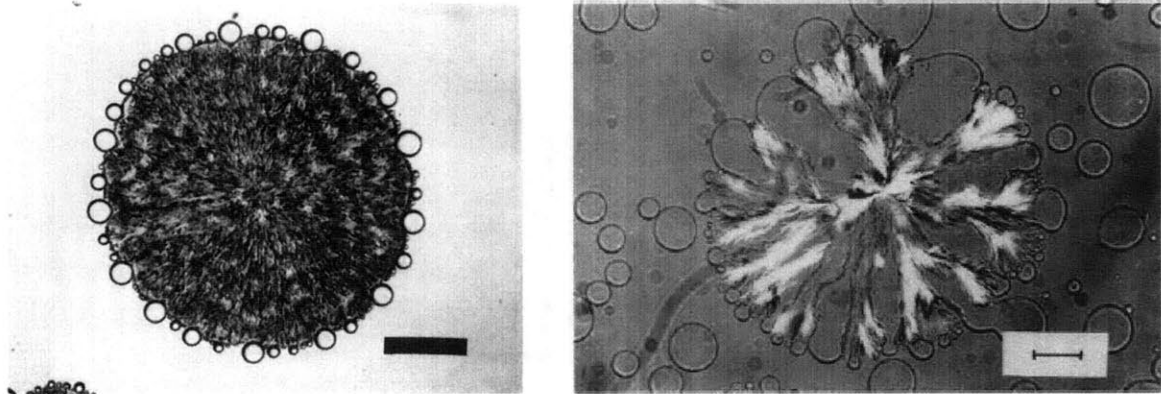
Figure 4-8: Photographs of highly symmetric snowflakes that are on the order of millimeters in size. [21]

#### 4.4.1 Similarity to snowflakes

One concern is whether kaleidoscopic structures could actually grow to a reasonable size in an experimental system without breaking symmetry. Snowflakes are good example of a well known diffusion-limited growth structure that, under the right conditions, can grow to very large size while maintaining symmetry [21]. Photographs of large symmetric snowflakes are shown in figure 4-8. Snowflakes are thought be symmetric in part because they grow quickly and in a relatively uniform environment. The environment fluctuates, but the fluctuations are more or less constant over the small domain of the growing snowflake.

The dynamics of snowflake growth is controlled by particle diffusion which brings water molecules to the surface of the ice crystal, and heat diffusion which removes latent heat from the solidifying interface. Thus snowflakes are an example of solidification in a two-phase, binary system. The phases are water vapor and ice, and the independent component is the saturation of water. The growth of a snowflake is very sensitive to temperature and moisture content of the air, resulting in complex displays of symmetry and the old adage that no two snowflakes are alike. Like snowflakes, the morphology of the kaleidoscopic spherulites also strongly depends on input parameters, as previously illustrated in the previous section.





(a) Phase separation at the growth front of a PCL spherulite in a PCL/PS (70/30) wt% system at 50C. The bar corresponds to 100  $\mu\text{m}$ . [19]

(b) A PCL spherulite in a PCL/PS (40/60) wt% system at 46C after 27h. Tar corresponds to 50  $\mu\text{m}$ . [22]

Figure 4-9: A solidifying interface can trigger spinodal decomposition in polymer systems.

#### 4.4.2 Growth front nucleation in polymers

Tanaka and Nishi published two influential papers demonstrating that crystallization of a spherulite from a polymer blend could trigger phase separation at the growing interface [19, 20]. Follow-up studies examined the process in greater detail [22, 23]. All found that in a solidifying mixture of poly( $\epsilon$ -caprolactone) (PCL) and polystyrene (PS), the PS is rejected from the crystallizing spherulite and piles up at the growth front, triggering phase separation and the formation of PS droplets on the growing spherulite. The formation of these structures is a result of a kinetically controlled competition between the crystallization process and the phase separation process. Pictures of two crystallizing spherulites are shown in figure 4-9. (a) shows formation of beads of amorphous polymer at the interface, and (b) shows an intermixing of crystallized and amorphous polymer that resembles radial lamellar growth found in kaleidoscopic spherulites.

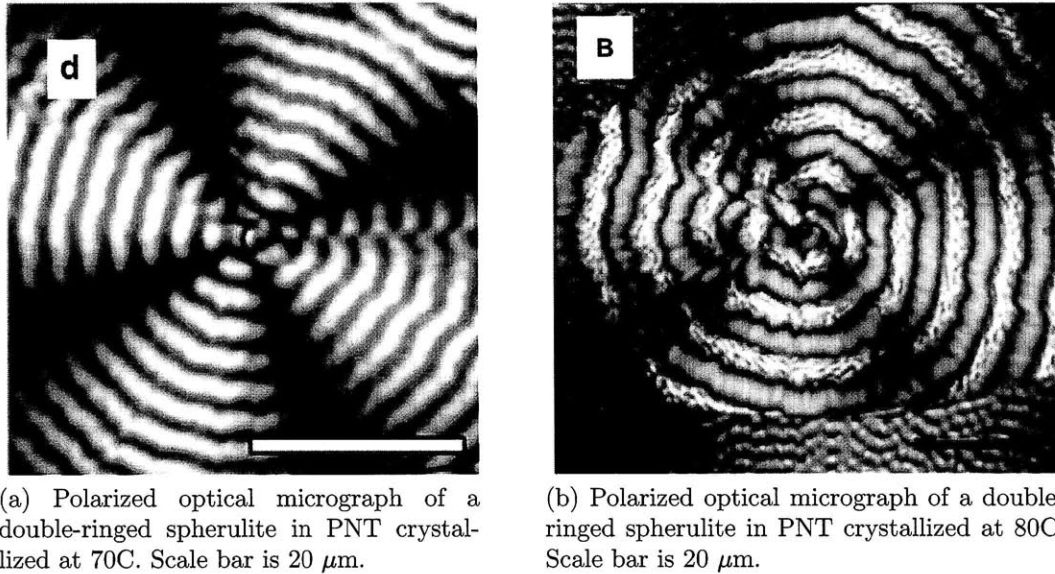


Figure 4-10: Growth of single and double ringed polymer spherulites is common in thin films. [24]

### 4.4.3 Ring structures

Ring-banded spherulites have been frequently observed in a variety of thin film polymer systems [25, 26, 24], and recently as compositional banding in thin film silicon-gold systems [27]. Examples of ringed spherulites are shown in figure 4-10. These ringed spherulites show remarkable resemblance to the kaleidoscopic spherulite in figure 4-4a, although the mechanisms of ring formation are not identical. The kaleidoscopic rings form from a cascade of nucleation events in a multiphase system, but rings in polymer spherulites are thought to be related to the structure of crystallizing polymers, forming due to the twisting of polymer lamellae. Diffusion-limited growth kinetics is thought to play an important role however, and the formation of ring spherulites in binary polymer blends has been simulated with phase-field methods [28].

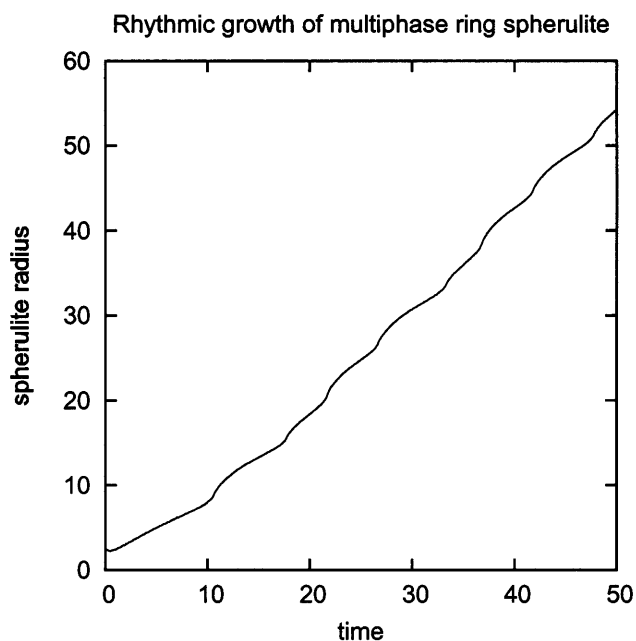
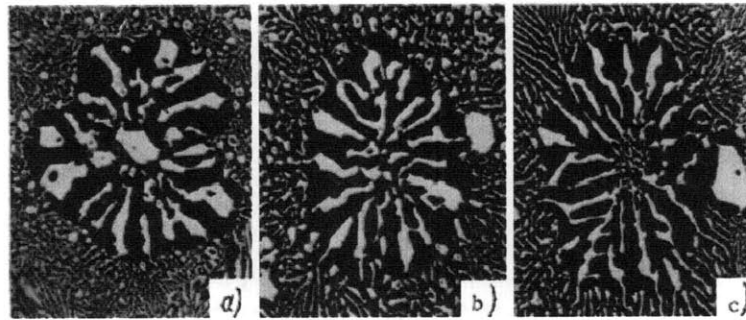


Figure 4-11: Measurement of the radius of the growing multiphase ring spherulite shows nonlinear growth. Each blip corresponds to the nucleation of a ring.

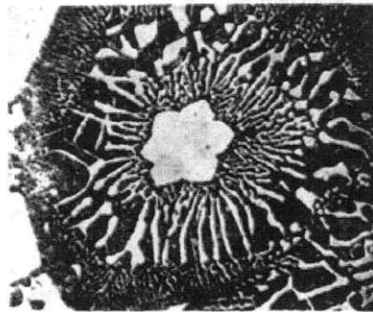
#### 4.4.4 Rhythmic ring growth

Experimental and theoretical studies have shown that, in contrast to theory, ring-banded spherulites do not grow at a constant rate [29, 30, 31, 32]. Instead, there is a period of fast growth as a new ring forms followed by a period of slow growth. Although some explanations are tailored to specific polymer systems, the leading explanation for rhythmic growth is that rejection of solute (amorphous polymer) from the crystallizing spherulite slows growth. It takes time for rejected solute to diffuse away from the interface, and growth is disrupted. Such an explanation applies to the kaleidoscopic rings, since each ring forms by rejection of the other two components.

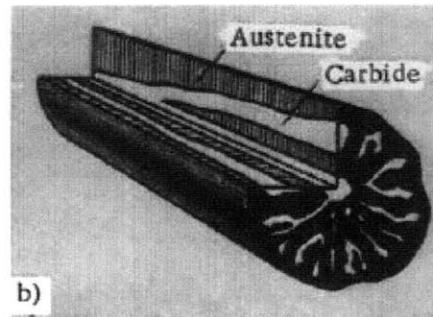
Measurement of the radius a growing kaleidoscopic ring spherulite shows that growth is rhythmic. The radius of a simulated ringed spherulite is plotted in figure 4-11 with clear evidence of nonlinear growth. Each blip in the plot corresponds to the nucleation of a ring, and the shape of the nonlinear deviations show good qualitative agreement with plots in [29, 30, 31, 32]. Figure 4-11 is further evidence that



(a) Sections of eutectic colonies in Fe-C-Cr alloys (x600) [33].



(b) Molybdenum cast iron with 25.13% Mo and 2.96% C, 400x. [34]



(c) Diagram of the austenite-chromium carbide eutectic [33].

Figure 4-12: Micrographs of eutectic colonies in ternary iron alloys.

solute rejection is a mechanism that can lead to rhythmic spherulite growth, and also a validation that the simulated kaleidoscopic spherulites are displaying appropriate growth dynamics.

## 4.5 Evidence in metallic systems

A final concern is whether kaleidoscopic spherulites might be a very specific morphology that only form in thin-film polymer systems under highly controlled laboratory conditions. Figure 4-12 shows quasi-2D structures that formed in cast iron alloys [33, 34]. The image shows a cut through a eutectic colony, which is a cylindrical structure with a growth direction out of the page. A fiber initially grew to form the center of the colony, and triggered the growth of a two-phase eutectic lamellar

structure which grew radially outward from the fiber, roughly maintaining a circular cross-section. Over short distances along its longitudinal axis, the fiber is essentially a 2D system. The growth patterns are similar in appearance to the radial growth simulated in figure 4-4c.

## 4.6 Visualizing diffuse interfaces

A challenge with diffuse interface modeling is interpreting results. Phase-field simulations contain a lot of important information, but it is difficult to extract because the output of the simulations are pictures of microstructure. 1D plots of concentration profiles at interfaces become difficult to comprehend for large microstructure and are not particularly effective for 2D or 3D microstructures. However, understanding how the composition profile at interfaces changes as microstructure develops is crucial.

To address this difficulty, a composition map was developed as a useful ternary visualization method, drawing on a technique originally used by Eyre [35]. Compositions in a microstructure are plotted on a ternary triangle to visually reveal information about all compositions in a microstructure at once. The composition map gives insight into which compositions are present in the microstructure, and the motion of the points when viewed as a movie reveals the path the system takes toward equilibrium.

The composition map is a triangle is drawn to correspond to the phase diagram, with the red diffusing component ( $c_1$ ) at the top vertex, green ( $c_2$ ) at the lower left, and blue ( $c_3$ ) at the lower right. For every composition in the microstructure, a corresponding point is drawn on the composition map, and the color of the point chosen to match the color of the composition in the microstructure. Compositions that are in the liquid phase are colored silver in the composition map for clarity<sup>1</sup>.

The composition map in figure 4-13 provides additional insight into the growth

---

<sup>1</sup>The liquid occurs at a composition near the center of the triangle, where an equal mix of red green and blue produces a dark brown which is difficult to distinguish visually.

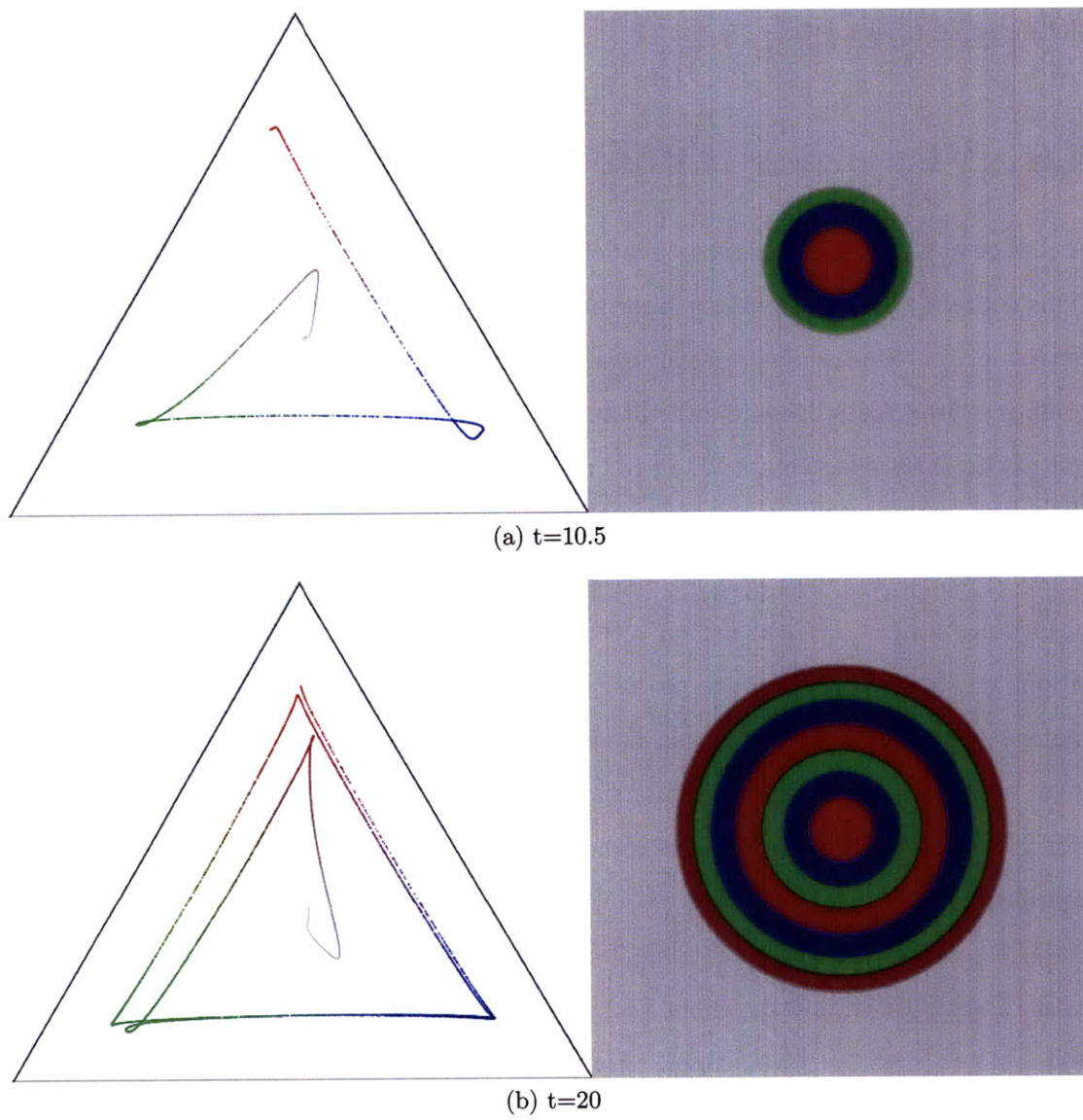


Figure 4-13: Illustration of a growing multiphase ringed spherulite with a composition map.

of multiphase ring spherulites. As rings nucleate, wispy lines of composition radiate from the center of the composition map toward the vertices of the triangle one at a time. Each point on the line corresponds to a composition within a diffuse interface somewhere in the microstructure. The lines eventually settle into an equilibrium profile, which can clearly be seen in the figure.

The appearance of loops in the line as rings nucleate is an unexpected finding that highlights the ability of the composition map to illuminate behavior that would be difficult to detect from images of microstructure alone. The loops result from a concentration gradient that is initially present in the outermost ring as it nucleates, and the corners of the loop correspond to the inner and outer surfaces of the ring. The disappearance of the concentration gradient at later times corresponds to shrinkage of the loops. Since the rings form by expelling solute which must then diffuse away from the spherulite, it is not surprising that the rings initially have a concentration gradient, although it is not visible in the microstructure images.

## References

- [1] U. Hecht, L. Granasy, T. Pusztai, B. Bottger, M. Apel, V. Witusiewicz, L. Ratke, J. De Wilde, L. Froyen, D. Camel, B. Drevet, G. Faivre, S. G. Fries, B. Legendre, and S. Rex. Multiphase solidification in multicomponent alloys. *Materials Science & Engineering R-Reports*, 46(1-2):1–49, 2004.
- [2] I. Singer-Loginova and H. M. Singer. The phase field technique for modeling multiphase materials. *Reports on Progress in Physics*, 71(10):32, 2008. Singer-Loginova, I. Singer, H. M. Swiss Federal Institute of Technology ETH, Zurich, Switzerland 374 IOP PUBLISHING LTD 362GS.
- [3] J. D. Hunt and K. A. Jackson. Binary eutectic solidification. *Transactions of the Metallurgical Society of Aime*, 236(6):843–&, 1966.

- [4] K. A. Jackson and J. D. Hunt. Lamellar and rod eutectic growth. *Transactions of the Metallurgical Society of Aime*, 236(8):1129–&, 1966.
- [5] V. S. Stubican and R. C. Bradt. Eutectic solidification in ceramic systems. *Annual Review of Materials Science*, 11:267–297, 1981.
- [6] D.A. Porter and K.E. Easterling. *Phase Transformations in Metals and Alloys*. Stanley Thornes (Publishers) Ltd, 2000.
- [7] W. J. Boettinger, S. R. Coriell, A. L. Greer, A. Karma, W. Kurz, M. Rappaz, and R. Trivedi. Solidification microstructures: Recent developments, future directions. *Acta Materialia*, 48(1):43–70, 2000.
- [8] M. D. Rinaldi, R. M. Sharp, and M. C. Flemings. Growth of ternary composites from melt .1. *Metallurgical Transactions*, 3(12):3133–3138, 1972.
- [9] M. D. Rinaldi, R. M. Sharp, and M. C. Flemings. Growth of ternary composites from melt .2. *Metallurgical Transactions*, 3(12):3139–3148, 1972.
- [10] D. Lewis, S. Allen, M. Notis, and A. Scotch. Determination of the eutectic structure in the ag-cu-sn system. *Journal of Electronic Materials*, 31(2):161–167, 2002.
- [11] M. A. Ruggiero and J. W. Rutter. Origin of microstructure in the 332 k eutectic of the bi-in-sn system. *Materials Science and Technology*, 13(1):5–11, 1997.
- [12] T. Himemiya and T. Umeda. Three-phase planar eutectic growth models for a ternary eutectic system. *Materials Transactions Jim*, 40(7):665–674, 1999.
- [13] H. D. Keith and F. J. Padden. A phenomenological theory of spherulitic crystallization. *Journal of Applied Physics*, 34(8):2409–&, 1963.
- [14] J. H. Magill. Review spherulites: A personal perspective. *Journal of Materials Science*, 36(13):3143–3164, 2001.



- [15] L. Granasy, T. Pusztai, and J. A. Warren. Modelling polycrystalline solidification using phase field theory. *Journal of Physics-Condensed Matter*, 16(41):R1205–R1235, 2004.
- [16] L. Granasy, T. Pusztai, G. Tegze, J. A. Warren, and J. F. Douglas. Growth and form of spherulites. *Physical Review E*, 72(1), 2005. Part 1.
- [17] M.F.X Gigliotti, G. A. Colligan, and G. L. F. Powell. Halo formation in eutectic alloy systems. *Metallurgical Transactions*, 1(4):891–&, 1970.
- [18] F. Drolet, K. R. Elder, M. Grant, and J. M. Kosterlitz. Phase-field modeling of eutectic growth. *Physical Review E*, 61(6):6705–6720, 2000. Part B.
- [19] H. Tanaka and T. Nishi. New types of phase-separation behavior during the crystallization process in polymer blends with phase-diagram. *Physical Review Letters*, 55(10):1102–1105, 1985.
- [20] H. Tanaka and T. Nishi. Local phase-separation at the growth front of a polymer spherulite during crystallization and nonlinear spherulitic growth in a polymer mixture with a phase-diagram. *Physical Review A*, 39(2):783–794, 1989.
- [21] K. G. Libbrecht. The physics of snow crystals. *Reports on Progress in Physics*, 68(4):855–895, 2005.
- [22] Y. Li, M. Stein, and B. J. Jungnickel. Competition between crystallization and phase-separation in polymer blends .1. diffusion controlled supermolecular structures and phase morphologies in poly(epsilon-caprolactone)/polystyrene blends. *Colloid and Polymer Science*, 269(8):772–780, 1991.
- [23] H. M. Shabana, R. H. Olley, D. C. Bassett, and B. J. Jungnickel. Phase separation induced by crystallization in blends of polycaprolactone and polystyrene: an investigation by etching and electron microscopy. *Polymer*, 41(14):5513–5523, 2000.

- [24] E.M. Woo and Yu-Fan Chen. Single- and double-ring spherulites in poly(nonamethylene terephthalate). *Polymer*, 50(19):4706 – 4717, 2009.
- [25] G. Kim, C. C. Han, M. Libera, and C. L. Jackson. Crystallization within melt ordered semicrystalline block copolymers: Exploring the coexistence of microphase-separated and spherulitic morphologies. *Macromolecules*, 34(21):7336–7342, 2001.
- [26] C. C. Su and J. H. Lin. Ringed spherulites in ternary polymer blends of poly(beta-caprolactone), poly(styrene-co-acrylonitrile), and polymethacrylate. *Colloid and Polymer Science*, 283(2):182–193, 2004.
- [27] D. K. Venkatachalam, N. H. Fletcher, D. K. Sood, and R. G. Elliman. Self-assembled nanoparticle spirals from two-dimensional compositional banding in thin films. *Applied Physics Letters*, 94(21), 2009.
- [28] H. J. Xu, H. W. Chiu, Y. Okabe, and T. Kyu. Breakup of spiral and concentric ringed spherulites in polymer crystallization. *Physical Review E*, 74(1), 2006. Xu, Haijun Chiu, Hao-Wen Okabe, Yoshifumi Kyu, Their Part 1.
- [29] Z. G. Wang, L. J. An, B. Z. Jiang, and X. H. Wangh. Periodic radial growth in ring-banded spherulites of poly(epsilon-caprolactone)/poly(styrene-co-acrylonitrile) blends. *Macromolecular Rapid Communications*, 19(2):131–133, 1998.
- [30] T. Kyu, H. W. Chiu, A. J. Guenther, Y. Okabe, H. Saito, and T. Inoue. Rhythmic growth of target and spiral spherulites of crystalline polymer blends. *Physical Review Letters*, 83(14):2749–2752, 1999.
- [31] J. Chen and D. C. Yang. Phase behavior and rhythmically grown ring-banded spherulites in blends of liquid crystalline poly(aryl ether ketone) and poly(aryl ether ether ketone). *Macromolecules*, 38(8):3371–3379, 2005.

- [32] J. Chen and D. C. Yang. Rhythmic growth of ring-banded spherulites in blends of liquid crystalline methoxy-poly(aryl ether ketone) and poly(aryl ether ether ketone). *Journal of Polymer Science Part B-Polymer Physics*, 45:3011–3024, 2007.
- [33] Yu. N. Taran and V.M. Snagovskii. Morphology of the eutectic in fe-c-cr alloys. *Metal Science and Heat Treatment*, 8(4):27–30, 1966.
- [34] Y. N. Taran. Theory of multiphase solidification of alloys. *Metal Science and Heat Treatment*, 19(9-10):846–850, 1977.
- [35] David J. Eyre. Cascades of spinodal decompositions in the ternary cahn-hilliard equations. In *Mathematics of Microstructure Evolution*, pages 367–378, 1996.

THIS PAGE INTENTIONALLY LEFT BLANK

## Chapter 5

# Solidification and melting of a ternary eutectic

At first glance, melting and solidification, which both involve a transformation between liquid and a solid, would appear to be inverses of each other. Experiments have repeatedly shown though that liquids must often be supercooled before they solidify, but solids can rarely be superheated without melting. This asymmetry has been the focus of centuries of scientific investigation, yet some aspects still cannot be completely explained. The current understanding of the finer aspects of solidification and melting is discussed in recent review articles [1, 2, 3]. A particularly interesting question that will be addressed in this chapter is why some solid alloys begin to melt below their melting point while others do not.

The presence of a nucleation barrier is usually cited as the reason why liquids may be supercooled, and phase field modeling of the nucleation process necessitates the development of a way to model the statistical fluctuations that trigger nucleation. Such a procedure is described in this chapter and nucleation, growth, and coarsening are studied in a ternary eutectic system and found to agree with basic theory. Beyond the simple observation that no energy barrier exists for melting, the explanation for the inability to superheat solids becomes complicated. The second half of this chapter

illustrates different aspects of the asymmetry between solidification and melting. An interesting finding is that the shape of free energy curves can qualitatively explain experimentally observed premelting behavior. It will be shown that metastable energy states have a large influence on microstructure evolution. Asymmetry introduced because of unequal diffusivity in solids and liquids will also be explored.

## 5.1 Phase-field model for nucleation

Nucleation occurs in systems where there is an energy barrier that inhibits transition from one phase to another. Nucleation is triggered when random fluctuations combine to produce a rare, localized critical event that crosses the barrier and leads to the growth of the lower energy phase. Within the context of the multiphase model, there are three different contributions to the energy barrier. The first is a compositional barrier which arises from differing equilibrium compositions of phases and the parabolic shape of their free energy curves. The second is the phase transition barrier discussed in Section 2.1.7, and the third is an energy penalty due to the creation of interface.

Figure 5-1 schematically illustrates the two ways noise can be added to trigger nucleation within the context of the multiphase model proposed in chapter 2. The illustration shows free energy curves for a binary system with three phases. A homogeneous system of phase  $\gamma$  with composition  $c_B = x$  can lower its free energy by phase separating into regions of  $\alpha$  with composition  $x_{eq}^\alpha$  and  $\beta$  with composition  $x_{eq}^\beta$ . The path from the initial to final state involves both changes in composition and changes in phase. Whether compositional fluctuations or fluctuations in phase are more important in generating critical nuclei is largely unknown.

Phase-field is particularly well-suited for modeling nucleation since the fluctuations that lead to nucleation occur on the length scale of an interface, and on that scale the diffuseness of interfaces is important. This section will demonstrate that the

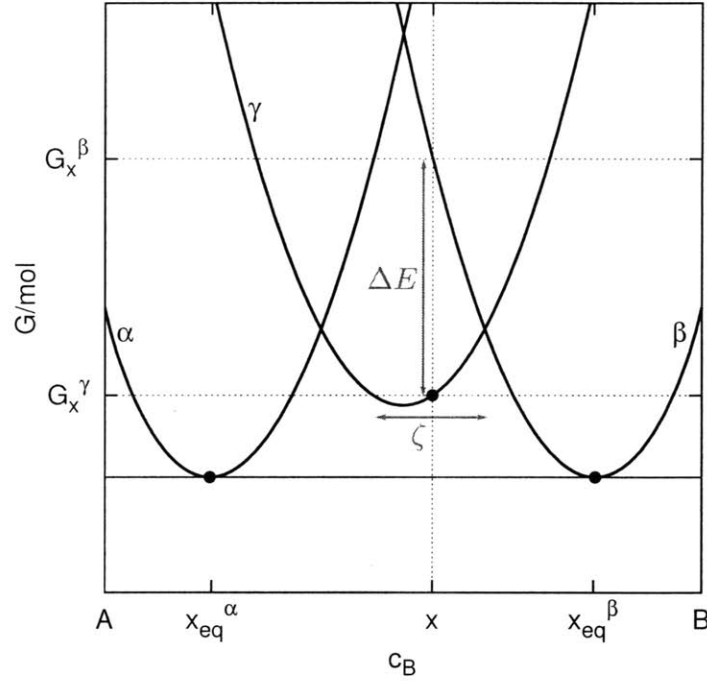


Figure 5-1: Two types of fluctuations can trigger a nucleation event in the multiphase, multicomponent model.  $\zeta$  illustrates composition fluctuations, and  $\Delta E$  is an energy fluctuation that converts one phase to another at constant composition.

multiphase model proposed in this work provides a natural way to model the nucleation process. Langevin noise will be introduced to model fluctuations in composition due to thermal noise, and a nucleation procedure will be proposed to introduce phase nuclei following a statistical energy distribution.

### 5.1.1 Stochastic Langevin noise

Langevin noise terms are frequently added to phase-field simulations to model the effect of thermal fluctuations [4, 5, 6, 7] and are used in this work to model fluctuations in composition. Following model C of Halperin, Hohenberg, and Ma [8], the component diffusion equations with Langevin noise terms  $\vec{\zeta}_1$  and  $\vec{\zeta}_2$  are:

$$\frac{\partial c_1}{\partial t} = \nabla \cdot \left( \frac{D_1 c_1}{RT} \left( (1 - c_1) \left( \nabla \frac{\delta F}{\delta c_1} \right) - c_2 \nabla \frac{\delta F}{\delta c_2} \right) + \vec{\zeta}_1 \right) \quad (5.1a)$$

$$\frac{\partial c_2}{\partial t} = \nabla \cdot \left( \frac{D_2 c_2}{RT} \left( (1 - c_2) \left( \nabla \frac{\delta F}{\delta c_2} \right) - c_1 \nabla \frac{\delta F}{\delta c_1} \right) + \vec{\zeta}_2 \right) \quad (5.1b)$$

Langevin noise is added inside the outermost gradient so that composition is conserved.  $\vec{\zeta}_1$  and  $\vec{\zeta}_2$  are vectors of random numbers that follow a Gaussian distribution. The vectors have two indices ( $i, j$ ) for 2D systems and three indices in 3D. The random numbers have a mean of 0 and a variance determined by the fluctuation-dissipation theorem [9, 10]. When a distribution has zero mean, its inner product is equivalent to its variance:

$$\langle \zeta_i(\vec{r}, t) \zeta_j(\vec{r}', t') \rangle = 2MRT \delta_{ij} \delta(\vec{r} - \vec{r}') \delta(t - t') \quad (5.2)$$

$M$  is the mobility of the component,  $\delta_{ij}$  is a Kronecker delta reflecting the fact that the noise in direction  $i$  is not correlated with the noise in direction  $j$ , and the two Dirac delta functions reflect that the noise is also not correlated in space or time.

In order to discretize the Langevin terms for simulation on a grid with grid spacing  $\Delta x$  and timestep  $\Delta t$ , appropriate scalings for the Dirac delta functions must be applied [4]:

$$\langle \zeta_i(\vec{r}, t) \zeta_j(\vec{r}', t') \rangle = \frac{2MRT}{\Delta t \Delta x^2} \delta_{ij} \delta_{rr'} \delta_{tt'} \quad (5.3)$$

The local magnitudes of the Langevin noise must also be adjusted to account for non-constant mobility. The diffusivity  $D$  and  $c(1 - c)$  in the expression for mobility both potentially vary in space and time. For a Gaussian distribution  $\zeta$  with variance  $\sigma^2 = \frac{2RT}{\Delta t \Delta x^2}$  (note that mobility has been omitted from the variance), the correct local scaling to account for varying mobility is:

$$\sqrt{Dc(1 - c)} \zeta \quad (5.4)$$

where  $M = Dc(1 - c)$ . Unless otherwise noted,  $RT = 10^{-6}$  was used to set the energy scale for compositional fluctuations in all simulations in this work, and Gaussian noise was generated using a Box-Muller transform [11] and the C++ `rand()` function.



### 5.1.2 Incorporating classical nucleation theory

Unfortunately for the computational modeling community, a brute force simulation of nucleation at small undercooling may never be achieved by any modeling method. A reasonable experimental nucleation rate of  $1/\text{cm}^2/\text{s}$  is way beyond the reach of both the time and length scales accessible by molecular dynamics, but capturing nucleation in continuum models requires very high space and time resolution because nucleation is such a rare event. Simulating nucleation events with Langevin noise in phase-field models is justifiable and elegant but easily becomes computationally prohibitive. One solution is to increase the variance of the noise, but this introduces numerical instabilities and produces fluctuations that are significantly different from real systems [6].

Attempts to model nucleation with phase-field methods have taken two different approaches. For highly undercooled systems far from equilibrium, Langevin noise is appropriate. For small undercooling however, the computational time necessary to simulate nucleation is prohibitive. Gaussian noise is expensive to generate, and small timesteps, grid spacings, and large domains are necessary. Thus it has become popular to introduce nuclei into phase-field simulations to trigger nucleation instead of using Langevin noise. Large fluctuations are added on the computational time scale in an attempt to capture the nucleation events that occur on much smaller length and time scales. Granasy et al. did this by randomly adding critical fluctuations that were calculated to match local composition [5, 6], and Langevin noise was added to determine whether or not the critical fluctuations nucleated. Unfortunately, calculation of a critical fluctuation becomes complicated in a multiphase system.

An alternative approach Simmons simulated nucleation by adding fully formed nuclei and adjusted the nucleation rate according to the local supersaturation [12, 13]. The nuclei were added to the conserved composition variable which lead to large concentration gradients, numerical instabilities, and a challenge maintaining mass conservation. A nucleation rate that varies with composition is also not easy to im-

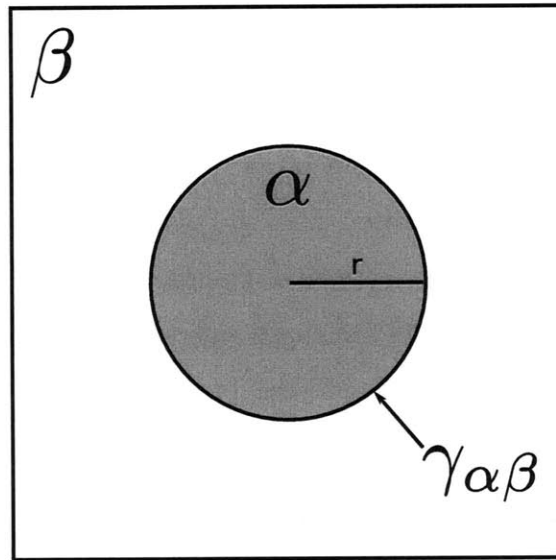


Figure 5-2: Classical nucleation of  $\alpha$  in  $\beta$  involves creation of a volume of  $\alpha$  separated from  $\beta$  by an interface with surface energy  $\gamma_{\alpha\beta}$ .

plement in practice. Another concern with Simmons's method is that the nuclei that are added are already completely transformed, unlike Granasy's critical fluctuations that push the system just to the top of an energy barrier rather than all the way over it.

A new approach for introducing nuclei is proposed here that uses elements of both techniques. The nucleation rate naturally becomes a function of local supersaturation as nuclei are added following a statistical energy distribution. Nuclei are added to the system at random locations, and the system decides which nuclei grow and which do not, much like a Monte-carlo simulation. The nucleation attempt rate is assumed to be constant everywhere, and the radius of the nuclei is adjusted so that the energy of the fluctuations obey a Gaussian distribution. Unlike the other nucleation models, there is no need for difficult calculations of the critical radius, and because phases are not conserved, adding nuclei by altering the phase variables poses no conservation challenges.

Figure 5-2 depicts a classical description of the formation of a nucleus of phase  $\alpha$

in a bulk region of phase  $\beta$ . The nucleus of  $\alpha$  has a lower free energy density than the  $\beta$  it replaces, and this free energy decrease drives the growth of the nucleus. The formation of the nucleus also introduces a surface energy  $\gamma_{\alpha\beta}$ , which contributes to a nucleation barrier. A nucleus is expected to grow when its radius is large enough that the free energy savings more than offsets the free energy increase due to the appearance of surface energy.

Classical nucleation theory assumes that the interface is sharp and that the interfacial energy of a nucleus is the same as that of a flat interface. Since the nuclei that are added computationally have sharp interfaces that are the width of a gridpoint, the classical model is appropriate for approximating the energy of a computational nucleus. In 2D, the classical energy of forming a nucleus of radius  $r$  is:

$$\Delta E = \pi r^2 \Delta F + 2\pi r \gamma \quad (5.5)$$

with  $\Delta f$  being the difference in free energy density between phase  $\alpha$  and  $\beta$ :

$$\Delta F = f_\alpha - f_\beta \quad (5.6)$$

In classical nucleation theory,  $\Delta F$  is negative and represents the energy savings driving the growth of the nucleus, which is assumed to already be at or close to its equilibrium concentration. This assumption is not necessary in the multiphase model. It is important to keep in mind though that when nuclei are added computationally with composition held constant,  $\Delta F$  will often be *positive*, as illustrated in figure 5-1.

Equation 5.5 can now be solved for the particle radius  $r$  corresponding to an energy fluctuation  $\Delta E$ . There are two solutions, but only one gives a positive radius:

$$r = \frac{-\gamma + \sqrt{\gamma^2 + \Delta F \Delta E / \pi}}{\Delta F} \quad (5.7)$$

In order to evaluate Eq. 5.7 it is necessary to approximate  $\gamma$ , the interfacial energy

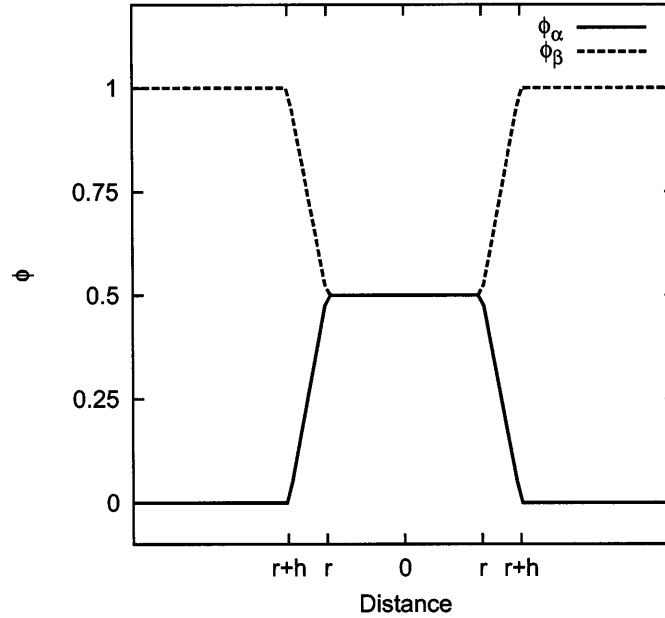


Figure 5-3: Profile of a nucleus of  $\alpha$  added to a matrix of  $\beta$  on a discrete grid. The nucleus has a radius of  $r$  and an interfacial width of  $h$ , the grid spacing.

introduced by the phase nucleus. An approximation for  $\gamma$  is acceptable because it is the system that ultimately determines which nuclei grow. The goal of the nucleation procedure is to introduce random nuclei that follow a Gaussian energy distribution, not to calculate the size or shape of the critical nucleus exactly.

To further simplify the calculation of the nucleus radius, the composition at the randomly chosen attempt sites is assumed to be constant over the small volume of the nucleus. This implies that composition gradients will not be included in the estimation of  $\gamma$ . To calculate interfacial energy within the context of the multiphase model it is necessary to evaluate Eq. 2.35 numerically. With the assumption of only phase gradient energy, the equation takes a simple form:

$$\gamma = \int_V \frac{1}{2} \Lambda_{\alpha\alpha} (\nabla \phi_\alpha)^2 + \frac{1}{2} \Lambda_{\beta\beta} (\nabla \phi_\beta)^2 dV \quad (5.8)$$

This form is correct for a diagonal phase gradient energy matrix  $\Lambda$ .

The assumption that nuclei have computationally sharp interfaces that are the

width of one gridpoint simplifies the calculation of  $\gamma$ . As illustrated in figure 5-3, the phase fractions change by a value of .5 over the width of a gridpoint at the interface. The magnitude of  $\nabla\phi$  is then  $.5/h$ , and therefore  $(\nabla\phi)^2 = .25/h^2$ . Because the phase gradients are assumed to be zero except at the interface, the expression for surface energy can be solved in 1D by integrating across the interface from  $r$  to  $r + h$ :

$$\begin{aligned}\gamma &= \int_r^{r+h} \frac{1}{2} \Lambda_{\alpha\alpha} (\nabla\phi_\alpha)^2 + \frac{1}{2} \Lambda_{\beta\beta} (\nabla\phi_\beta)^2 dr \\ &= \int_r^{r+h} \frac{\Lambda_{\alpha\alpha} + \Lambda_{\beta\beta}}{8h^2} dr \\ &= \frac{\Lambda_{\alpha\alpha} + \Lambda_{\beta\beta}}{8h}\end{aligned}\tag{5.9}$$

### 5.1.3 Nucleation algorithm

The nucleation procedure is as follows: Define a nucleation attempt rate for each phase and a variance for  $\Delta E$ . For each phase  $\alpha$ , match the nucleation attempt rate by randomly selecting locations. At each location, introduce a nucleus of  $\alpha$ . To do this, choose a random number for  $\Delta E$  from a Gaussian distribution. Use Eq. 5.6 to compute the energy change per unit volume for the phase transition<sup>1</sup>, and obtain a radius by solving Eq. 5.7. Introduce a circular nucleus to the system by setting  $\phi_\alpha = .5$  within a radius of  $r$  from the randomly chosen location. Multiply the rest of the phase fractions by .5 within the circular radius as well to account for the phase change. Continue running the simulation and let the system decide which nuclei grow.

## 5.2 Simulation of nucleation, growth, and coarsening

The nucleation procedure developed in the previous section was used to simulate nucleation and growth, and snapshots of the evolving microstructure can be found

---

<sup>1</sup>for a multiphase system, evaluate an expression like 2.12 for  $f_\beta$

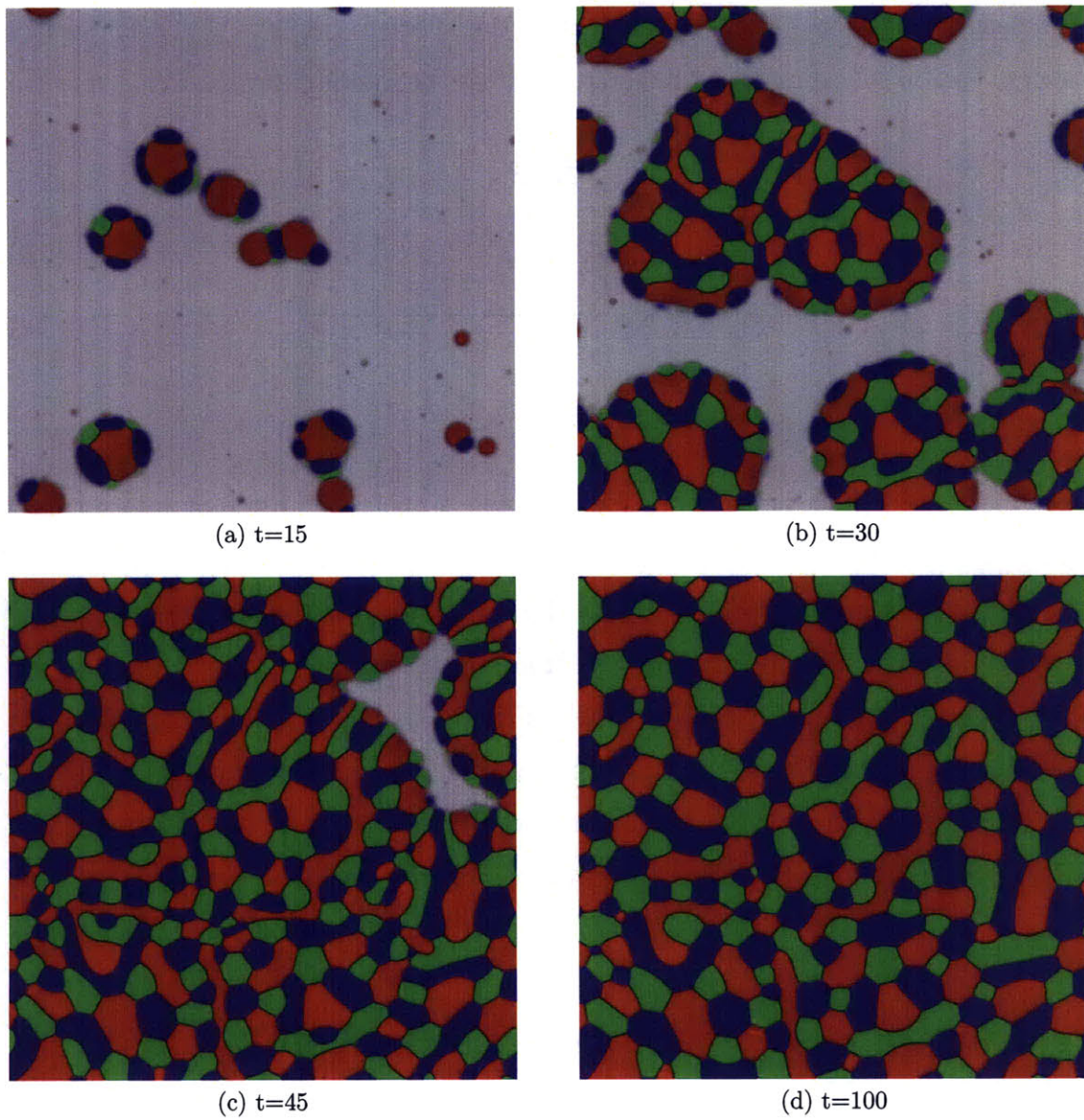


Figure 5-4: Simulation of nucleation, growth, and coarsening of a three-phase solid from a homogeneous metastable liquid. Diffusivity is equal in all phases.

in figure 5-4. The solidification is qualitatively similar to phase-field simulations of binary eutectic solidification performed by Drolet et al. [14]. A computational grid of  $512^2$  points, a grid spacing of  $h = .25$ , and  $k = .5$  were used in the simulation. The temperature of the liquid was  $T = -1.45$ , which corresponds to the free energy curves and phase diagram in figure 4-2. The initial condition was homogeneous metastable liquid of composition  $c = (.35, .31, .34)$ . A slightly off-center mean composition was chosen so that each phase would have a different nucleation barrier. Since the system is slightly red-rich, red has the lowest nucleation barrier. Red is observed to nucleate first at random locations as predicted by the rule of Stranski and Totomanow (difficult to verify experimentally), which states that the phase that nucleates in the one with the lowest barrier [15]. The growing nuclei then undergo secondary nucleation at the growth front and blue and green solid phases are observed to form. The growing structures maintain a roughly circular shape as in chapter 4, although symmetry is broken by the presence of Langevin noise and phase nucleation attempts. As the spherulites continue to grow, they begin to impinge on each other and eventually consume all of the liquid.

### 5.2.1 Analysis of nucleation and growth

Although there is no theory to describe nucleation and growth in ternary multiphase systems, the example presented here can be analyzed in terms of theories that govern simpler systems. The Johnson-Mehl-Avrami-Kolmogorov kinetics (JMAK) equation predicts the amount of transformed volume as a function of time for diffusion limited transformations with concurrent nucleation and growth, and a constant nucleation rate and constant growth rate [16]. Under these assumptions, the JMAK equation for a 2D system is:

$$X = 1 - e^{-\pi/3JR^2t^3} \quad (5.10)$$

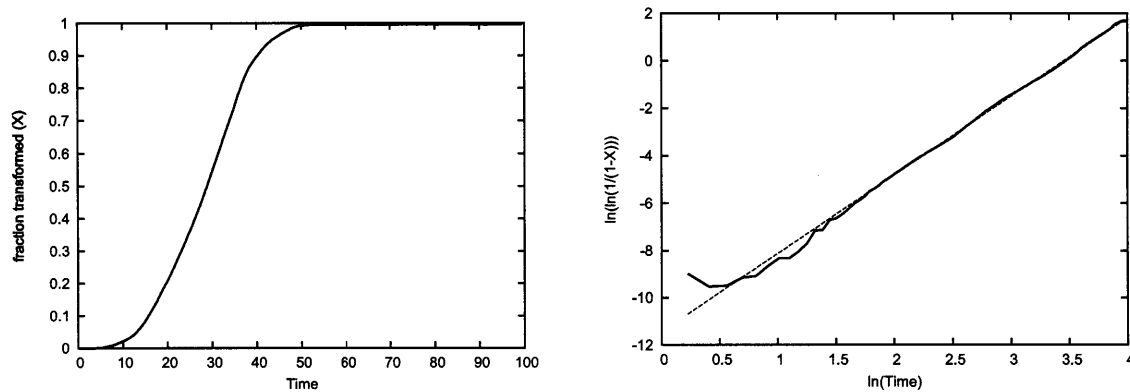


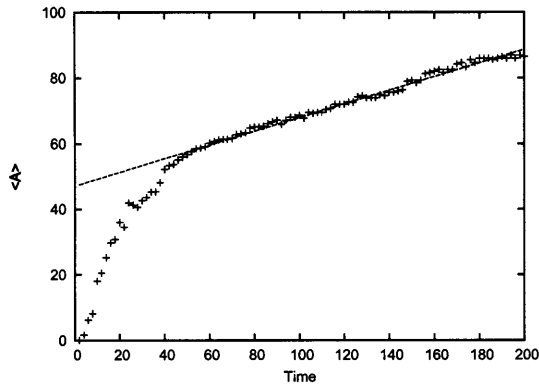
Figure 5-5: A plot of the fraction of liquid transformed in the solidification simulation, and a fit to the 2D JMAK equation. The slope of the fit line is 3.31.

Where  $X$  is the fraction of the system which has undergone the phase transition,  $J$  is the nucleation rate and  $R$  is the growth rate.

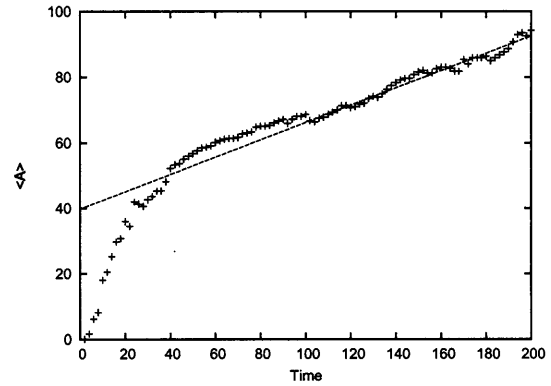
Since the multiphase solidification studied in chapter 4 was diffusion limited, there is hope that the JMAK equation might apply. Additionally, the growth rate of the three-phase spherulites was shown to be more or less constant in section 4.4.3, and the nucleation attempt rate is constant, although not necessarily the nucleation rate. Figure 5-5 shows a plot of the fraction of solid as a function of time, as well as a log plot used to determine the exponent of  $t$  in the JMAK equation. For a 2D system, the slope of the plot should be 3, and a slope of 3.31 was measured. The relationship is linear as expected, but the slightly larger than expected time exponent reveals that the transformation took place more quickly than predicted by theory.

The discrepancy is fairly minor however, confirming that the multiphase model and nucleation routine are behaving properly. The deviation from theory might be a result of the assumption of constant nucleation rate. The simulation only implements a constant nucleation attempt rate, while the actual nucleation rate is determined by the evolving system. Nucleation at the growth front is a complicating factor that is not accounted for in the JMAK analysis.





(a) With no intergranular film, the slope of the coarsening regime is .208.



(b) With an intergranular film, the slope of the coarsening regime is .263.

Figure 5-6: Coarsening of a ternary microstructure with and without the appearance of an intergranular film at  $t=100$ . The intergranular film, which forms as the result of an instantaneous temperature change, increases the coarsening rate by 25%.

## 5.2.2 Analysis of coarsening

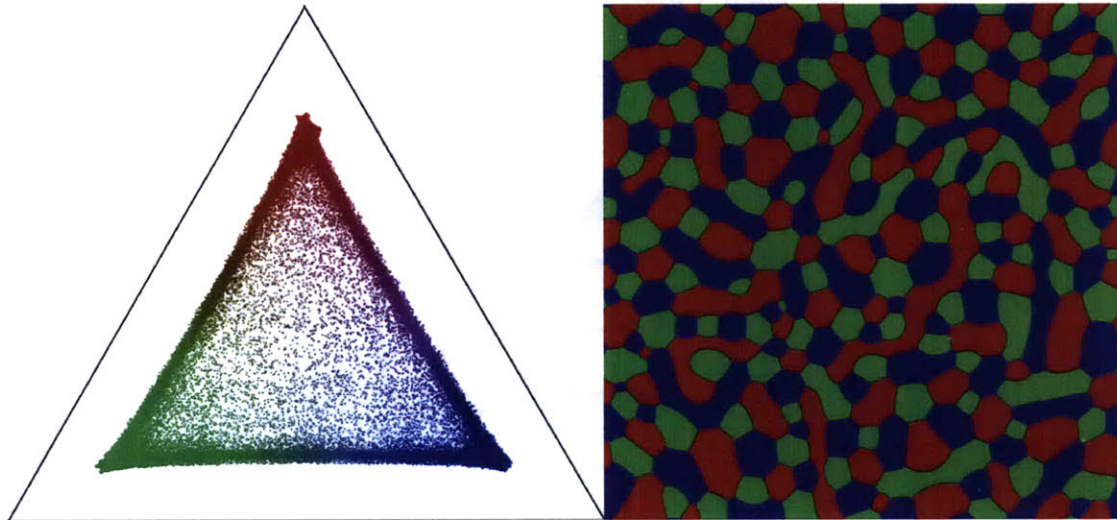
After the system has completely solidified, the solid begins to coarsen. In a 2D system with impinging particles and diffusion driven coarsening, the average particle area of particles is predicted to grow linearly. Figure 5-6a plots the average particle size over time during nucleation, growth, and coarsening regimes. The particles grow quickly at the beginning of the nucleation and growth stage, but as they impinge on each other the growth rate begins to slow. Around the nondimensional time of 60, a linear coarsening regime begins, and the coarsening rate constant is found by measuring the slope of a fit line. A computer program was written to calculate the number and size of particles in each of the phase fraction order parameters, and a contour of  $\phi = \frac{1}{2}$  was used to locate the particle boundaries. The coarsening rate, in non-dimensional units, was found to be .208. Since the surface energies of the solids are all equal, six-sided domains are predicted to be the most common as the system coarsens, according to the N-6 rule [16].

### 5.3 Coarsening at an elevated temperature

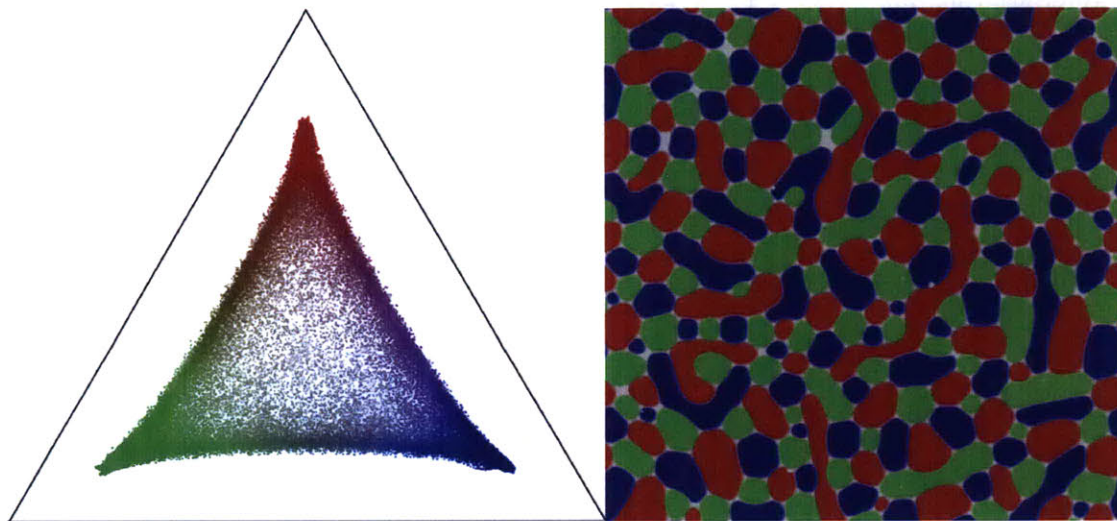
To study melting in a ternary multiphase system, the completely solidified microstructure from the previous section was brought to a higher temperature still below the melting point at time 100 and allowed to coarsen. Because the multiphase model assumes isothermal conditions, the temperature increase happens instantaneously. Figure 5-7 shows the microstructure just before and just after the temperature increase. Although the magnitude of the temperature increase was not large enough to produce a stable liquid region in the phase diagram, liquid is observed to form at triple junctions and phase boundaries. Image filters have been used to exaggerate the width of the liquid film in figure 5-7b for clarity of display. The unaltered liquid phase fraction for the same microstructure is presented in figure 5-8 to convey that liquid first pools at triple junctions while forming thin layers at phase boundaries.

The composition maps in figure 5-7 reveal the effect the metastable liquid curve has on the solid microstructure when temperature is increased. The composition variation at the diffuse solid interfaces shows up as straight, diffuse lines that connect the single phase regions in the composition map in figure 5-7a. When liquid forms at the phase triple junctions and phase boundaries, the interfacial composition profiles bow inward toward the center of the composition map, as shown in figure 5-7b.

The average particle size for the microstructure coarsened close to the melting point is plotted in figure 5-6b. The slope of the plot was measured starting after the temperature increase at time 100, and was found to be about 25% larger than for coarsening at low temperature, even though the initial solid microstructure was identical in both tests. The increased coarsening rate likely has two contributing factors. The first is that the metastable liquid curve, which is responsible for the premelting behavior, lowers the energy barrier for diffusion from one solid phase to another by providing a metastable, lower energy diffusion pathway through composition space. The second factor is that small particles become unstable at high temperature and melt as discussed in section 5.3.2, leaving larger particles to contribute to the average



(a) Just before the temperature increase,  $t=99.5$ .



(b) Shortly after the temperature increase,  $t=110$ .

Figure 5-7: Premelting is observed at triple junctions and phase boundaries when a three-phase microstructure is heated to a temperature ( $T=-.3$ ) slightly below the melting point. Time is reported in nondimensional units.



Figure 5-8: The liquid phase fraction for the microstructure in figure 5-7b. Liquid is white and solid is black. Premelting is observed in multiphase microstructure below the melting point. Liquid forms first at phase triple junctions and then at phase boundaries as temperature is increased.

size.

### 5.3.1 Premelting and metastable liquid

Solids are often but not always observed to begin melting below the melting temperature, with liquid appearing first at triple junctions and then at grain boundaries. Several explanations have been offered, including the general observation that grain boundaries and triple junctions are high energy sites that are less thermally stable than the bulk. Premelting of free surfaces has been studied extensively and has been described in terms of atomic thermal vibrations [1]. Melting at grain boundaries and triple junctions was first observed experimentally by Hsieh and Baluffi in aluminum [17]. Raj presented an analytic description of premelting at triple junctions and found that melt pockets at triple and higher order grain junctions can be thermodynamically stable, with a size inversely proportional to the undercooling [18]. Recently, premelting at grain boundaries has been modeled as a structural transition using a

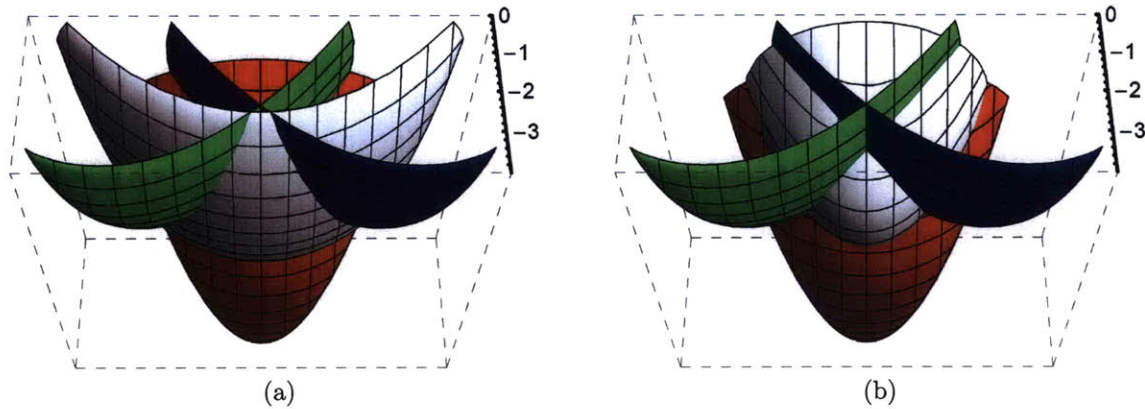


Figure 5-9: The shape of the liquid free energy curve determines whether premelting occurs at grain boundaries. The free energy at the minimum of the liquid curve is the same in both landscapes, but intergranular liquid films are only observed for the curve in (a). Both curves exhibit premelting at phase triple junctions.

diffuse interface model [19, 20, 21].

The argument that premelting occurs at crystal defects because they are high energy sites cannot be a complete description of premelting however, because in some experimental systems premelting is not observed. The multiphase model offers a plausible thermodynamic explanation for why some material systems premelt while others do not; premelting in the multiphase model results largely from the shape of the metastable regions of free energy curves. The explanation relies on the assumption that interfaces are diffuse and that points within an interface must therefore choose between various high energy states.

Just below the melting point, the liquid phase is not thermodynamically stable, although its energy minimum is not high above the common tangent plane. The liquid free energy curve is still lower than the solid free energy curves over a significant composition range, as illustrated in figure 5-9a. Liquid is metastable in these regions, because its energy is not as low as a phase separated three-phase solid mixture. An explanation for premelting is that the system makes use of these metastable liquid states, first at triple junctions where the energy difference between the solid curves

and the metastable liquid is largest, and then at grain boundaries where the difference is smaller but still favors the liquid over composition ranges far from the single phase solid regions.

Thickening of liquid films at grain boundaries as temperature approaches the melting point has also been observed experimentally. Thickening of the liquid films can be interpreted as an increase in the number metastable liquid states available with increasing temperature, illustrated in figure 5-9. As the liquid curve continues to descend, it becomes lower than the solid curves over a larger range of compositions, and the liquid film thickens. This diffuse interface interpretation of the width of the liquid layer may address why previous theoretical studies of grain boundary melting found it necessary to “incorrectly” assume that chemical potential in the liquid depends on the width of the liquid [22]. The diffuse-interface model developed in this work accounts for the effect of nonequilibrium material at the interface which penalizes interfaces differently based on their thickness.

### 5.3.2 Instability of small particles

Coarsening theory predicts that the radius of shrinking grains will smoothly decrease to zero. However, in phase field simulations of coarsening close to the melting point, shrinking grains were observed to melt when they became small rather than shrink to zero radius as a solid. The larger white pockets that are apparent in figure 5-8 are locations in the coarsening microstructure where small grains melted instead of continuing to coarsen as a solid.

The melting of small grains in figure 5-8 is a demonstration of the intrinsic instability of nanocrystalline materials that was predicted by Wagner [23] and reviewed in detail for experimental systems by Mei [2]. Wagner built on the premelting analysis of Raj [18] to show that there is a critical temperature above which a nanocrystal of radius  $r$  will become unstable. Figure 5-8 demonstrates the inverse of Wagner’s relationship; for a fixed temperature, there is a critical radius below which nanocrystals

become unstable and melt.

## 5.4 Asymmetry introduced by unequal diffusivity

Experimental measurements usually find that diffusion in a liquid is three to four orders of magnitude faster than in a solid, and is another source of asymmetry between melting and freezing. During melting the phase that forms has high diffusivity, but during solidification the phase that forms has low diffusivity. Thermodynamic and kinetic arguments have shown that the driving force for trans-interface diffusion (exchange of solute across the solid-liquid interface) disappears when the diffusivity of the parent phase approaches zero [3, 24]. Thus trans-interface diffusion is expected to occur during solidification, but not melting. For solidification, some of the driving force must be spent on trans-interface diffusion, while for melting, all of the driving force goes into interface migration.

One of the effects of differing diffusivities in the solid and liquid phases is that it is possible for concentration gradients to develop in solids at high at high solidification rates. Solid microstructures with concentration gradients are observed experimentally and form by a process called coring. When an alloy is cooled under nonequilibrium conditions and diffusion in the solid is limited, the composition of the solid formed initially at the core of the solidifying structure is not the same as the composition at the outer edge of the structure [25]. Concentration gradients do not form during melting, however, because of the high diffusivity in the liquid.

To investigate the effect of diffusion, a phase-field simulation of nucleation and growth was performed with slow diffusivity in the solid. The simulation parameters were the same as those used in the nucleation and growth simulation in section 5.2, except the diffusivity of each component was made to be a linear function of the liquid phase fraction  $\phi_4$ . The diffusivity of the liquid regions was kept at 1, but the diffusivity in the solid regions was decreased by three orders of magnitude to 1/1000.

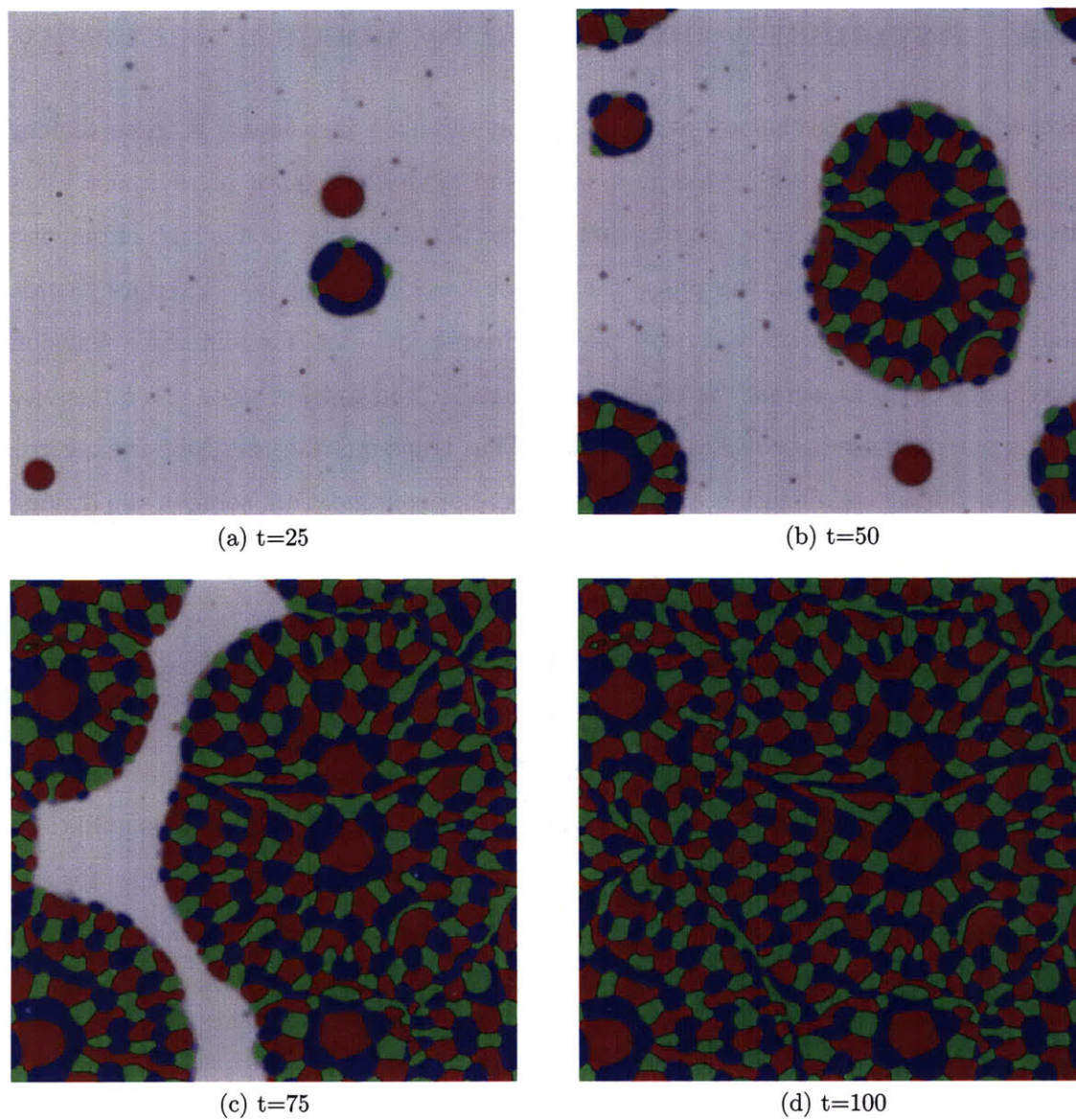


Figure 5-10: Simulation of nucleation, growth, and coarsening of a three-phase solid from a homogeneous metastable liquid. Diffusivity is three orders of magnitude slower in the solid than in the liquid. Time is reported in nondimensional units.



Decreasing the solid diffusivity while holding the relaxation parameters constant in the phase evolution equations simulates solidification with a rapidly moving interface.

Figure 5-10 contains snapshots from a simulation of nucleation and growth with a diffusivity in the solid of  $1/1000$ . The microstructure that forms is visibly different than formed under conditions of equal diffusivity (figure 5-4). The microstructure consists of smaller, rougher particles that are less equiaxed and do not coarsen on the time scale of the simulation. The particles are also a noticeably different shade of color, with a somewhat washed-out appearance. The composition map in figure 5-11a provide an explanation. With slow solid diffusivity, solidification occurred at compositions outside the stable single phase regions. Once the system has frozen in a supersaturated state though, it is essentially stuck because reaching equilibrium now requires significant solid diffusion.

Figures 5-11 (b)-(d) show what happens to the microstructure shortly after the temperature is increased to  $T = -.3$ , a value just below the melting temperature (the same temperature as in figure 5-7). Once again the composition maps help to clarify what is happening, especially when compared to the equal diffusivity case (figure 5-7). The solidified microstructure is initially out of equilibrium but unable to evolve, being frozen in place. The temperature increase initially causes the highest energy compositions to melt because the solid phases are supersaturated with solute. Interestingly, the regions that melt appear to be the areas that solidified last. Large pools of liquid form, but eventually the grains surrounding these liquid regions begin to grow back into the liquid. By figure 5-11d, some of the liquid regions have begun to re-solidify. The evolution is evident in the composition map, which evolves from an initial diffuse spray of compositions toward thinner lines of composition connecting the single phase regions. The composition map relaxes to a profile similar to figure 5-7 indicating that the system is evolving toward equilibrium.

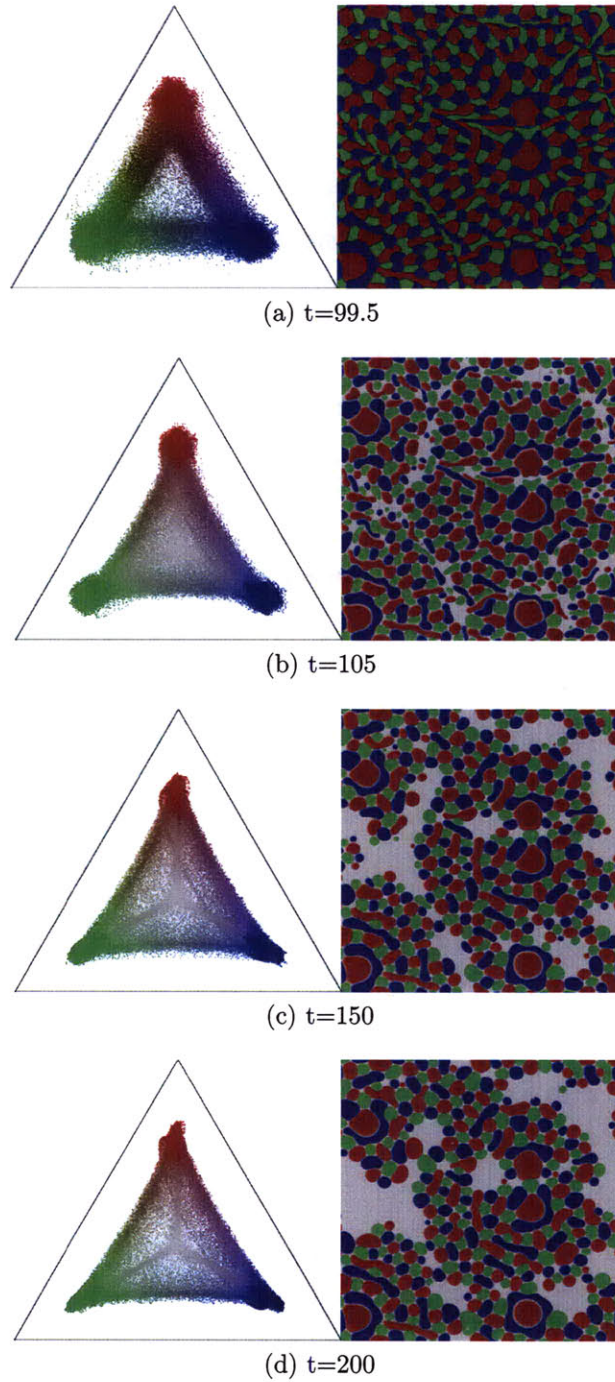


Figure 5-11: Solutal melting and re-solidification of a rapidly solidified multiphase microstructure held at a temperature below the melting point. The diffusivity in solid is  $1/1000$  the diffusivity in the liquid. Time is reported in nondimensional units.

## References

- [1] J. G. Dash. History of the search for continuous melting. *Reviews of Modern Physics*, 71(5):1737–1743, 1999. 97 AMERICAN PHYSICAL SOC COLLEGE PK 270PF.
- [2] Q. S. Mei and K. Lu. Melting and superheating of crystalline solids: From bulk to nanocrystals. *Progress in Materials Science*, 52(8):1175–1262, 2007. Mei, Q. S. Lu, K.
- [3] M. Rettenmayr. Melting and remelting phenomena. *International Materials Reviews*, 54(1):1–17, 2009. Rettenmayr, M.
- [4] A. Karma and W. J. Rappel. Phase-field model of dendritic sidebranching with thermal noise. *Physical Review E*, 60(4):3614–3625, 1999. Part A.
- [5] L. Granasy, T. Borzsonyi, and T. Pusztai. Nucleation and bulk crystallization in binary phase field theory. *Physical Review Letters*, 88(20):4, 2002. 38 AMERICAN PHYSICAL SOC 549UY.
- [6] L. Granasy, T. Pusztai, and J. A. Warren. Modelling polycrystalline solidification using phase field theory. *Journal of Physics-Condensed Matter*, 16(41):R1205–R1235, 2004.
- [7] L. Granasy, T. Pusztai, T. Borzsonyi, G. Toth, G. Tegze, J. A. Warren, and J. F. Douglas. Phase field theory of crystal nucleation and polycrystalline growth: A review. *Journal of Materials Research*, 21(2):309–319, 2006.
- [8] B. I. Halperin, P.C. Hohenberg, and S. Ma. Renormalization-group methods for critical dynamics .1. recursion relations and effects of energy conservation. *Physical Review B*, 10(1):139–153, 1974.
- [9] P. C. Hohenberg and B. I. Halperin. Theory of dynamic critical phenomena. *Reviews of Modern Physics*, 49(3):435–479, 1977.

- [10] J.D. Gunton, M. San Miguel, and Paramdeep S. Sahni. The dynamics of first-order phase transitions. In *Phase Transitions and Critical Phenomena*. Academic Press Inc., 1983.
- [11] G. E. P. Box and M. E. Muller. A note on the generation of random normal deviates. *Annals of Mathematical Statistics*, 29(2):610–611, 1958.
- [12] J. P. Simmons, C. Shen, and Y. Wang. Phase field approach to transformations involving concurrent nucleation and growth. In A. Gonis, P. E. A. Turchi, and A. J. Ardell, editors, *Symposium on Nucleation and Growth Processes in Materials held at the 1999 MRS Fall Meeting*, volume 580, pages 417–427, Boston, Ma, 1999.
- [13] J. P. Simmons, C. Shen, and Y. Wang. Phase field modeling of simultaneous nucleation and growth by explicitly incorporating nucleation events. *Scripta Materialia*, 43(10):935–942, 2000. 33 PERGAMON-ELSEVIER SCIENCE LTD 373AK.
- [14] F. Drolet, K. R. Elder, M. Grant, and J. M. Kosterlitz. Phase-field modeling of eutectic growth. *Physical Review E*, 61(6):6705–6720, 2000. Part B.
- [15] I. N. Stranski and D. Totomanow. Seed formation speed and ostwald’s step rule. *Zeitschrift Fur Physikalische Chemie-Abteilung a-Chemische Thermodynamik Kinetik Elektrochemie Eigenschaftslehre*, 163(5/6):399–408, 1933.
- [16] Robert W. Balluffi, Samuel M. Allen, and W. Craig Carter. *Kinetics of Materials*. John Wiley & Sons, Inc., 2005.
- [17] T. E. Hsieh and R. W. Balluffi. Experimental-study of grain-boundary melting in aluminum. *Acta Metallurgica*, 37(6):1637–1644, 1989.
- [18] R. Raj. Premelting at triple grain junctions. *Acta Metallurgica Et Materialia*, 38(8):1413–1416, 1990.

- [19] M. Tang, W. C. Carter, and R. M. Cannon. Diffuse interface model for structural transitions of grain boundaries. *Physical Review B*, 73(2), 2006.
- [20] M. Tang, W. C. Carter, and R. M. Cannon. Grain boundary order-disorder transitions. In *Brandon Symposium on Advanced Materials and Characterization held at the 2006 TMS Annual Meeting*, volume 41, pages 7691–7695, San Antonio, TX, 2006. Tang, Ming Carter, W. Craig Cannon, Rowland M.
- [21] M. Tang, W. C. Carter, and R. M. Cannon. Grain boundary transitions in binary alloys. *Physical Review Letters*, 97(7), 2006. Tang, Ming Carter, W. Craig Cannon, Rowland M.
- [22] G. F. Bolling. On average large-angle grain boundary. *Acta Metallurgica*, 16(9):1147–&, 1968.
- [23] M. Wagner. Intrinsic instability of nanocrystalline metals. *Acta Metallurgica Et Materialia*, 40(5):957–959, 1992.
- [24] M. Hillert and M. Rettenmayr. Deviation from local equilibrium at migrating phase interfaces. *Acta Materialia*, 51(10):2803–2809, 2003. 5 PERGAMON-ELSEVIER SCIENCE LTD OXFORD 691HF.
- [25] D.A. Porter and K.E. Easterling. *Phase Transformations in Metals and Alloys*. Stanley Thornes (Publishers) Ltd, 2000.

THIS PAGE INTENTIONALLY LEFT BLANK

## Chapter 6

# Transient liquids and reactive phases

Transient liquid phase bonding (TLPB) is a commonly used process for producing strong bonds between materials that are difficult to join, perhaps because they cannot be welded or suffer from thermal cracking when welded. TLPB is commonly used to bond metals, ceramics, composites, and semiconductors, and has been employed in the aerospace industry for several decades. It is also useful for joining small devices and has found application in MEMS and microelectronics. TLPB produces interface-free bonds that are identical chemically and structurally to the parent materials. The bonds are therefore more stable at high temperature than materials joined by brazing, yet TLPB bonding requires lower temperatures than welding. The liquid that forms during TLPB wets the solid, eliminating the need for the high clamping force required in diffusion bonding. Review papers by MacDonald and Eagar [1] and [2] provide detailed descriptions of specific materials systems where TLPB is used.

There have been many attempts to model the transient liquid bonding process, but they have all made restrictive assumptions and as a result have only met with mixed success. The models simplify the TLPB process, breaking it into discrete stages and modeling each stage with linear diffusion equations, when in reality TLPB

is a complicated, continuous, nonlinear process. Surprisingly, there has been only one very recent attempt to model TLPB with phase-field, and only the solidification stage was modeled [3]. Modeling the entire process is important because the stages can occur simultaneously, and the initial conditions for each stage are controlled by the stage that precedes it.

This chapter will demonstrate that phase-field is ideal for modeling TLPB and addresses all of the deficiencies with previous modeling attempts. It will be shown that the multiphase model developed in this work captures all of the experimentally observed behavior in the bonding process including stages II and IV which have not previously been modeled. This work is also the first report of a multidimensional TLPB model, and the first TLPB model capable of simulating arbitrary geometries. The composition profile in the transient liquid is also reported here for the first time.

## 6.1 Simulation of transient liquid bonding

TLPB makes clever use of the fact that the melting point in a eutectic system is a function of composition, and the transience of the liquid phase arises from composition changes that occur because of diffusion. A thin interlayer of material is sandwiched between substrates of the material to be joined, and the interlayer and substrate form a eutectic system with the interlayer acting as a melting point depressant. Localized liquid forms as interdiffusion progresses at the interlayer-substrate interface, and the liquid eventually wets the substrate. Capillary forces then bond the two pieces of substrate. As diffusion progresses further, the composition of the liquid hits the liquidus line in the eutectic phase diagram, and the liquid solidifies, producing an interface-free bond.

TLPB will now be modeled here with a simulation employing the multiphase model derived in chapter 2 and the free energy landscape from section 4.1. A fifth phase, a compound of 50%  $c_1$  and 50%  $c_2$ , is added to the energy landscape. The



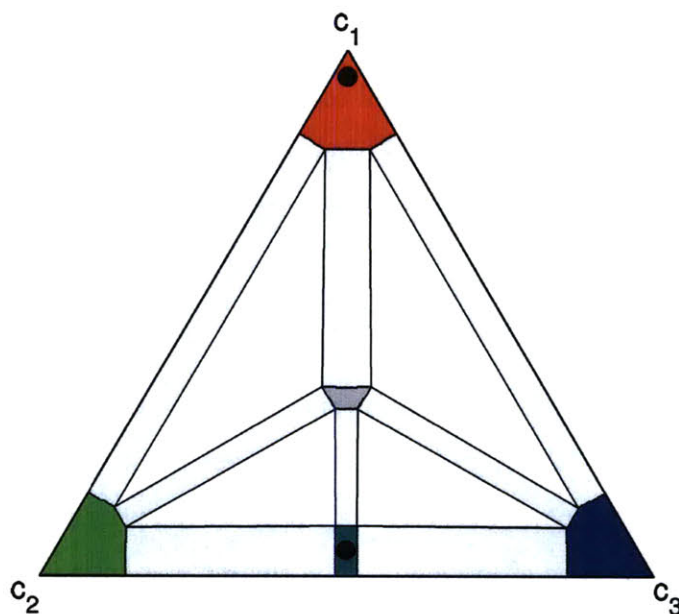


Figure 6-1: The phase diagram used for simulating transient liquid bonding. A fifth phase of composition  $c = (.5, .5, 0)$  has been added to the system. The dots indicate the compositions of the initial phases in the simulation.

phase diagram with this compound added is shown in figure 6-1. The free energy density of the new phase is:

$$f_5(c_1, c_2) = f(c_1 + 1/3 - .5, c_2 + 1/3 - .5) + \Delta G_{mix} \quad (6.1)$$

$\Delta G_{mix}$  and  $f(c_1, c_2)$  are defined in section 4.1. This blue-green phase is an attempt to simulate a stoichiometric line compound with little solid solubility that forms from a reaction of blue and green. The blue-green phase has a small amount of solubility in practice because a true line compound cannot be modeled with a diffuse interface method.

The fifth phase was introduced to create a binary eutectic-like reaction involving this new blue-green phase, the red phase, and the silver liquid phase. A more complicated reaction that is unique to a ternary system will be presented in section 6.4. A transient liquid bond can be made by sandwiching a thin interlayer of the blue-green

phase between substrates of the red phase and allowing the system to react. The black dots in figure 6-1 indicate the initial compositions of the base material and the interlayer in the simulation, and the diffusion path connecting the two phases passes through a region of stable liquid phase. Thus a transient liquid is expected to form.

### 6.1.1 The four stages of TLPB

The results of the transient liquid bonding simulation are displayed in figure 6-2 and will be used to illustrate the four stages of transient liquid phase bonding. Figure 6-3 shows corresponding plots of solute concentration across the interfaces in figure 6-2. Since the simulation is effectively a binary eutectic reaction contained within a ternary system,  $c_2 + c_3$  may be taken as the solute concentration. In this case  $c_1$  and  $c_2$  maintain the same profile at interfaces since they occur in equal amounts and with equivalent energetics and kinetics. A computational grid of  $1024 \times 256$  points, a grid spacing of  $h = .25$ , and  $k = .25$  were used in the simulation. The pictures in figure 6-2 are 512 gridpoints wide and have been cropped to highlight the interlayer region.

The first stage of TLPB is dissolution, which requires only short-range diffusion and as a result usually occurs on the order of minutes experimentally. Interdiffusion near the substrate-interlayer interface brings regions of the system into the stable liquid region of the phase diagram. A liquid film forms at the outer edges of the interlayer and progresses inward toward the center of the interlayer, eventually meeting at the center of the interlayer, as illustrated in figures 6-2 (b)-(d).

The second stage involves widening of the liquid layer, although in experiment, the dissolution stage and the widening stage often overlap. The width of the liquid increases as the liquid is further diluted with  $c_1$  and  $c_2$  and continues moving toward the liquidus line of the substrate phase. Eventually the liquid region reaches a maximum width, which occurred at time=80 in the simulation (figure 6-2d and 6-3c). Evidence of widening is visible in the interface composition profiles of figure 6-3 with the help of the vertical dashed lines that mark the location of the initial interfaces.

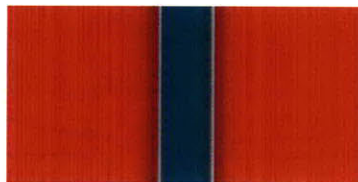
(a)  $t=0$ (b)  $t=2$ (c)  $t=40$ (d)  $t=80$ (e)  $t=600$ (f)  $t=820$ 

Figure 6-2: A phase-field simulation of transient liquid bonding in a ternary system. Time is reported in nodimensional units.

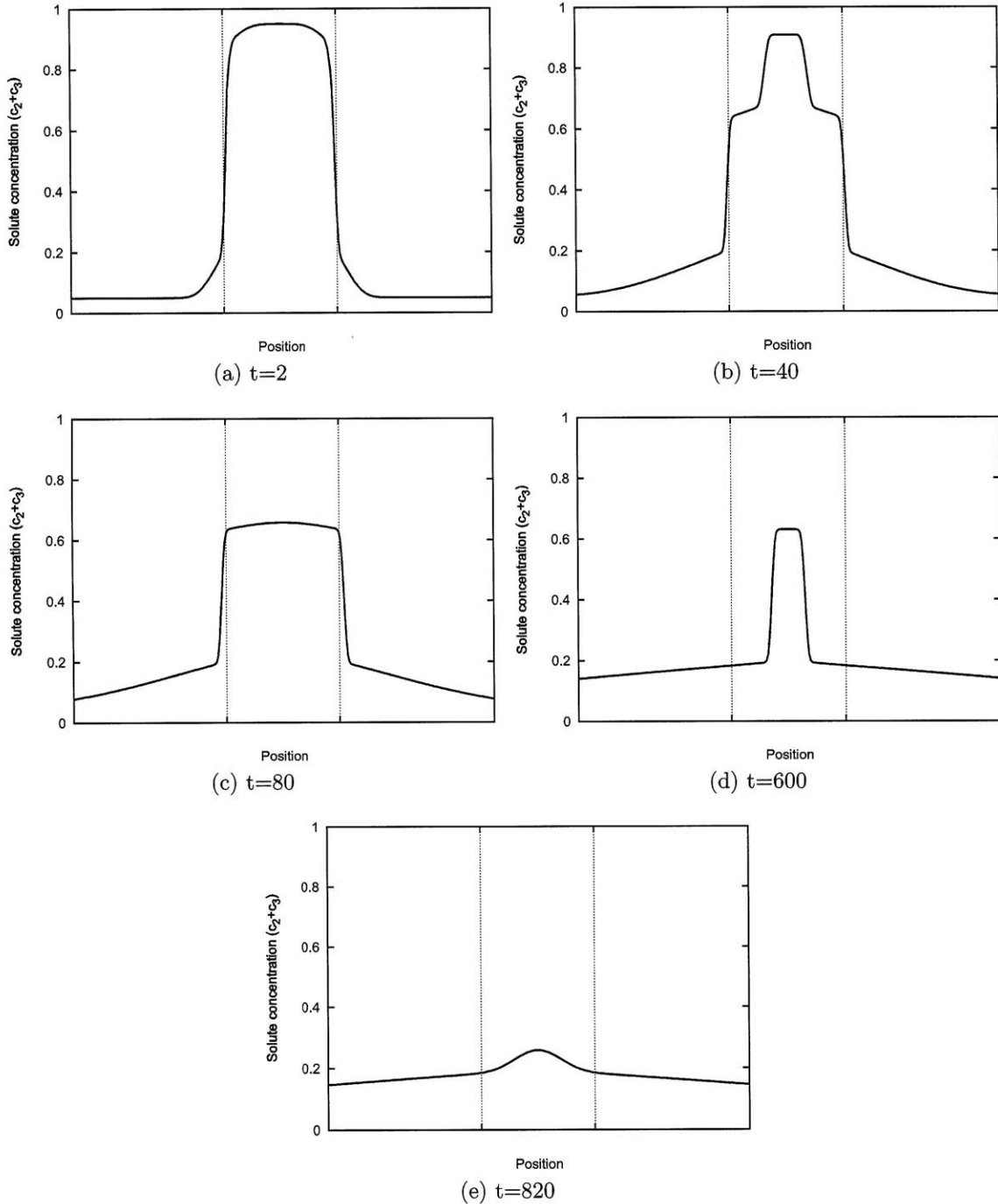


Figure 6-3: Plot of solute concentration at the interlayer during transient liquid bonding. The vertical dashed lines mark the initial position of the interlayer. The plots correspond to the microstructures in figure 6-2.

There is not a significant amount of widening in the simulation because the liquid region in the phase diagram is small. The amount of widening could be increased by raising the dissolution temperature so that the size of stable liquid phase region increases.

Isothermal solidification of the liquid layer occurs during the third stage. As solute from the liquid layer continues to diffuse into the solid, the liquid begins to solidify. The liquid region shrinks, and eventually disappears, as illustrated in figures 6-2e and 6-2f. The isothermal solidification stage is generally very time consuming because it is limited by long-range diffusion of the solute into the substrate, and can take anywhere from several minutes to many hours experimentally. The solidification time is also specific to each system, strongly depending on diffusivities in the solid, the shape of the phase diagram, and the composition and thickness of the interlayer. For this reason, the solidification stage has been the focus of most TLPB modeling efforts.

After the liquid has solidified the bond must be held at the solidification temperature so that the solute can homogenize. Homogenization is necessary to avoid precipitation of unwanted phases at the interlayer as the bond is cooled. Figure 6-3e reveals that even after the interlayer has solidified, there is still a high solute concentration in the area where the liquid used to be. The homogenization stage is usually very slow because it too is dependent on long-range diffusion, and can range from several hours to several days. And like isothermal solidification, the homogenization time is specific to each system with the phase diagram, energetics, and kinetics playing a big factor.

## 6.2 Discussion of TLPB models

The transient liquid bonding process lends itself to modeling because it has direct technical importance yet is time consuming to study and optimize experimentally.

Since the process is highly dependent on system parameters and can take many hours to complete in practice, a predictive model for optimizing the parameter selection process would be extremely helpful. Unfortunately, modeling of TLPB has only achieved moderate success because, in the words of Gale [2], the models lack of sophistication. All of the currently proposed models have made large assumptions that severely limit their applicability. Despite several decades of work, no model has successfully captured all four stages of the transient liquid bonding process. It is important to review several aspects of the current models in order to show why they have been unsuccessful and why phase-field is well suited for modeling TLPB. Many of the TLPB individual modeling attempts have been critiqued in review papers [1, 4, 5, 2].

A serious problem with current models is that they simplify the bonding process by dividing it into discrete stages that are each modeled separately, even though the stages are observed to occur simultaneously. Breaking the process into stages makes it easier to model the process with linear diffusion equations that can be solved analytically, although the use of diffusion equations to model phase-separating systems is a significant simplification that was discussed in section 1.2.2. The diffusion equation with concentration as a driving force applies only to ideal systems and cannot describe systems that phase separate. Limited thermodynamic data is included in the models, and planar interfaces, isothermal conditions, and completely sharp interfaces with a jump in composition are usually assumed.

Transient liquid phase bonding models have largely focused on modeling the isothermal solidification stage because it is a limiting step in the bonding process as well as a stage that is relatively easy to model. Modeling the isothermal solidification stage with diffusion equations quickly becomes challenging because of the presence of the moving solid-liquid boundary, which cannot be accounted for with diffusion equations alone. Models have therefore had to make simplifying assumptions about the interface. Some have modeled just the base material as a semi-infinite phase with the

solute concentration of the liquid as one of the boundary conditions [6]. While simple, this method does not predict accurate solidification times [5]. Other approaches have treated the moving interface as a jump in concentration occurring at a single moving gridpoint. This too is a simplification as there is no physical justification for modeling an interface as a composition shock. Illingworth et al. studied numerical solutions of diffusion equations with sharp interfaces and found that tracking the sharp interface presents a numerical challenge [7, 8]. Specifically, the ability to estimate error and adjust the timestep is an important idea that has not been addressed. The adaptive numerical methods studied in chapter 3 may be a solution to this problem.

There have been a few attempts to derive models for isothermal solidification in ternary systems [9, 10]. Campbell and Boettinger reported using the commercially available DICTRA code which incorporates composition dependent diffusivities and multicomponent thermodynamics to simulate transient liquid bonding, although simulations were only performed in 1D and diffusion was only modeled in the base material [11]. Attempting to model complex nonlinear behavior with linear equations again proved difficult, in part because ternary systems are significantly more complicated than binary systems. The assumption of constant equilibrium composition in the solid and liquid at the interface no longer holds in a ternary system. The equilibrium concentrations change continually and must be found from mass balance equations governed by tie lines on the phase diagram<sup>1</sup>. Planar interfaces and complete mixing in the liquid layer must also be assumed. In contrast, the phase-field model developed in this work is governed by the free energy curves themselves and mass balance is implicitly included in the model, as are the ability to simulate complex morphologies and concentration gradients.

---

<sup>1</sup>This process is similar to the expensive quasiequilibrium calculation in the Eiken multiphase, multicomponent model [12] discussed in section 1.2.2

### 6.3 Cellular solidification

The formation of cellular structures due to gradients in temperature and composition is a well known phenomenon in materials science [13], and the transition between planar and cellular structures has previously been modeled with phase-field methods [14]. Experimental studies of TLPB have often observed that solidifying interfaces do not remain planar during isothermal solidification [1, 2]. Cellular morphologies are common and are believed to form as a result of constitutional supercooling [15]. Constitutional supercooling occurs when solute builds up in front of a quickly solidifying interface, causing the liquid to become supercooled without a change in temperature. The moving planar interfaces then break up into cells via a Mullins-Sekerka instability [16, 17].

An interesting recent discovery is that a cellular solidification morphology improves the mechanical performance of transient liquid bonds compared to bonds with a flat bond interface while decreasing bonding time [18, 19]. Planar solidification was disrupted by performing transient liquid bonding with a temperature gradient across the interface, which induces a composition gradient in the liquid. It is thought that a planar bond line tends to concentrate oxides and other impurities and does not provide as much bonding surface area as a wavy bond line. Being able to control the morphology very carefully is important because the formation of dendrites was found to weaken the bond. The temperature gradient bonding method was very recently modeled with a 2D phase-field method that included grain structure [3].

A newer discovery is that heat treatments can be used instead of a temperature gradient to trigger cellular growth during transient liquid bonding. Wang et al. report using this approach to create bonds with the mechanical strength of the parent material in minutes instead of hours [20, 21]. The interlayer is first heated to high temperature and held for a few seconds to trigger the dissolution, and then the bond is held at a lower temperature during isothermal solidification, which finishes in just a few minutes. The lower holding temperature is in a region of constitutional



supercooling that produces cellular solidification. Compared to the temperature gradient method, this multiple heat treatment technique appears experimentally easier to control and potentially faster.

A simulation of a cellular structure during the isothermal solidification stage of a transient liquid bond is shown in figure 6-4, with the liquid phase colored silver. In order to trigger cellular growth, several phase-field parameters were adjusted from the simulation presented in section 6.1. First, the composition of the liquid was moved closer to the red-rich phase:  $c=(.7,.15,.15)$ . This would be achieved experimentally by performing the TLPB dissolution stage at a higher temperature than in the original simulation so that the liquid phase region would be larger than in the phase diagram of figure 6-1. Second, the liquid was made unstable by quenching the system to a temperature of  $T = -.2$ . Third, the diffusivity of the components in the solid was set to 1/1000 the diffusivity in the liquid to more closely agree with experimental observations. Finally, the phase barrier height was increased to  $W = .5$  and the velocity of the solidifying interface was increased by changing the relaxation parameter from  $\tau = 1$  to  $\tau = .1$ .

Being able to accurately predict the morphology of the solidifying liquid interlayer is an important technical problem that can be addressed with the multiphase model developed in this work. Since the model captures all of the TLPB stages, it could be used to optimize annealing times and temperatures in bonding processes involving multiple heat treatments.

## 6.4 Simulation of reactive bonding

The TLPB simulations that have been presented essentially simulated transient liquid bonding in a binary eutectic, even though technically the system had three components and five phases. The ability of the multiphase model to capture complicated reaction pathways is highlighted here with a transient liquid bonding simulation that

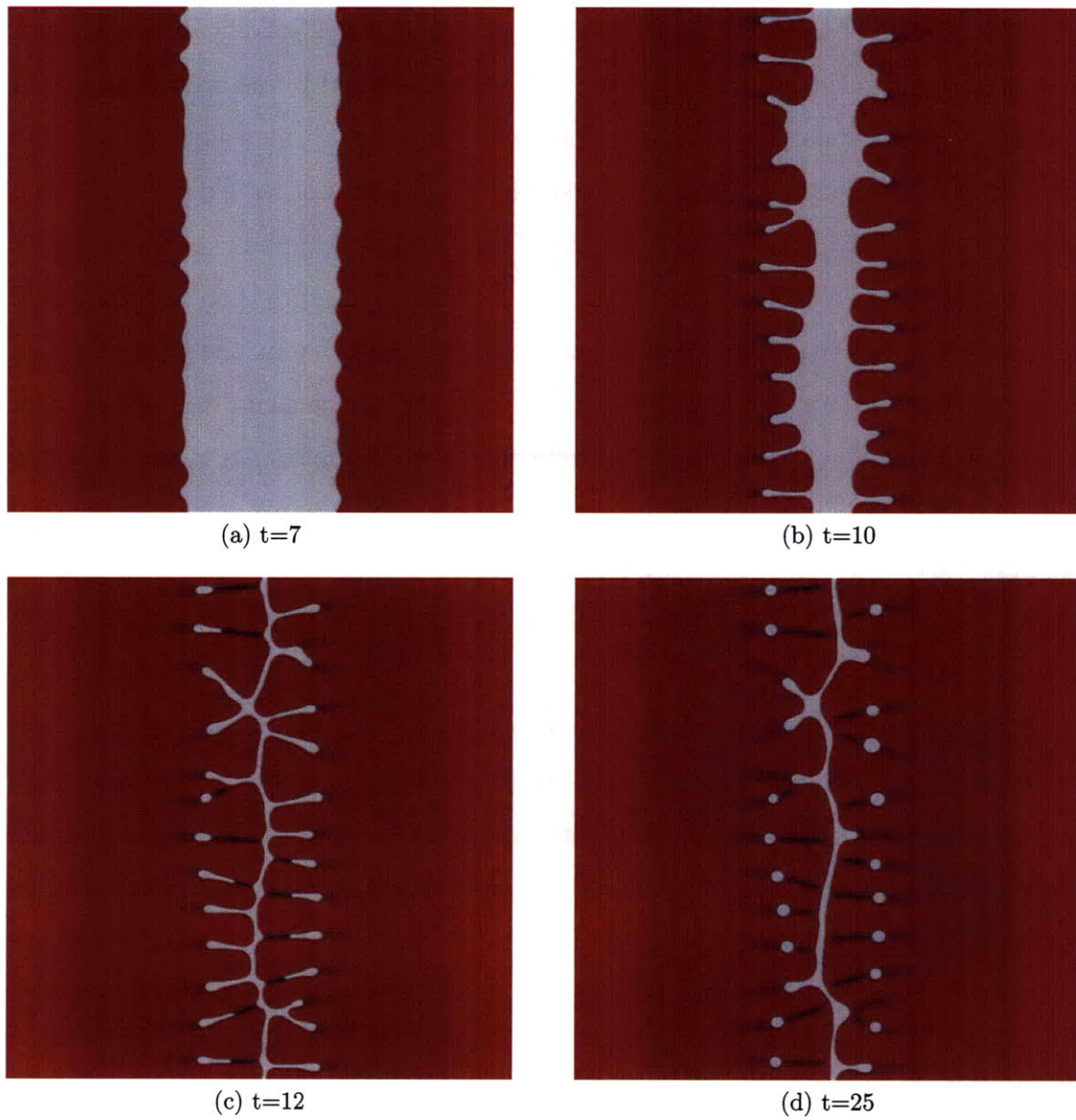


Figure 6-4: Simulation of cellular growth during the isothermal solidification stage of a transient liquid bond.

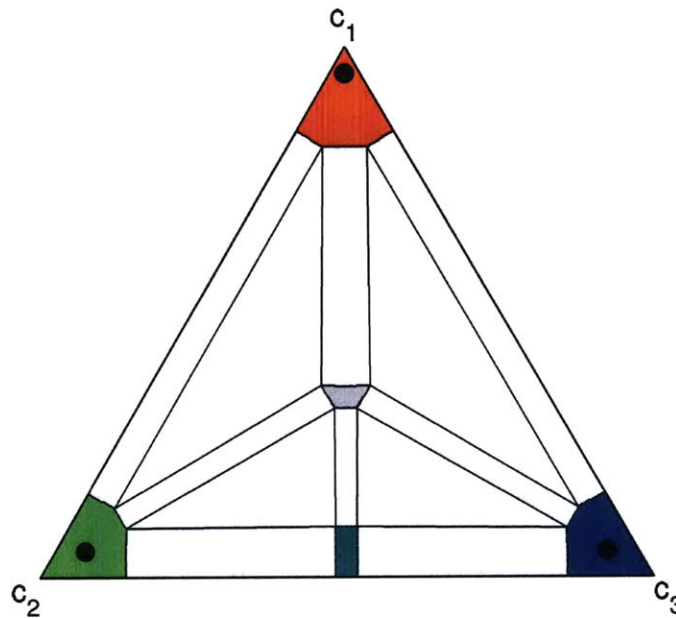


Figure 6-5: The phase diagram used for the reactive liquid bonding simulation.

is inherently ternary. The reaction also produces two different transient phases.

Imagine that formation of the blue-green phase from the blue phase and green phase involves an expensive processing step, possibly at high temperature. Rather than starting with the blue-green phase as the interlayer material, it could be cheaper to apply a thin layer of the green phase to one of the substrates and a thin layer of the blue phase to the other. The initial interlayer is now half blue and half green, and the starting compositions are identified in figure 6-5.

Dissolution of the new geometry is shown in figure 6-6. Blue and green first react to form the blue-green phase, which then reacts with the red phase to form a transient liquid. Two transient phases have formed during the reaction. Although the formation of the liquid takes longer than starting with the blue-green phase, the time from the beginning of the reaction until no more liquid remains is the same. What is particularly interesting about this reaction is that neither the green nor the blue interlayer would react with the red to produce a liquid, yet a liquid forms anyway.

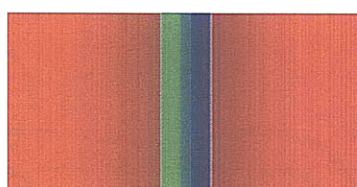
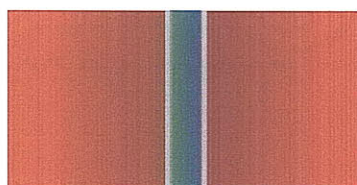
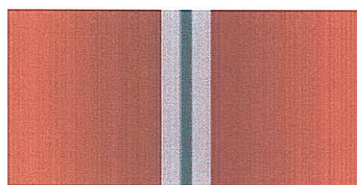
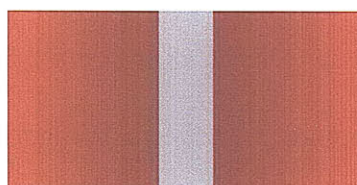
(a)  $t=0$ (b)  $t=30$ (c)  $t=100$ (d)  $t=120$ (e)  $t=150$ 

Figure 6-6: An example of TLPB in a ternary system. A liquid interlayer forms after a solid state reaction that produced the blue-green phase. Once the liquid layer has formed, isothermal solidification proceeds as in figure 6-2.

## 6.5 Future work

A discussion on future work related to modeling transient liquid phase bonding can be found in section 7.1.2.

## References

- [1] WD MacDonald and TW Eagar. Transient liquid-phase bonding. *ANNUAL REVIEW OF MATERIALS SCIENCE*, 22:23–46, 1992.
- [2] W. F. Gale and D. A. Butts. Transient liquid phase bonding. *Science and Technology of Welding and Joining*, 9(4):283–300, 2004.
- [3] M. A. Jabbareh and H. Assadi. Modelling of microstructure evolution in transient-liquid-phase diffusion bonding under temperature gradient. *Scripta Materialia*, 60(9):780–782, 2009.
- [4] Y. Zhou, W. F. Gale, and T. H. North. Modelling of transient liquid phase bonding. *International Materials Reviews*, 40(5):181–196, 1995.
- [5] Y. Zhou. Analytical modeling of isothermal solidification during transient liquid phase (tlp) bonding. *Journal of Materials Science Letters*, 20(9):841–844, 2001.
- [6] I. Tuahpoku, M. Dollar, and T. B. Massalski. A study of the transient liquid-phase bonding process applied to a ag-cu-ag sandwich joint. *Metallurgical Transactions a-Physical Metallurgy and Materials Science*, 19(3):675–686, 1988.
- [7] T. C. Illingworth, I. O. Golosnoy, V. Gergely, and T. W. Clyne. Numerical modelling of transient liquid phase bonding and other diffusion controlled phase changes. *Journal of Materials Science*, 40(9-10):2505–2511, 2005. 4th International Conference on High Temperature Capillarity MAR 31-APR 03, 2004 Sanremo, ITALY.

- [8] T. C. Illingworth, I. O. Golosnoy, and T. W. Clyne. Modelling of transient liquid phase bonding in binary systems- a new parametric study. *Materials Science and Engineering a-Structural Materials Properties Microstructure and Processing*, 445:493–500, 2007.
- [9] C. W. Sinclair. Modeling transient liquid phase bonding in multicomponent systems. *Journal of Phase Equilibria*, 20(4):361–369, 1999.
- [10] C. W. Sinclair, G. R. Purdy, and J. E. Morral. Transient liquid-phase bonding in two-phase ternary systems. *Metallurgical and Materials Transactions a-Physical Metallurgy and Materials Science*, 31(4):1187–1192, 2000.
- [11] C. E. Campbell and W. J. Boettinger. Transient liquid-phase bonding in the ni-al-b system. *Metallurgical and Materials Transactions a-Physical Metallurgy and Materials Science*, 31(11):2835–2847, 2000. 37 MINERALS METALS MATERIALS SOC WARRENDALE 375HJ.
- [12] J. Eiken, B. Boettger, and I. Steinbach. Multiphase-field approach for multicomponent alloys with extrapolation scheme for numerical application. *PHYSICAL REVIEW E*, 73(6, Part 2), JUN 2006.
- [13] M. C. Flemings. Solidification processing. *Metallurgical Transactions*, 5(10):2121–2134, 1974.
- [14] W. J. Boettinger and J. A. Warren. Simulation of the cell to plane front transition during directional solidification at high velocity. *Journal of Crystal Growth*, 200(3-4):583–591, 1999.
- [15] D.A. Porter and K.E. Easterling. *Phase Transformations in Metals and Alloys*. Stanley Thornes (Publishers) Ltd, 2000.
- [16] W. W. Mullins and R. F. Sekerka. Morphological stability of a particle growing by diffusion or heat flow. *Journal of Applied Physics*, 34(2):323–&, 1963.

- [17] W. W. Mullins and R. F. Sekerka. Stability of planar interface during solidification of dilute binary alloy. *Journal of Applied Physics*, 35(2):444–45, 1964.
- [18] A. A. Shirzadi and E. R. Wallach. Temperature gradient transient liquid phase diffusion bonding: a new method for joining advanced materials. *Science and Technology of Welding and Joining*, 2(3):89–94, 1997.
- [19] H. Assadi, A. A. Shirzadi, and E. R. Wallach. Transient liquid phase diffusion bonding under a temperature gradient: Modelling of the interface morphology. *Acta Materialia*, 49(1):31–39, 2001.
- [20] X. G. Wang, X. G. Li, and Q. Yan. Effect of two step heating process on joint microstructure and properties during transient liquid phase bonding. *Science and Technology of Welding and Joining*, 12:455–459, 2007.
- [21] X. G. Wang, X. G. Li, and Q. Yan. A novel bonding process: Super-cooled transient liquid phase bonding. *Acta Metallurgica Sinica*, 43:1096–1100, 2007.

THIS PAGE INTENTIONALLY LEFT BLANK



# Chapter 7

## Conclusion

This thesis has shown that successful computational modeling involves a balance between theoretical model development, numerical methods, and reference to experiment. The original goal of this work was to improve materials processing by simulating transient liquid phases in multiphase microstructure, and achieving this goal required deriving a new multiphase, multicomponent model and appropriate numerical methods. The model leads to a new interpretation of premelting and liquid film formation at phase boundaries, and produced the first complete simulation of transient liquid bonding. As a whole, the work emphasizes the importance of metastable phases in modeling microstructure evolution. Previously proposed models that use phase diagrams and diffusion equations rather than the free energy curves, it is argued, are too simplistic to correctly model multiphase systems. The important contributions of this work are now summarized.

### Model development

Perhaps the most important contribution of this thesis is the derivation in chapter 2 of diffuse interface model for simulating microstructure with an arbitrary number of phases and components. The model was derived from basic thermodynamic and kinetic principles with all steps and assumptions described in detail. This allowed

for the correction of subtle misconceptions which appear in other multiphase and multicomponent models. A composition gradient energy is included in the model, and driving forces and evolution equations that properly account for conservation conditions are derived. The physical interpretation of the model parameters was also discussed. Compared to other proposed multiphase models which were summarized in chapter 1, the model developed in this work is simpler in form and less computationally expensive, yet capable of simulating a wider range of phenomena. The model is particularly well-suited for studying nucleation and growth, spinodal decomposition, and the effect of metastable phases on microstructure, all of which were studied in later chapters.

### **A time-adaptive numerical method**

A correctly derived model is an important, but any computer simulation is governed by the accuracy and robustness of the numerical methods employed. In this regard, the multiphase equations, which are nonlinear and stiff, present a numerical challenge. Explicit finite difference and semi-implicit spectral methods are commonly used to solve phase-field equations and were analyzed in chapter 3. The methods were applied to a single-component nonlinear phase-field diffusion equation that describes spinodal decomposition. Explicit finite difference was found to be very unstable and suffer from discretization difficulties while the semi-implicit spectral method was found to be orders of magnitude more stable but potentially very inaccurate. The sources of inaccuracy have been overlooked in studies that favor the stability improvements. This thesis investigated the source of the error and found that the rich temporal dynamics that occur during spinodal decomposition as well as using a large timestep with a first-order accurate time integrator were responsible for much of the error. The accuracy of the spectral method was improved with a second-order semi-implicit Runge-Kutta time integrator and an adaptive timestepping procedure. For a constant amount of total accumulated error, this adaptive Runge-Kutta method was found to

be orders of magnitude faster than explicit finite difference and first-order spectral.

## **Data analysis techniques**

A composition map was introduced in section 4.6 as an insightful way to visualize composition in complex microstructures, particularly at interfaces. The composition map was used throughout the thesis to supplement images of microstructure. In several instances, the composition map illuminates microstructural evolution dynamics that is not detectable in pictures of the microstructure. Computer code that performs quantitative image analysis of microstructures was also written. This code counts the number and size of particles in images and is useful for studying coarsening behavior.

## **Discovery of diffusion limited growth instability**

An interesting diffusion limited growth instability in multiphase systems confined to a thin film was discovered with the new multiphase model and is discussed in chapter 4. The instability does not appear to have been previously reported, although its existence has been suggested by several authors. The instability leads to spherulites with complex patterns that appear to share similarities with snowflakes as well as structures in solidifying metallic alloys and polymer mixtures. The instability highlights how ternary multiphase systems, which have received little study, are significantly different from binary systems.

## **Simulation of metastable phases and transient liquids**

Chapters 5 and 6 present a variety of simulations that demonstrate how the multiphase model correctly captures intricate asymmetries in the processes of solidification and melting. A nucleation barrier for solidification was observed and prompted development of a Monte-Carlo-like procedure to trigger nucleation. However when solid was heated from below the melting point, premelting was observed first at phase triple

junctions and then at phase boundaries. The formation of liquid below the melting point was attributed to the shape and position of the metastable liquid curve, which was found to have large effect on microstructure by creating low-energy paths through composition space. Slow diffusivity in solids relative to liquids lead to solutal melting below the melting point and was another example of asymmetry between solidification and melting. Finally, the multiphase method was used to produce the first reported simulation of the entire transient liquid phase bonding process. The model was also shown to be a promising candidate for optimizing the bonding process and for simulating non-planar solidification interfaces which were recently discovered to increase bond strength.

## 7.1 Future work

This primary focus of this thesis was on model development, analysis of numerical methods, and a phenomenological description of materials behavior such as nucleation and growth, premelting, and the appearance of transient liquid phases. These were necessary steps toward the larger goal of quantitative and predictive modeling of microstructure. Having developed a suitable multiphase model, the next steps of this research will involve incorporating thermodynamic and kinetic data to simulate experimental systems. Attempting a quantitative simulation of transient liquid phase bonding would be a good first step because it would help answer difficult materials processing questions while at the same time providing a valuable validation of the multiphase model. Modeling other physical systems may necessitate extension of the model to include nonisothermal conditions, interfacial anisotropy, elasticity, or crystallography, and further development of sophisticated numerical methods will likely prove necessary as well. Three specific areas for future work are discussed below, and a detailed proposal for the application of wavelet transforms to solve the phase-field equations can be found in appendix A.

### 7.1.1 Numerical methods

Although the adaptive Runge-Kutta method studied in chapter 3 offers significant improvements over explicit finite difference and first-order spectral methods, there is still room for improvement. It greatly increases accuracy, but the method can be quite computationally expensive, especially if stochastic noise is added as the simulation progresses. The method proposed here represents a quick and easy fix for a commonly used method, and more importantly demonstrates that simple numerical methods are not sufficient for phase-field modeling. Ultimately, a multiresolution technique is needed that allows for both spatial and temporal adaptivity. The wavelet transform appears to be a very promising candidate, and its application to phase-field modeling is discussed in appendix A. The biggest computational drawback (besides lack of an adaptive grid) with the adaptive timestepping method proposed here is that the timestep for the entire system is limited by the smallest timestep required anywhere in the system. Chapter 6 presents simulations of transient liquid bonding where diffusivity is orders of magnitude faster in the liquid than in the solid. Timestep adaptivity where the liquid is evolved with small timesteps and the solid with large timesteps would result in a big computational savings. Thus space and time adaptivity of wavelets could be advantageous.

Even without the development of multiresolution methods, the adaptive IMEX-RK2 method could likely still be improved. A more sophisticated PID timestep controller would likely make better timestep choices [1, 2]. It could be interesting to investigate variable step size BDF multistep IMEX methods that were recently developed [3]. SBDF schemes have better error damping properties for very stiff equations and heavily dominant diffusion problems, and are less computationally expensive because they make use of data that has already been calculated. However because the step sizes in the past cannot be changed, they may be limited in their ability to make rapid changes to the step size.

Very recently, a stiffly accurate third-order IMEX-RK scheme has been developed

[4]. The third order Runge-Kutta iterator is more computationally expensive than the second-order iterator, but also more accurate. There is a chance that the third-order method with an embedded second-order method might outperform the second-order/first-order method proposed here by allowing larger timesteps to be tolerated. It is also possible that the additional cost of the third-order method more than offsets the timestep savings.

### 7.1.2 Transient liquid bonding

Perhaps the most promising application of the multiphase model is simulating and optimizing transient liquid liquid bonding, which can be very time consuming and therefore difficult to optimize times and temperatures experimentally. This thesis showed the promise of the multiphase model in that it was able to capture subtle aspects of the bonding process as well as the formation of non-planar geometries. It should also be able to simulate the other important phenomena that influence the quality of transient liquid phase bonds. Oxide layers or precipitates of other phases can form and disrupt the solidification process, or form when a bond is cooled without sufficient homogenization. The formation of these phases is specific to the thermodynamics of each material system and cannot correctly be captured with the current models that use diffusion equations and phase diagrams. Another complicating factor is that the substrate material in a transient liquid bond is usually composed of grains, and the transient liquid can penetrate the grain boundaries. This and the fact that the grains grow preferentially into the solidifying liquid can produce a non-planar interface. All of these phenomena could potentially be simulated with the multiphase model developed in this work.

### 7.1.3 Thermodynamic and kinetic data

While the multiphase, multicomponent model represents an improvement in the way we think about materials processes, it does not improve our current knowledge of

materials properties. Ultimately, any attempt to accurately model highly nonlinear, materials specific microstructural processes will be limited by the availability of thermodynamic and kinetic data. Unfortunately the systems that are most desirable to model are often the ones for which little thermodynamic data exists or is very difficult to obtain experimentally. Prediction of these quantities is part of the motivation for development of models in the first place. For instance, the phase-field model developed in this work relies on knowledge of metastable extensions of free energy functions which are difficult to measure but essential to the method. Furthermore, diffusivity in ternary or higher systems is known to be a function of composition but remains a formidable experimental task to measure. Progress determining and cataloging free energy functions and diffusivities in multicomponent systems is being made [5, 6], but remains a challenging problem. The solution will likely involve clever combinations of thermodynamic models for the parameters themselves, calculations from ab-initio and atomistic simulations, and experiment, when possible.

## References

- [1] G. Soderlind. Automatic control and adaptive time-stepping. *Numerical Algorithms*, 31(1-4):281–310, 2002. 2001 ANODE Workshop JAN 03-06, 2001 AUCKLAND, NEW ZEALAND.
- [2] C. A. Kennedy and M. H. Carpenter. Additive runge-kutta schemes for convection-diffusion-reaction equations. *Applied Numerical Mathematics*, 44(1-2):139–181, 2003.
- [3] D. Wang and S. J. Ruuth. Variable step-size implicit-explicit linear multistep methods for time-dependent partial differential equations. *Journal of Computational Mathematics*, 26(6):838–855, 2008. Wang, Dong Ruuth, Steven J.

- [4] S. Boscarino. On an accurate third order implicit-explicit runge-kutta method for stiff problems. *Applied Numerical Mathematics*, 59(7):1515–1528, 2009. Boscarino, Sebastiano.
- [5] T. Kitashima. Coupling of the phase-field and calphad methods for predicting multicomponent, solid-state phase transformations. *Philosophical Magazine*, 88(11):1615–1637, 2008. Kitashima, Tomonori 85 TAYLOR & FRANCIS LTD 331IP.
- [6] U. R. Kattner and C. E. Campbell. Modelling of thermodynamics and diffusion in multicomponent systems. *Materials Science and Technology*, 25(4):443–459, 2009. Kattner, U. R. Campbell, C. E. 183 MANEY PUBLISHING LEEDS 438XR.



# Appendix A

## Multiresolution phase-field modeling with the discrete wavelet transform

The discussion in this appendix is taken from a proposal written by the author in July 2009 for an NRC postdoctoral fellowship at NIST.

### A.1 Introduction

Phase-field modeling has provided insight into many difficult materials science problems over the last twenty years, contributing to our understanding solidification [1], solid-state phase transformations, coarsening and grain growth, crystallography, elasticity, dislocation dynamics, and electrochemistry [2, 3]. Despite its success, important problems ideally suited for phase-field have often proven too difficult computationally. Connecting physics on the nanometer scale to experimentally measurable phenomena on diffusive time scales and microstructural length scales remains a major challenge for computational science. As a result, phase-field has remained largely a phenomenological approach; direct comparison of phase-field simulations with exper-

imental observations has not been possible despite advances in numerical methods, development of sophisticated software libraries, and increases in computing power of orders of magnitude.

Removing the computational limitations of phase-field modeling would transform it into a predictive approach that would have an impact on many areas of science. Predictive modeling techniques are needed to help solve real-world engineering problems like understanding how nanograins in photovoltaic materials affect electro-optical properties, modeling stress in thin films to better understand Sn whisker formation, and studying microstructure formation in energy storage materials to improve batteries and hydrogen fuel cells.

The downside of phase-field is that it is very computationally intensive because the now wide interfaces must be resolved. The different length scales that naturally occur in microstructure present a numerical challenge that was highlighted in recent survey papers as an outstanding problem in phase-field modeling [4, 5]. The problem is that in experimental systems, the width of an interface might be at most 10nm while the grains it separates could be on the order of micrometers in diameter, or larger. Important physics occurs on the scale of the interface, but many properties of microstructure are determined at the length scale of grains. Since microscopic behavior often involves tens or hundreds of grains, performing realistic simulations that capture both length scales has been impossible. An interface must be resolved with 5-10 grid points for numerical stability, making the size of a regular square grid needed to model a collection of grains enormous. Unfortunately this numerical difficulty is often avoided in phase-field modeling with the use of unrealistically thick interfaces that introduce spurious effects. When interfaces are too wide, the coalescence of neighboring particles is exaggerated, as are nonequilibrium effects like solute trapping and solute drag. As a result, a direct comparison of phase-field simulations with experimental observations has been challenging, and phase-field modeling has remained largely a phenomenological method.

## A.2 Background

Many different numerical methods have been used to solve the phase-field equations, and each method has advantages and disadvantages. Explicit finite difference is commonly used because it is the simplest to program, but the 4th order spatial derivative that often appears in phase-field equations introduces a severe timestep restriction for explicit timestepping and makes simulation of long times impossible. Fourier spectral solvers with implicit-explicit operator splitting have proven to be one of the most efficient methods to date, but use of the discrete Fourier transform (DFT) requires a regular square grid. Adaptive grid techniques are appealing because interesting behavior occurs mostly at interfaces which comprise a very small volume fraction of a microstructure. There is not as much activity in the interior of grains, and much less resolution is required there. Adaptive grid techniques have been successful, but the advantages of DFT must be forfeited. Additionally, much computational effort is wasted tracking interfaces, especially for microstructures comprised of a large number of grains or precipitates. Explicitly tracking interfaces with adaptive meshing is somewhat counterproductive, since one of the main advantages of phase-field is to eliminate the necessity of tracking interfaces. Implicit finite volume solvers have proven effective with non-uniform grids and allow for the use of large timesteps, but fully implicit solvers are computationally expensive and generally do not scale well.

The discrete wavelet transform (DWT) is currently used in many fields of engineering to solve PDEs [6] and may be the key to addressing the numerical difficulty in phase-field. The discrete wavelet transform is similar to the Fourier transform in that it is a way to represent a complex function by simpler functions that are well understood. A wavelet  $w(x)$  is a square integrable function with zero mean, and a wavelet basis  $w_{jk}$  is created by scaling and translating the wavelet:

$$w_{jk}(x) = 2^{j/2}w(2^j x - k) \tag{A.1}$$

$k$  is the translation index and  $j$  is the scale index. The wavelet series for a function  $f(x)$  is:

$$f(x) = \sum_{k=-\infty}^{\infty} a_k \phi(x - k) + \sum_{k=-\infty}^{\infty} \sum_{j=0}^{\infty} b_{jk} w_{jk}(x) \quad (\text{A.2})$$

$a_k$  and  $b_{jk}$  are the wavelet coefficients and  $\phi(x - k)$  is a scaling function that captures the average value of the function. The wavelets  $w_{jk}$  capture the multiresolution detail. Having two indices allows the wavelet transform to provide both frequency and spatial localization. The basis functions in the Fourier transform, on the other hand, are frequencies that have only a scale component. Wavelets used in numerical simulation must be compactly supported, meaning that they are non-zero only on a finite interval and zero outside that interval. Compactly supported wavelets can be used as trial and test functions to solve PDEs using the Galerkin method.

DWT has three major advantages over DFT and adaptive mesh techniques when applied to phase-field problems. First, unlike the discrete Fourier transform, the DWT is localized in space as well as frequency, providing information about which frequencies are present and also where they occur. The wavelet transform is a multiresolution method because the wavelet basis captures high frequencies with high resolution, and low frequencies with low resolution. Spatial localization can be used in phase-field to extract the interfacial regions of a microstructure and focus the computational effort at the interface, much like an adaptive grid but without the headache of tracking interfaces. Extraction of the grain boundaries could be achieved by appropriately filtering the DWT coefficients. This is not possible with the Fourier transform because the DFT is only localized in frequency; a local change in a signal is reflected in all of the Fourier coefficients. Information about where each frequency occurs is encoded in the phase of the Fourier transform rather than the amplitude, and this phase information cannot easily be interpreted [7]. Second, the DWT is designed to capture high frequencies, while the DFT is plagued by the Gibbs phenomenon and slow decay of coefficients for functions that aren't smooth. Wavelet transforms do not exhibit the

Gibbs phenomena, and when properly designed can be used to capture discontinuities and sharp features efficiently [8]. Capturing high frequencies accurately and with few coefficients is an attractive feature when modeling thin interfaces which have large concentration gradients. Finally, the DWT is cheap to compute, scaling as  $O(N)$  [9]. This scaling is ideal and an improvement over DFT which scales as  $O(N\log N)$ , and DWT may allow for simulation of systems larger than ever before possible. When the size of a system becomes large, the difference between  $O(N)$  and  $O(N\log N)$  becomes significant.  $N$  for a large simulation could easily be  $10^{10}$ , and  $\log(10^{10}) \approx 10$ , meaning DWT could be an order of magnitude faster than DFT. Additionally, DWT may also be easier to parallelize than DFT because of the spatial localization offered by DWT. The computation of each coefficient in a discrete Fourier transform requires knowledge of the entire grid, making parallelization difficult.

The wavelet transform has not yet received much attention from the phase-field community, and an extensive literature search revealed only one attempt to use wavelet transforms to solve phase-field problems [10]. In this paper, Wang and Pan focused on numerical methods rather than searching for new physical insights, and the work was limited in that it focused on solving the Allen-Cahn equation, perhaps the simplest example of a phase-field model. The work also only took advantage of the data compression aspect of the DWT and used explicit timestepping on a uniform grid. Still, the authors demonstrated the promise of wavelet transforms as an effective replacement for adaptive meshes. Their wavelet solver was 33 times faster than an explicit finite difference solver for an equivalent simulation. This is a significant finding, because using DFT with explicit timestepping is significantly *slower* than explicit finite difference. Not only is DFT less stable, but for a fixed timestep the computational overhead of one iteration of DFT is much larger than for one iteration of finite difference. The real improvements with DFT appear after the use of semi-implicit operator splitting, which provides stability for timesteps two to three orders of magnitude larger. Incorporating semi-implicit techniques with the DWT will likely lead

to similar huge performance gains. Wang and Pan acknowledge that there is room for improvement with the use of different timesteps for wavelet coefficients at different levels. Small, quickly evolving frequencies require small timesteps while large, slowly evolving frequencies can be evolved with much larger timesteps. Development of a multiscale timestepping technique within the framework of an implicit-explicit operator splitting will be necessary to fully realize the advantages of DWT.

The Allen-Cahn equation studied by Wang and Pan applies to non-conserved fields:

$$\frac{\partial \phi}{\partial t} = -M \left( \frac{\partial f(\phi)}{\partial \phi} - k \nabla^2 \phi \right) \quad (\text{A.3})$$

$\phi$  is the order parameter,  $M$  is a mobility,  $f(\phi)$  is a homogeneous free energy, and  $k$  is a gradient energy coefficient. Generally  $f(\phi)$  is constructed so that a system will want to separate into regions of  $\phi = 1$  and  $\phi = 0$ . This phase separation is opposed by the gradient energy term which penalizes sharp interfaces, and a stable diffuse interface represents equilibrium between these two opposing forces.

It will be important to extend DWT techniques to the Cahn-Hilliard equation, which applies to conserved fields:

$$\frac{\partial \phi}{\partial t} = \nabla \cdot \left( M \nabla \left( \frac{\partial f(\phi)}{\partial \phi} - k \nabla^2 \phi \right) \right) \quad (\text{A.4})$$

The fourth derivative in this equation causes severe instability for explicit solvers, and the payoff from using a wavelet transform technique will likely be much greater than for the Allen-Cahn equation.

### A.3 Expected results and their significance

The value of this project is that it has the potential to transform phase-field from a phenomenological modeling approach into a predictive approach that captures both experimental time and length scales. Computational methods have had difficulty

connecting physics on the nanometer scale to experimentally measurable phenomena on diffusive time scales and microstructural length scales. Making this connection would be a big leap forward for computational modeling. Furthermore, because phase-field has been used to study a wide variety of phenomena, improving the fundamentals of the modeling technique will have an impact on many areas of science. Several areas where the wavelet transform is expected to make important contributions are now described.

Phase-field simulations of solidification have always been performed at large undercooling, often more than an order of magnitude larger than in experiments, because of numerical limitations [4]. It is crucial to extend simulations to the low undercooling regime because it is known that interfacial kinetics change. High undercooling is a kinetically limited regime, but low undercooling represents a diffusion limited regime. The problem, once again, arises from differing length scales that must be resolved during solidification. Low undercooling produces slow growth rates, and the diffusion field ahead of a solidifying structure can be several orders of magnitude larger than the structure itself. Multiresolution DWT methods seem ideally suited to solve this problem.

Nucleation and growth is another phenomena that suffers from length scale difficulties that could be alleviated by the DWT. Nucleation has proven to be a truly difficult problem and remains the least well understood stage of solidification, even though phase-field is extremely well suited for simulating it [11]. Because nucleation events occur on the length scale of an interface, simulations require extremely small spatial and time resolution over the whole domain to catch them. Growth and coarsening of the nuclei then occurs on much larger length and time scales, and it has been impossible computationally to capture the nucleation events followed by a considerable growth of the microstructure. Being able to simulate the entire nucleation and growth process is important because microstructure plays a big role in determining the macroscopic properties of materials.

The newly developed phase-field crystal (PFC) method has recently received attention as an approach that merges phase-field and molecular dynamics. PFC provides a way to simulate microstructure on diffusive time scales, which are not accessible by molecular dynamics, and atomistic length scales. In PFC an atomic probability density serves as the phase-field variable for which an energy functional is minimized. It is somewhat analogous to density functional theory which is used to simulate electrons based on their density distribution. Crystal anisotropy, dislocations, and plastic deformation are incorporated automatically in PFC, unlike in standard phase-field models [12, 13]. One of the difficulties with phase-field crystal is that it faces the same system size limitations as molecular dynamics, and the key to improving PFC lies in bridging length scales from atomistic to macro-scale [14]. The PFC equations are sixth order nonlinear partial differential equations that present a numerical challenge. Adaptive meshing and DFT methods have been successfully employed but have not resolved the numerical difficulties. Wavelet transforms could provide an advantage over DFT when dealing with the longer wavelengths that control microstructure evolution. DFT has already proven to be particularly efficient when applied to PFC, [15] and it may be possible to combine DFT and DWT into a hybrid method where DFT is used to represent the underlying crystal lattice which is periodic at the atomic scale, and DWT is used to efficiently handle longer wavelength interactions.

Finally, the DWT approach may also provide advantages to phase-field models of electrochemistry. A recently developed and relatively simple electrochemical phase-field model correctly captured the behavior of an electrochemical interface, including the formation of a charge double-layer [3]. The model has been used to produce phenomenologically realistic simulations of electrodeposition and electrodisolution, but unfortunately encountered severe numerical challenges [2]. Solving the evolution equations proved difficult because the resolution of charge within the interfacial region required many more mesh points than typical of phase-field models because of the intricate charge distribution in the interface. Only 1D systems were studied, as the



need to resolve the charge distribution in close proximity to the interface restricted the size of the domain and lengths of time that could be modeled. The ability of wavelet transforms to capture sharp frequencies and focus computational effort at interfaces could be particularly helpful to deal with this problem.

## References

- [1] WJ Boettinger, JA Warren, C Beckermann, and A Karma. Phase-field simulation of solidification. *ANNUAL REVIEW OF MATERIALS RESEARCH*, 32:163–194, 2002.
- [2] J. E. Guyer, W. J. Boettinger, J. A. Warren, and G. B. McFadden. Phase field modeling of electrochemistry. ii. kinetics. *Physical Review E*, 69(2), 2004. Part 1.
- [3] J. E. Guyer, W. J. Boettinger, J. A. Warren, and G. B. McFadden. Phase field modeling of electrochemistry. i. equilibrium. *Physical Review E*, 69(2), 2004. Part 1.
- [4] I. Singer-Loginova and H. M. Singer. The phase field technique for modeling multiphase materials. *Reports on Progress in Physics*, 71(10):32, 2008. Singer-Loginova, I. Singer, H. M. Swiss Federal Institute of Technology ETH, Zurich, Switzerland 374 IOP PUBLISHING LTD 362GS.
- [5] N. Moelans, B. Blanpain, and P. Wollants. An introduction to phase-field modeling of microstructure evolution. *Calphad-Computer Coupling of Phase Diagrams and Thermochemistry*, 32(2):268–294, 2008. Moelans, Nele Blanpain, Bart Wollants, Patrick.
- [6] Karsten Urban. *Wavelets in Numerical Simulation: Problem Adapted Construction and Applications*. Springer, 2002.

- [7] Martin J. Mohlenkamp and Maria Cristina Pereyra. *Wavelets, Their Friends, and What They Can Do for You*. European Mathematical Society, 2008.
- [8] Gilbert Strang. *Computational Science and Engineering*. Wellesley-Cambridge Press, 2007.
- [9] G. Beylkin, R. Coifman, and V. Rokhlin. Fast wavelet transforms and numerical algorithms .1. *Communications on Pure and Applied Mathematics*, 44(2):141–183, 1991.
- [10] D. Wang and J. Pan. A wavelet-galerkin scheme for the phase field model of microstructural evolution of materials. *Computational Materials Science*, 29(2):221–242, 2004.
- [11] U. Hecht, L. Granasy, T. Pusztai, B. Bottger, M. Apel, V. Witusiewicz, L. Ratke, J. De Wilde, L. Froyen, D. Camel, B. Drevet, G. Faivre, S. G. Fries, B. Legendre, and S. Rex. Multiphase solidification in multicomponent alloys. *Materials Science & Engineering R-Reports*, 46(1-2):1–49, 2004.
- [12] K. R. Elder, M. Katakowski, M. Haataja, and M. Grant. Modeling elasticity in crystal growth. *Physical Review Letters*, 88(24), 2002.
- [13] K. R. Elder and M. Grant. Modeling elastic and plastic deformations in nonequilibrium processing using phase field crystals. *Physical Review E*, 70(5), 2004. Part 1.
- [14] N. Provatas, J. A. Dantzig, B. Athreya, P. Chan, P. Stefanovic, N. Goldenfeld, and K. R. Elder. Using the phase-field crystal method in the multi-scale modeling of microstructure evolution. *Jom*, 59(7):83–90, 2007. Provatas, N. Dantzig, J. A. Athreya, B. Chan, P. Stefanovic, P. Goldenfeld, N. Elder, K. R. 78 MINERALS METALS MATERIALS SOC 188CD.

- [15] M. Cheng and J. A. Warren. An efficient algorithm for solving the phase field crystal model. *Journal of Computational Physics*, 227(12):6241–6248, 2008.
- Cheng, Mowei Warren, James A. 27 ACADEMIC PRESS INC ELSEVIER SCIENCE 310AU.